Ultracold Bosons in Optical Lattices for Quantum Measurement and Simulation

by

William Cody Burton

Bachelor of Arts in Physics, Princeton University (2012)

Submitted to the Department of Physics
in partial fulfillment of the requirements for the degree of

Doctor of Philosophy

at the

MASSACHUSETTS INSTITUTE OF TECHNOLOGY

February 2019

Author .....
Department of Physics
September 12, 2018

Certified by .....
Wolfgang Ketterle
John D. MacArthur Professor of Physics
Thesis Supervisor

Accepted by .....
Nergis Mavalvala
Associate Department Head, Physics

Ultracold Bosons in Optical Lattices for Quantum Measurement and Simulation

by

William Cody Burton

Submitted to the Department of Physics
on September 12, 2018, in partial fulfillment of the
requirements for the degree of
Doctor of Philosophy

Abstract

Ultracold atoms provide a platform that allows for pristine control of a physical system, and have found uses in both the fields of quantum measurement and quantum simulation. Optical lattices, created by the AC Stark shift of a coherent laser beam, are a versatile tool to control ultracold atoms and implement novel Hamiltonians. In this thesis, I report on three experiments using the bosonic species Rubidium-87 trapped in optical lattices.

I first discuss our work in simulating the Harper-Hofstadter Hamiltonian, which describes charged particles in high magnetic fields, and has connections to topological physics. To simulate the charged particles, we use laser-assisted tunneling to add a complex phase to tunneling in the optical lattice. For the first time, we have condensed bosons into the ground state of the Harper-Hofstadter Hamiltonian. In addition, we have demonstrated that we can add strong on-site interactions to the effective Hamiltonian, opening the door to studies of interesting states near the Mott insulator transition.

Next, I present a novel technique to preserve phase coherence between separated quantum systems, called superfluid shielding. Phase coherence is important for both quantum measurement and simulation, and is fundamentally limited by projection noise. When an interacting quantum system is split, frozen-in number fluctuations lead to fluctuations of the relative phase between separated subsystems. We cancel the effect of these fluctuations by immersing the separated subsystems in a common superfluid bath, and demonstrate that we can increase coherence lifetime beyond the projection noise limit.

Finally, I discuss our efforts in simulating magnetic ordering in the spin-1 Heisenberg Hamiltonian. It is hard to adiabatically ramp into magnetically ordered ground states, because they often have gapless excitations. Instead, we use a spin-dependent lattice to modify interspin interactions, allowing us to ramp into the spin Mott insulator, which has a gap and can therefore act as a cold starting point for exploration of the rest of the phase diagram. We have achieved a cold spin temperature in the spin Mott insulator, and I discuss plans to also achieve a cold charge temperature

and then ramp to the the xy-ferromagnet, which has spin-charge separation.

Thesis Supervisor: Wolfgang Ketterle
Title: John D. MacArthur Professor of Physics

Acknowledgments

In this thesis, I use the first-person singular "I" when discussing the work, but no thesis is created by a single person. Through my time at MIT, I have been supported and helped by more people than I can list here.

I first wish to acknowledge my advisor Wolfgang Ketterle. He has undoubtedly had the greatest influence on how I think about and approach physics. It always amazes me when Wolfgang can take something that I thought was irreducibly quantum and give a classical analogy that neatly explains it. Of course, I would not be where I am today without a host of teachers and mentors who nurtured and supported my love of physics, including Robert Donaldson, Ralph Bunday, James Schafer, Jim Restorff, Marilyn Wun-Fogle, Bobby Berg, David Huse, Mike Romalis, Trey Porto, and Andrew Houck.

When I first began working in BEC4, Hiro Miyake and Georgios Siviloglou were the senior graduate student and postdoc, respectively. Both were kind and patient in helping me learn not only atomic physics, but the special quirks of our particular experimental apparatus. I think that Georgios's most important advice was always to remember "do not panic." Colin Kennedy and Woo Chang Chung were my fellow grad students and companions for most of my time here. Colin's energy and Woo Chang's focus made for a stimulating and efficient research environment. The second postdoc that I worked with, Wenlan Chen, was a great addition to the lab. She had a broad knowledge base and a view for a good picture. I especially want to thank her for keeping us from going down rabbit holes of research and keeping our eyes on the prize! Finally, I must acknowledge the assistance of our undergraduate and visiting students: Yuri Lenskiy, Benedikt Groever, and Samarth Vadia.

Of course, BEC4 is not an island, and the other labs, both in Wolfgang's group and in the CUA, have been immensely helpful. The ability to just walk down the hallway if you have technical questions, need supplies, or even just want to chat about physics is truly unique and has led to many friendships over the years. I want to especially point out the close connection between BEC4 and BEC5, who both want

to use bosons in optical lattices to study magnetic ordering. This has led to many conversations and deep friendships with Niki Jepsen, Ivana Dimitrova, Jesse Amato-Grill, and Will Lunden. The postdocs in Wolfgang's other labs, Alan Jamison and Chris Lee, provided mentorship, a sounding-board, and friendship to all the labs.

Outside of work, the people I probably spent the most time with were my roommates Tom Cooper and Matt Nichols, and the quasi-roommate Ian Counts. I'm glad I got to live with good friends and colleagues for five years, and I'll miss coming home to a house full of physicists. I would like to thank all of my friends from the Physics Department for helping to keep me sane, whether through pub socials, hiking, board games, or just hanging out! A special thanks goes out to Zak Vendeiro, Alban Urvoy, Boris Braverman, Lawrence Cheuk, Sergio Cantu, John Hardin, Gabriel Collin, Mukund Madhav, Nancy Aggarwal, Jenny Schloss, Tom Mahony, Alex Leder, Alex Ji, and Keaton Burns!

Working as a volunteer Emergency Medical Technician with MIT Emergency Medical Services provided a welcome complement to my work in grad school. While physics research can take months or years and alternates between tedious and sublime, working on an ambulance provides a much faster feedback loop — within an hour of getting a call, you've done your best to make someone's life better. I appreciate all members of MIT EMS for giving me a second home on campus, and especially want to thank my qCC partner Andrew Tang, the Training Officer before me Shivangi Goel, and my successors Vivian Hu and Ann Liu.

Finally, none of this would be possible without the support and love of my family and my girlfriend, Olivia. My parents, Bill and Suzanne Burton, supported by my grandparents, Bill and Jean Eckert and John and Judy Burton, raised me to be intellectually curious. My siblings, Tuck, M-E, and Mindy, have always been my best friends, and I am proud of what they have accomplished so far and excited to see what their future holds! I'm so glad that I met Olivia three years ago, when she was interning at a tech company in Kendall Square, and since then she's proven to be one of the most intelligent and determined people that I know. It's been a joy getting to know her family, and I can't wait till you join me in Colorado!

Contents

List of Figures

List of Tables

Chapter 1

Introduction

Ultracold atoms provide a clean and precisely controllable system for studying a wide range of physical effects. Through the use of lasers, magnetic fields, and microwave and radio frequency (RF) waves, one can implement nearly any microscopic Hamiltonian to a high accuracy. With the advent of laser cooling and evaporative cooling, it became possible to create Bose-Einstein condensates (BECs) [1, 2], which were first predicted by Bose and Einstein in 1924. In a BEC, the low temperatures lead to a macroscopic occupation of a single quantum state. Initial work with BECs involved exploring exotic physics, including matter wave interference [3], superfluidity [4], vortex lattices [5], and superradiance [6]. Later work achieved similarly low temperatures in fermions, leading to the production of degenerate Fermi gases [7].

Once it had been shown that optical dipole forces could be used to create lattice potentials [8, 9], a new realm of quantum simulation was opened. Fermions in an optical lattice are described by the Fermi-Hubbard model, which is also the simplest model of electrons in a crystal lattice, and is believed to be connected to the phenomenon of high-temperature superconductivity [10, 11]. Bosonic atoms, on the other hand, are most naturally described by the Bose-Hubbard Hamiltonian [12], and inital work studied the superfluid-Mott insulator transition [13, 14]. Since then, much work has looked at lattices with lower dimensionality [15], novel geometries [16, 17], or modified tunneling [18, 19, 20, 21, 22, 23, 24].

In addition, because of their cold temperature and precise control, cold atoms

have become one of the primary systems for precision measurement [25]. One general method used is that of atom interferometery, which relies on the wave nature of quantum mechanics and can be explained in analogy with classical optical interferometry. In a traditional interferometer, a beam of light is split and sent along two paths. When the light is re-combined and measured, the light from the two paths interfere, and the interference pattern contains information about the difference in path lengths. For an atom interferometer, one takes advantage of the wave nature of cold atoms, running separate parts of the wavefunction along different paths, and thereby measuring the energy difference between the paths. This method has proved useful not only in studying fundamental physics [26, 27, 28], but also as a precise force sensor [29, 30, 31].

The experiments described in this thesis were done in Wolfgang Ketterle's Rubidium lab at MIT. This lab studies ultracold bosonic ^{87}Rb atoms in optical lattices, and in the past has been used to explore many topics, including superradiance [6], the quantum Zeno effect [32], and demagnetization cooling [33], and in recent years has focused on lattice physics. I begin in Chapter 2 by describing the theory of optical lattices and some background theory necessary to understand our system.

In Chapter 3, I discuss our work in simulating strong magnetic fields, where a charged particle in a uniform magnetic field undergoes cyclotron motion with a cyclotron orbit size of the same order as the lattice spacing. Then, the motion is described by the Harper-Hofstadter Hamiltonian, whose spectrum is given by the fractal Hofstadter's butterfly. The spectrum is interesting not only for its fractal nature, but also for its connection to toplogical physics. Where the vacuum has a Chern number, of exactly zero, many of the subbands of Hofstadter's butterfly have a non-zero Chern number. Since Chern numbers are topological invariants and must be integers, it cannot go smoothly from its non-zero value in the bulk of a system to zero outside it — the bandgap must close at the edge, allowing for gapless edge modes. Topological invariants are robust to local variations in system parameters, so these edge modes are "topologically protected" from lattice impurities or distortions. This inherent robustness makes topological materials interesting in themselves and

as a potential candidate for use in quantum computing.

In order to see these effects in a traditional material, one would need magnetic fields ∼10,000 T, which is clearly not feasible. Instead, we simulate the effect of this field by directly controlling the phase of tunneling elements in our lattice. By doing so, we can emulate the Aharanov-Bohm phases associated with such a high field. I present the first realization of a BEC in the Harper-Hofstadter Hamiltonian and demonstrate some of the properties of this Harper superfluid, including gauge-dependent observables.

In Chapter 4, I discuss superfluid shielding, which is a novel method to increase the coherence lifetime in separated quantum systems, like those in atom interferometers. One fundamental mechanism for the decay of phase coherence is quantum projection noise. When a coherent quantum system is split, there are unavoidable density fluctuations. If the systems are self-interacting, these density fluctuations get written into the relative phase between the subsystems, and therefore reduce the phase coherence and signal-to-noise in measurements. Because of this, most groups using atom interferometry work with atoms above the BEC transition point, where densities are low enough that interactions are negligible. However, this is the equivalent of using a white light interferometer, rather than a laser interferometer, which will in general have a much higher brightness.

Superfluid shielding gets around this issue, and allows for long coherence lifetimes, by using good interactions to zero out the effect of bad interactions. We immerse the separated quantum systems in a superfluid bath of a different spin state, which because it is superfluid, moves its density to exactly cancel the density fluctuations in the separated subsystems. Then, since for ^{87}Rb, all inter- and intra-spin interaction strengths are equal to the percent level, this cancels the effect of the density fluctuations on the relative phase between the separated subsystems. I present a theoretical analysis of this effect and demonstrate its ability to lengthen coherence times beyond the projection noise limit by using Bloch oscillations in a two-component ^{87}Rb BEC.

In Chapter 5, I present our work on the Heisenberg Hamiltonian, a paradigmatic description of systems with magnetic ordering. A system with two spin components

deep in the $n = 2$ Mott insulator can be mapped onto a spin-1 Heisenberg model, which has an additional phase that the spin-1/2 model does not have — the spin Mott insulator. This state is an insulator in both spin and charge space, and has gapped excitations, which should allow us to keep a lower entropy when we ramp to this phase from a BEC. Once there, we will be able to use a spin-dpenedent lattice to vary the inter-spin interaction strength and adiabatically enter other states that have magnetic ordering and gapless excitations. The first phase that we wish to ramp to is the xy-ferromagnet, which is a spin superfluid while still being an insulator in charge, demonstrating spin-charge separation. So far, we have achieved spin Mott insulators that are cold in spin space, but were initially unable to ramp into a cold xy-ferromagnet because of the large number of charge excitations. I discuss upgrades made to the experiment that have greatly reduced the charge temperature, along with future plans for our system.

Chapter 2

Optical Lattices

Lattice models are used in much of physics, from condensed matter [34] to high-energy physics [35, 36]. In the field of ultracold atoms, lattice models have been proposed and used to study topological physics [37, 38], magnetic phases [39, 40], and even dynamical gauge fields [38]. Optical lattices, which are created using coherent laser light, are a versatile tool for creating lattice potentials for ultracold atoms.

In this chapter, I first describe how to create an optical lattice using the AC Stark shift of a coherent laser beam. I then discuss the basic theory of particles in a lattice potential, including Bloch's theorem and bandstructure calculations. In deep lattices, the system can be described by the Bose-Hubbard Hamiltonian, which has superfluid and Mott insulating regions, and can easily be extended by adding external (possibly time-dependent) potentials or novel types of interactions.

2.1 Making an Optical Lattice

Optical lattice potentials can be formed using the AC Stark Shift [8, 9], which is the potential felt by atoms in an off-resonant oscillating electromagnetic field. Working in the dipole approximation and ignoring atomic motion, we write the interaction between the oscillating field and the atom as

$$H' = -\vec{d} \cdot \vec{E}(t) \tag{2.1}$$

where $\vec{d} = -e\vec{r}$ is the dipole operator, and $\vec{E} = E\hat{x}\cos(\omega t)$ is the electric field. For the scalar AC Stark shift, which is spin-independent and the primary component at large detunings, we can treat the atom as a two level system with ground state g and excited state i. We define the dipole matrix element between the two states

$$M_{gi} = \langle i | \vec{d} \cdot \hat{x} | g \rangle . \tag{2.2}$$

Note that we have left the electric field strength out of this definition, so $\langle i | H' | g \rangle = EM_{gi}$. Then with second order perturbation theory, we find that the energy shift is

$$\Delta E = 2\pi\alpha a_0^2 I |M_{gi}|^2 \left(-\frac{1}{\delta} + \frac{1}{\omega_{gi} + \omega} \right), \tag{2.3}$$

where α is the fine structure constant, a_0 is the Bohr radius, ω_{gi} is the atomic resonance frequency, and $\delta = \omega - \omega_{gi}$. We have included the electric field strength in the intensity $I = c\epsilon_0 E^2/2$. Now, if the intensity varies with position, we can treat ΔE as an external potential. These potentials, which we create with far-detuned lasers, are the primary tools used in the experiments described in this thesis.

The sign of the potential changes with detuning — a red-detuned laser beam creates an attractive potential, while a blue-detuned beam creates a repulsive potential. Our main trapping beams, which provide confinement on the scale of 10-100 μm, are made by focusing the output of a 1064 nm fiber laser. It is possible to make a lattice potential out of an array of independent dipole traps [41, 42], but doing so requires a large numerical aperture and precise control over many degrees of freedom. Instead, we make our optical lattices by retro-reflecting a laser beam focused on the atoms, which creates an intensity lattice with a spacing that is half of the laser wavelength. Unlike in [41, 42], we cannot move individual lattice sites around, but a retro-reflected lattice is much more stable: the spacing between lattice sites is set only by the laser wavelength, and the relative depths of lattice sites is determined by the Gaussian envelope of the beam, which can be much broader than the atomic cloud. This stability allows us to reach and maintain the colder temperatures required to study lattice physics mediated by tunneling and on-site interactions.

2.2 Theory of Particles in Lattice Potentials

Our neutral atoms in a one-dimensional optical lattice are then described by the single-particle Hamiltonian

$$H = \frac{p^2}{2m} + V_L \cos^2(k_L x) \tag{2.4}$$

where V_L is the height of the optical lattice potential and k_L is the wavevector $2\pi/\lambda$ of the lattice laser. This is the same form as a Hamiltonian describing electrons in a crystal lattice, and is the starting point for much of condensed matter physics. This connection both allows us to use theory tools first created for condensed matter systems, as well as use our cold atoms systems as analogues of interesting condensed matter systems.

2.2.1 Bloch's Theorem and Bandstructure

Our Hamiltonian breaks continuous translation symmetry, so momentum is not conserved, and the eigenstates do not have a definite momentum. However, there is still a discrete translation symmetry of $x \to x + a$, where $a = k_L/\pi$. Bloch's theorem [34] tells us that eigenstates of the Hamiltonian are also eigenstates of the discrete translation operator

$$\begin{aligned} T =& e^{ipa/\hbar} \\ T\psi(x) =& \psi(x+a)\,. \end{aligned} \tag{2.5}$$

We can explicitly split out this eigenvalue and write the wavefunction as

$$\psi(x) = e^{iqa}\phi_q(x) \tag{2.6}$$

where q is the eigenvalue of T, known as the quasimomentum, and $u_q(x)$ is periodic in x with period a. The quasimomentum is often similar to real momentum, but it is only defined on $(-\pi/a, \pi/a]$ and is only conserved modulo $2\pi/a$. We find that the

quasimomentum part of the ansatz factors out:

$$\begin{aligned} H\psi(x) =& He^{iqa}\phi_q(x) \\ =& e^{iqa}H_q\phi_q(x)\,, \end{aligned} \tag{2.7}$$

where

$$H_q = \frac{(p+q)^2}{2m} + V_L cos^2\left(k_L x\right), \tag{2.8}$$

and q is now a c-number, rather than an operator. Thus, each $\phi_q(x)$ is given by the eigenfunctions of the appropriate H_q, which have the form of Mathieu functions. However, Mathieu functions can be hard to work with, so for our numerical calculations, we use a plane wave expansion

$$\phi_q(x) = \sum_j c_j^{(q)} e^{2\pi i j x/a} \tag{2.9}$$

where we have chosen plane waves that are harmonics of the lattice spacing a, which enforces the translation symmetry of $\phi_q(x)$. In this basis, H_q can be written as a tri-diagonal matrix with the elements

$$\begin{aligned} H_{q;j,j} =& \left(2j + q/k_L\right)^2 E_{\mathrm{R}} + V_L/2 \\ H_{q;j,j\pm1} =& -V_L/4 \end{aligned} \tag{2.10}$$

and all other elements 0. We have defined the recoil energy scale $E_{\mathrm{R}} = \hbar^2 k_L^2/2m$. By numerically diagonalizing H_q for each q, we can determine the bandstructures as shown in Figure 2-1. We find that using a maximum $|j|$ of 15 provides good results for the lowest three bands.

An intuitive way to understand the off-diagonal terms is most obvious in an optical lattice, as opposed to a crystal lattice. In Section 2.1, we described the AC Stark shift in second-order pertubation theory where we ignored atomic motion. We can read the term $E^2 \left|M_{gi}\right|^2/\delta$ as the following proces: A ground state atom accepts a photon from the laser field with matrix element EM_{gi}, and is virtually excited into state i with an energy deficit of δ. Then, the atom is de-excited back to the ground

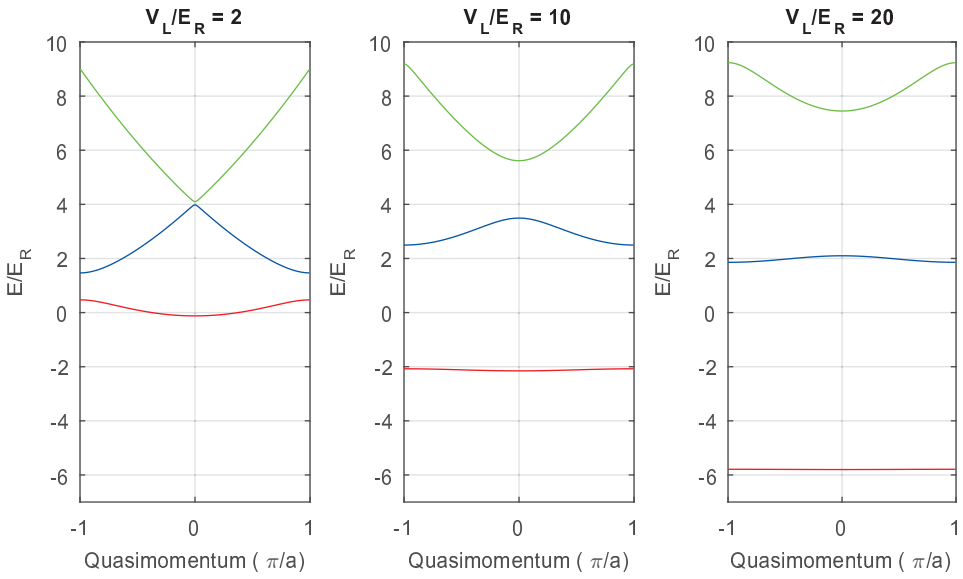

Figure 2-1: Bandstructure of an atom in an optical lattice. Here we plot the lowest three bands as a function of quasimomentum at different lattice depths. Note that at low lattice depths, the bands almost follow the free particle parabolic dispersion, with small avoided crossings. At higher lattice depths, the bands become flatter and the bandgaps approach the harmonic oscillator frequency for a single lattice site.

state by emitting a photon into the laser field, this time with matrix element EM_{gi}^*. Now in the real system, we need to take momentum conservation into account, and in an optical lattice composed of two retro-reflected laser beams, there are two options. First, if the emitted photon is in the same beam as the exciting photon, then the atom does not pick up any momentum. This is where the $V_L/2$ on the diagonal of H_q comes from. On the other hand, the atom could accept a photon from the input beam and emit into the retro-reflected beam, or vice versa, which will give it a momentum kick of $2\hbar k_L$. This takes $j \to j \pm 1$, and gives the off-diagonal terms of H_q. It is these terms that give rise to the avoided crossings seen in Figure 2-1.

2.2.2 Wannier Functions

Once we have solved for the bandstructure, we can use the Bloch functions to define another set of orthogonal basis states, which are equivalent to position eigenstates in the same way that Bloch states are the lattice equivalent of momentum eigenstates. These are known as the Wannier functions [43] and for a state localized at lattice site

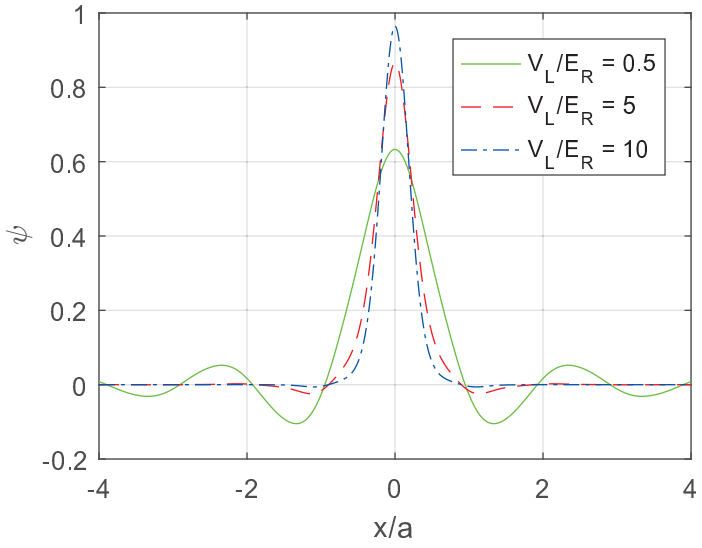

Figure 2-2: Maximally-localized Wannier functions in the lowest band. We have chosen a phase convention so that the wavefunction is purely real, and have plotted the maximally localized Wannier functions at varying lattice depths. At low lattice depths, the wavefunction has significant weight outside of the lattice site, but at higher lattice depths, it rapidly approaches the ground state wavefunction of the harmonic oscillator.

x_i are given by

$$w_n(x - x_i) = \sqrt{N} \int_{-\pi/a}^{\pi/a} \phi_q^{(n)}(x)\, e^{-iqx_i/\hbar} dq, \tag{2.11}$$

where n is the band index and N is a normalization constant. Note that the $\phi_q^{(n)}(x)$ are only defined up to a phase, and only one phase convention will provide the maximally localized functions that we want. This can be done by direct minimization [44] or by using the phase convention in [43]. For the ground band and even excited bands, maximally localized Wannier functions are produced by choosing all $c_j^{(q)}$ to be purely real. For odd excited bands, we choose all $c_j^{(q)}$ to be purely imaginary. In Figure 2-2, I have plotted the normalized ground band Wannier functions at various lattice depths. Note that at low lattice depths, the Wannier function has some weight outside the center well, but these parts quickly decay with increasing lattice depth, and the Wannier functions rapidly approach the eigenstates of the Harmonic oscillator.

2.3 Bose-Hubbard Hamiltonian

In a deep lattice, i.e. the single band approximation, we can write our Hamiltonian in terms of the Wannier functions

$$H = -t \sum_{\langle i,j \rangle} a_i^\dagger a_j \tag{2.12}$$

where a_j is the annihilation operator for the lowest band Wannier function on site j, and $\langle i, j \rangle$ denotes pairs of nearest neighbors. We find the tunneling parameter, t, by looking at the matrix element between neighboring Wannier functions

$$t = \int d\vec{r}\, w(\vec{r} - \vec{r}_0)^* \left(\frac{p^2}{2m} + V_L cos^2 \left(k_L x \right) \right) w(\vec{r} - \vec{r}_1) \,. \tag{2.13}$$

The system becomes more interesting when we add interactions between the atoms on a given site. Doing so gives us the Bose-Hubbard Hamiltonian [12]

$$H = -t \sum_{\langle i,j \rangle} a_i^\dagger a_j + \frac{U}{2} \sum_i n_i \left(n_i - 1 \right) \tag{2.14}$$

with the number operator $n_i = a_i^\dagger a_i$ as usual. The interaction parameter U is given by the squared on-site density

$$U = \frac{4\pi\hbar^2 a_s}{m} \int d\vec{r}\, w(\vec{r} - \vec{r}_0)^{*2} \, w(\vec{r} - \vec{r}_0)^2 \,, \tag{2.15}$$

where a_s is the s-wave scattering length.

The Bose-Hubbard Hamiltonian is the starting point for all of the research done in this thesis, and one of its main advantages is how easy it is to modify to take into account other potentials, interactions, or tunneling types. The most common extension is that of an external confining potential and the local density approximation. For an external potential $V_{ext}(\vec{r})$, we add a term to the Hamilonian of the form $\sum_i V_{ext}(\vec{r_i})\, n_i$, and to take into account the chemical potential, we add a term $-\mu \sum_i n_i$. We can

combine these two terms in the "local density approximation"

$$H = -t \sum_{\langle i,j \rangle} a_i^\dagger a_j + \frac{U}{2} \sum_i n_i \left(n_i - 1 \right) - \sum_i \mu_i n_i \tag{2.16}$$

with $\mu_i = \mu - V_{ext}(\vec{r}_i)$.

2.3.1 Superfluid to Mott Insulator Transition

Now let us look at the phases in a d-dimensional isotropic lattice with one spin component. There are two clear extremes: the first is known as the superfluid phase, and the second as the Mott insulator, both of which are accessible in optical lattices [13, 14].

The superfluid phase occurs when the Hamiltonian is dominated by $-t \sum_{\langle i,j \rangle} a_i^\dagger a_j$ and has all atoms in the same Bloch state, sitting at the bottom of the lowest band. In the mean-field, the superfluid has an order parameter

$$\psi = \langle a_i \rangle = \left\langle a_i^\dagger \right\rangle = \sqrt{n_i}. \tag{2.17}$$

At the other extreme, the Hamiltonian is dominated by the interaction term

$$H = \frac{U}{2} \sum_i n_i \left(n_i - 1 \right) - \sum_i \mu_i n_i \tag{2.18}$$

and becomes a sum of purely local energy terms. This leads to a ground state known as the Mott insulator with exactly $N_i = \lfloor (\mu/U) \rfloor + 1$ atoms on each site i.

To find the phase transition from a superfluid to a Mott insulator, we first write the Hamiltonian for a single lattice site in the mean field approximation [13]

$$H = zt \left(\frac{U}{2zt} n_i \left(n_i - 1 \right) - \frac{\mu_i}{zt} n_i - \left(a_i + a_i^\dagger \right) \psi + \psi^2 \right) \tag{2.19}$$

where $z = 2d$ is the number of nearest neighbors of a given site. According to Landau's theory of phase transitions, a second order phase transition from $\psi = 0$ (a Mott insulator) to non-zero ψ (a superfluid) will occur when $d^2E/d\psi^2 = 0$. Therefore,

we will work in the low t/U limit, splitting the Hamiltonian into the zeroth order and perturbative parts as

$$\begin{aligned} H_0 =& \frac{U}{2} n_i \left(n_i - 1\right) - \mu_i n_i \\ V =& zt \left(\left(a_i + a_i^\dagger \right) \psi + \psi^2 \right). \end{aligned} \tag{2.20}$$

The zeroth-order energy is then just

$$E^{(0)} = \frac{U}{2} N_i \left(N_i - 1\right) - \mu N_i \tag{2.21}$$

with N_i defined as above. The second order energy term is found to be

$$E^{(2)} = zt\psi^2 \left(\frac{N_i zt}{U\left(N_i - 1\right) - \mu_i} + \frac{zt\left(N_i + 1\right)}{\mu - UN_i} \right) \tag{2.22}$$

which leads to a phase boundary at

$$\frac{\mu_i}{U} = \frac{1}{2}\left(2N_i - 1 - \frac{zt}{U}\right) \pm \frac{1}{2}\sqrt{1 - \frac{2zt}{U}\left(2N_i + 1\right) + \left(\frac{zt}{U}\right)^2}. \tag{2.23}$$

Figure 2-3 shows the phase diagram for a three-dimensional isotropic system. The Mott insulating lobes are clearly visible and in order of increasing μ_i are associated with $N_i = 1, 2, 3, \ldots$, and as expected, decrease in size as we increase t/U. Since our atoms are held in an external harmonic trap, μ_i varies from 0 to μ across the cloud, and so any given cloud will sample a vertical line in Figure 2-3a. Since we know the form of μ_i, though, we can calculate which Mott shells are present in our system and what their relative weight is. For some work done in this thesis, it is important that we fill the $N_i = 1$ or $N_i = 2$ shell and not have any atoms in $N_i = 3$ or higher. We use the above work to calculated our expected maximum filling, and then confirm it via clock shift spectroscopy [45].

2.3.2 Wannier-Stark Ladder

Another useful extension of the Bose-Hubbard Hamiltonian describes particles in a tilted lattice, which is used as an integral part of two of the projects in this thesis.

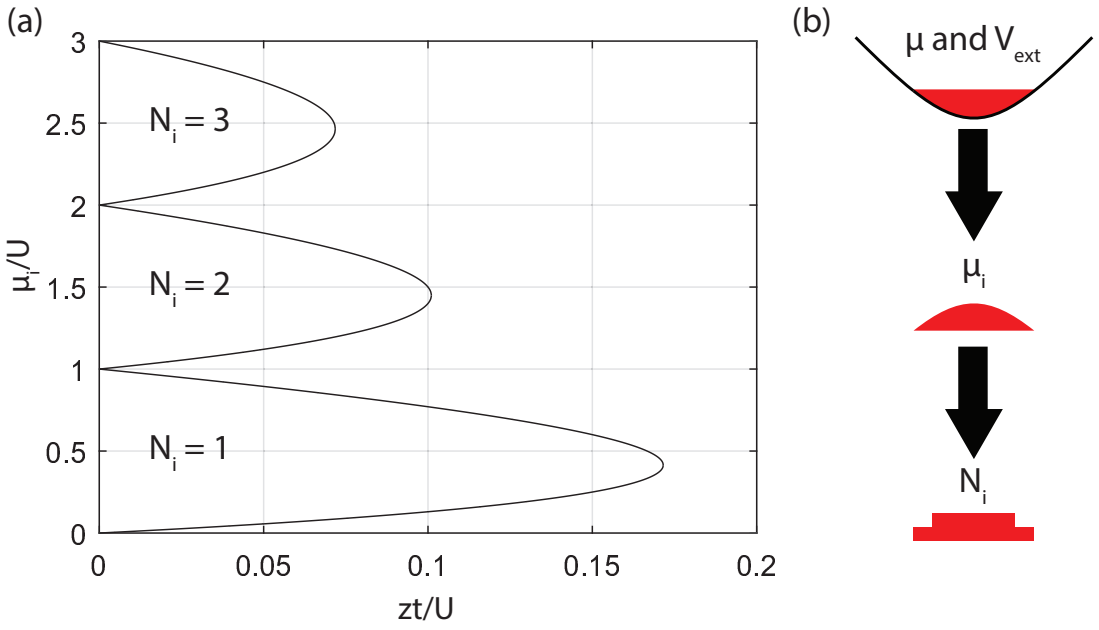

Figure 2-3: Phase diagram of the SF to MI transition and the LDA. (a) Calculated mean-field phase diagram of the superfluid to Mott insulator transtion, up to a filling factor of three. Each lobe is labeled with the corresponding filling factor, and the area outside the lobes is in the superfluid state. (b) Cartoon of the local density approximation. The cloud has a constant chemical potential μ and is held in an external trapping potential V_{ext}. Then for each lattice site, we find $\mu_i = \mu - V_{ext}$. Once μ_i is known, we can use Figure 2-3a to determine the filling at each lattice site N_i.

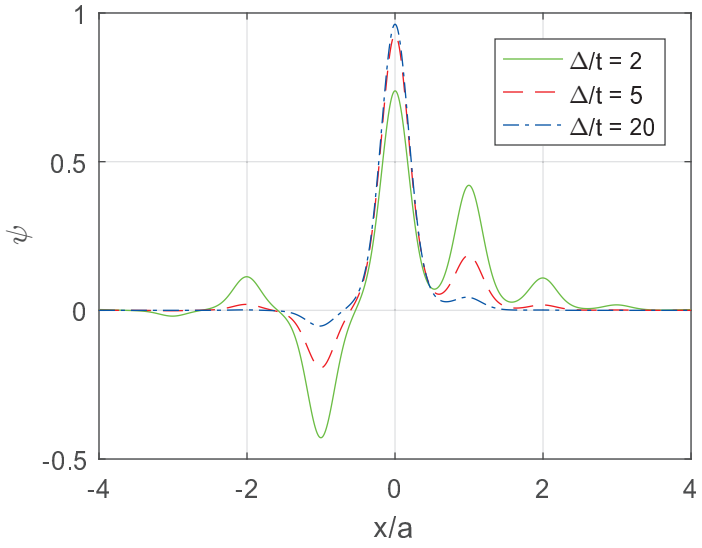

Figure 2-4: Wannier-Stark wavefunctions at varying tilts. Here, we plot the wavefunction of Wannier-Stark states in a lattice of 10 E_R with varying tilt-to-tunneling ratios Δ/t. (As in Figure 2-2, the phase convention is chosen so that the wavefunctions are purely real.) The wavefunctions all have some component on neighboring lattice sites, but this is strongly suppressed when $\Delta \gg t$.

If we define the energy tilt per lattice site Δ, the single-particle Hamiltonian is given by [46]

$$H = -\sum_l t\left(a_l^\dagger a_{l+1} + H.C.\right) + \Delta\sum_l l a_l^\dagger a_l. \tag{2.24}$$

For simplicity, we define $\alpha = t/\Delta$ and $\epsilon = E/t$. If we write the wavefunction in the basis of Wannier states $|\psi\rangle = \sum_l c_l a_l^\dagger |0\rangle$,

$$\begin{aligned} E|\psi\rangle &= H|\psi\rangle \\ \epsilon|\psi\rangle &= \left[-\sum_l\left(a_l^\dagger a_{l+1} + a_{l+1}^\dagger a_l\right) + \frac{1}{\alpha}\sum_l l a_l^\dagger a_l\right] \\ \epsilon\alpha\sum_j c_j a_j^\dagger|0\rangle &= \sum_j c_j\left(-\alpha a_{j-1}^\dagger - \alpha a_{j+1}^\dagger + j a_j^\dagger\right)|0\rangle. \end{aligned} \tag{2.25}$$

Then by detailed balance,

$$\begin{aligned} \epsilon\alpha c_j &= -\alpha\left(c_{j+1} + c_{j-1}\right) + j c_j \\ c_{j+1} + c_{j-1} &= \frac{j - \epsilon\alpha}{\alpha} c_j. \end{aligned} \tag{2.26}$$

This matches the Bessel function recurrence relation:

$$Z_{n+1} + Z_{n-1} = \frac{2n}{x} Z_n(x) \tag{2.27}$$

and so the eigenstate coefficients are

$$c_l = AJ_{\epsilon\alpha - l}(2\alpha) + BY_{\epsilon\alpha - l}(2\alpha) \tag{2.28}$$

where J_l and Y_l are Bessel functions of the first and second kind, respectively. In general, A and B are given by the boundary conditions. For an infinite lattice, we can set $B = 0$ to get localized states, which we call Wannier-Stark states. For $\epsilon = 0$, the eigenstate takes the form

$$|\psi_{\epsilon=0}\rangle = \sum_l J_{-l}\left(\frac{2t}{\Delta}\right) a_l^\dagger |0\rangle . \tag{2.29}$$

I.E. It is centered on site 0, and sites l away from the center have weights $\left|J_l\left(\frac{2t}{\Delta}\right)\right|^2$. If we change the energy by Δ then the Wannier-Stark state is simply translated one site left or right. In the case of large $\Delta > t$, tunneling is suppressed by energy conservation and the states become more localized about a single site. Figure 2-4 shows the probability distribution associated with the Wannier-Stark state centered about site 0 at several different tilt values.

Chapter 3

Simulating Strong Magnetic Fields

Topological states of matter are an active area of research in physics, and are strongly associated with high magnetic fields. While topological single-particle physics is well understood, there are many open questions about the interaction of topological materials with strong interactions [47, 48], with connections to the fractional quantum Hall effect [49] and Majorana fermions [50, 51, 52].

In neutral atoms, synthetic magnetic fields have previously been created through use of the Coriolis force in rotating systems [53, 5, 54], Berry's phases in multiple hyperfine states [18, 19, 20, 21, 22], or lattice shaking [23, 24]. Much recent work has focused on the Harper-Hofstadter Hamiltonian, which describes particles in a lattice subject to a magnetic field strong enough that the cyclotron orbit length becomes comparable to the lattice spacing [55, 56, 57]. The comparable length scales lead to the fractal structure of Hofstadter's butterfly, which has sub-bands with non-zero Chern numbers [58]. Previous work on uniform magnetic fields has either been limited in the magnitude of the synthetic field possible or plagued by heating. Bose-Einstein condensation has previously been achieved only in staggered flux configurations [59, 23] or small ladder systems [60, 61].

In this chapter, I present the first observation of Bose-Einstein condensation in the bulk Harper-Hofstadter Hamiltonian. I first explain some of the interesting properties of the Harper-Hofstadter Hamiltonian and describe how we use laser-assisted tunneling to imprint the proper phase on the wavefunction. I then describe the ex-

perimental sequence and upgrades that were required to achieve a cold superfluid in the Harper-Hofstadter Hamiltonian. Our observations directly show the broken translational symmetry of the vector potential, despite the uniform magnetic field, and demonstrate the non-gauge invariant momentum distribution and degeneracy of the ground band [62, 63, 64]. We observe the result of the addition of interactions and make a Harper superfluid near the Mott Insulating transition. Finally, I end with a discussion of the observed lifetime and some heating processe that may be relevant.

This chapter covers material from [65].

3.1 Harper-Hofstadter Hamiltonian

A two-dimensional system of charged particles in both a lattice potential and a high transverse magnetic field are described by the Harper-Hofstadter Hamiltonian [55, 56, 57]

$$H = \sum_{m,n} \left(-K\, e^{-i\phi_{m,n}} \hat{a}^{\dagger}_{m+1,n} \hat{a}_{m,n} - J\, \hat{a}^{\dagger}_{m,n+1} \hat{a}_{m,n} \right) + \text{H.c.} \tag{3.1}$$

where K and J are real tunneling coefficients and $a_{m,n}$ and $a^{\dagger}_{m,n}$ are the annihiliation and creation operators for site (m, n). $\phi_{m,n}$ is a spatially dependent phase

$$\phi_{m,n} = \frac{1}{\hbar} \int_{x_m}^{x_{m+1}} \vec{A} \cdot d\vec{r} \tag{3.2}$$

with the charge included in the vector potential $\vec{A}$. For convenience, we choose a gauge which has no component in the y direction. We want the vector potential to correspond to a constant magnetic field in the $\hat{z}$ direction, so we say

$$\begin{aligned} \vec{B} &= \nabla \times \vec{A} \\ B_0 \hat{z} &= \nabla \times A\hat{x} \\ &= \frac{\partial}{\partial z} A\hat{y} - \frac{\partial}{\partial y} A\hat{z}. \end{aligned} \tag{3.3}$$

This tells us that the form of $\vec{A}$ must be $(-By + f(x))\,\hat{x}$, where $f(x)$ is an arbitrary function of x only. This is an example of gauge freedom, and the choice of $f(x)$ does

not change the physics of the system. Note that we later discuss some experimental results that appear to be gauge dependent, but they rely on the specifics of the simulation that we use and are not present in the real system discussed here. Most theoretical work on the Harper-Hofstadter Hamiltonian has used the Landau gauge $\vec{A} = -By\hat{x}$, which we will use in this section.

For intuition about the form of the Hamiltonian, first recall the Aharanov-Bohm effect, which is most easily explained by looking at a closed adiabatic path P. The definition of adiabaticity tells us that applying a closed-loop adiabatic transformation leaves the probability distribution the same $|\psi_i(x)|^2 \underset{P}{\rightarrow} |\psi_f(x)|^2 = |\psi_i(x)|^2$, which implies that the only possible change to $\psi_i(x)$ is a phase: $\psi_f(x) = \exp[i\phi_{\mathrm{AB}}]\,\psi_i(x)$. This phase is the Aharanov-Bohm phase, given by

$$\phi_{\mathrm{AB}} = \frac{1}{\hbar}\oint_P \vec{A}\cdot d\vec{r} = \frac{\Phi}{\hbar}, \tag{3.4}$$

where Φ is the enclosed magnetic flux. Now we look at a particle described by the Harper-Hofstadter Hamiltonian in Equation 3.1 that is initially localized at $(0,0)$, and then takes a counterclockwise path $(0,0) \rightarrow (1,0) \rightarrow (1,1) \rightarrow (0,1) \rightarrow (0,0)$. The y legs of this path are mediated by real tunneling, and so add no phase to the wavefunction. On the other hand, the forward move from $(0,0) \rightarrow (1,0)$ and the backward move from $(1,1) \rightarrow (0,1)$ add a phase of $\phi_{0,0} - \phi_{0,1}$. In the Landau gauge,

$$\begin{aligned}\phi_{m,n} &= \frac{1}{\hbar}\int_{x_m}^{x_{m+1}} -By\hat{x}\cdot d\vec{r} \\ &= \frac{-Bna^2}{\hbar} \\ &= \frac{-\Phi n}{\hbar},\end{aligned} \tag{3.5}$$

and thus, $\phi_{0,0} - \phi_{0,1} = \frac{\Phi}{\hbar} = \phi_{\mathrm{AB}}$. From here, it is simple to see that this is true for every closed path in the Harper-Hofstadter Hamiltonian.

3.1.1 Hofstadter's Butterfly

The most striking property of the Harper-Hofstadter Hamiltonian is that it leads to a fractal bandstructure known as Hofstadter's Butterfly, shown in Figure 3-1 for a symmetric lattice $K = J$. We define the normalized flux $\alpha = Ba^2/\Phi_0$, or the ratio of the flux enclosed in a single lattice unit cell to the magnetic flux quantum $\Phi_0 = h/e$, which gives a phase of 2π when a particle circles it. In a normal material, with $a \sim 1$ Å, we would need a magnetic field of $\sim 10,000$ T to have $\alpha = 1$.

Let us first build some intuition about the form of Hofstadter's butterfly. At zero flux, the unit cell is simply given by the lattice, and so the lowest band covers the normal Brillouin zone, with an energy ranging from $-4J$ to $4J$. At $\alpha = 1$, any closed path that a particle takes encloses an integer number of flux quanta, and so the particle picks up a phase that is a multiple of 2π, which is indistinguishable from zero. We can therefore say that Hofstadter's butterfly should be the same at α and $\alpha + 1$. A system at $-\alpha$ is the same as a system with α and $\hat{z} \to -\hat{z}$, so the associated energies should be the same. Combining the two previous symmetries tells us that the butterfly is symmetric about $\alpha = 1/2$. Finally, for rational fluxes of the form $\alpha = p/q$ for $p, q \in \mathbb{Z}$, we can understand the structure of the subbands. If p and q are relatively prime, then a particle must enclose q lattice unit cells to enclose an integer number of flux quanta. We call this larger cell the magnetic unit cell, and it provides the translation symmetry for the system. Since it is q times bigger than the lattice unit cell, the new Brillouin zone is then q times smaller, and the ground band is split into q subbands. In Figure 3-1, this is obvious for $\alpha = 1/3$ and $1/4$. For $\alpha = 1/2$, which is the magnetic field that we have simulated in this chapter, a full bandstructure calculation shows that there are in fact two subbands, which are connected at Dirac points.

For a more quantitative description of Hofstadter's butterfly, we follow his original paper [55, 56, 57], which begins by treating the wavefunction as a sum over Wannier

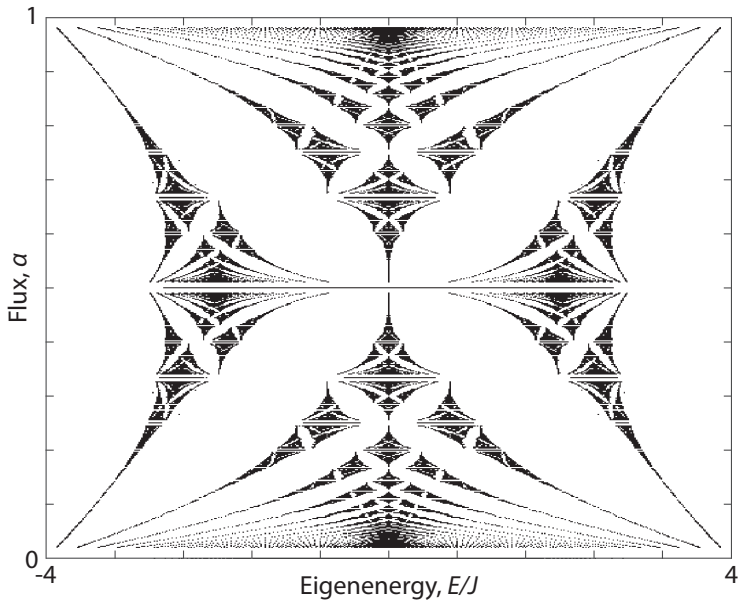

Figure 3-1: The fractal spectrum of the Harper-Hofstadter Hamiltonian, known as Hofstadter's butterfly. The vertical axis is the flux per unit cell, or α, and the horizontal axis is energy. Each filled point represents an eigenstate of the system under a flux α with a corresponding eigenenergy.

functions localized at each lattice site m, n,

$$|\psi\rangle = \sum_{m,n} c_{m,n} |m, n\rangle \,. \tag{3.6}$$

Using the Landau gauge, $\vec{A} = -By\hat{x} = -Bna\hat{x} \rightarrow \phi_{m,n} = -2\pi\alpha n$, we find the following relation between coefficients:

$$e^{i2\pi\alpha n} c_{m+1,n} + e^{-i2\pi\alpha n} c_{m-1,n} + c_{m,n+1} + c_{m,n-1} = -\frac{E}{J} c_{m,n}. \tag{3.7}$$

We make the ansatz that $c_{m,n}$ is separable into $\exp[ik_x am]\, g(n)$, and then find a recursion relation

$$2\cos(2\pi\alpha n + k_x a)\, g(n) + g(n+1) + g(n-1) = -\frac{E}{J} g(n) \,. \tag{3.8}$$

Then to numerically calculate the Harper Hamltonian as in Figure 3-1, we assume a lattice of sufficiently large size N with periodic boundary conditions. For rational

$\alpha \in [0, 1]$ and $k_x a \in [-\pi, \pi]$, we plot the eigenenergies, revealing the fractal structure of Hofstadter's butterly.

3.2 Raman tunneling

The Harper-Hoftsadter Hamiltonian normally describes *charged* particles in a high magnetic field, but we are working with *neutral* bosons of ^{87}Rb. Equation 3.1 tells us that the dynamics that we are interested in fundamentally come not from the charge, but from the phase pattern imprinted during tunneling. Enforcing real tunneling is relatively easy — we just put our atoms in a two-dimensional optical lattice. However, adding a complex phase to the tunneling coefficient is more involved.

In order to remove the real tunneling coefficient along the x direction, we apply a strong energy gradient, as shown in the schematic Figure 3-2. The tilt per lattice site Δ must be greater than the bandwidth of the untilted system, but smaller than the bandgap. Then energy conservation freezes out normal tunneling. We can restore tunneling by use of a pair of Raman lasers with a frequency difference $\delta\omega = \Delta$. Then, by accepting a photon from one laser and emitting into the other, an atom can hop down one site and still conserve energy. When it does so, if the Raman lasers are not collinear, the atom must also pick up a momentum kick $\delta\vec{k} = \vec{k}_1 - \vec{k}_2$, which is what determines the phase of our laser-induced tunneling. To provide intuititon for how a momentum kick turns into a complex tunneling element, recall that a momentum eigenstate has the form $\psi_k = \exp\left[i\vec{k}\cdot\vec{r}\right]$, i.e., a spatially dependent phase. Instead of explicitly thinking of momentum conservation for each tunneling event, we can factor it into the tunneling term $K\exp\left[i\phi_{m,n}\right]$, where

$$\begin{aligned} \phi_{m,n} &= \delta\vec{k}\cdot\vec{r}_{m,n} \\ &= m\ \delta k_x a + n\ \delta k_y a. \end{aligned} \tag{3.9}$$

This gives us an effective flux of $\alpha = \delta k_y a/2\pi$, which is tunable simply by changing the angle between the two Raman lasers.

For our specific implementation, our Raman lasers are far-detuned from the atomic

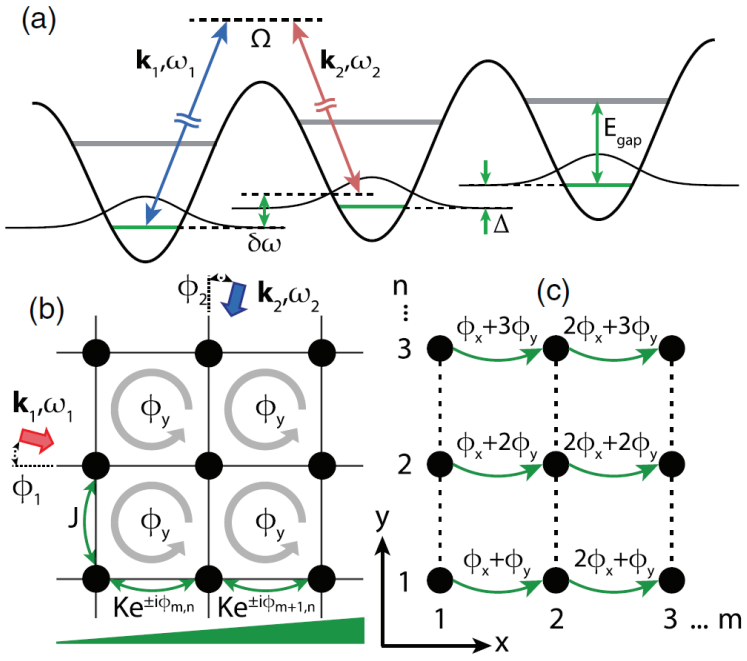

Figure 3-2: Schematic of our laser assisted tunneling setup. (a) We suppress normal tunneling in the x direction by applying a strong tilt Δ. It is then re-established by a two-photon process with two Raman beams whose frequencies are offset by $\delta\omega = \Delta$. (b) The Raman lasers are at an angle to each other, and so impart momentum with each x-tunneling event, which is equivalent to a complex tunneling parameter. The lattice is untilted along y, and so has purely real tunneling. (c) Phase pattern of the tunneling. In our gauge, $\phi_x = \phi_y = \pi$.

resonance. This allows us to ignore light scattering, and should lead to long lifetimes [21, 22]. In addition, it allows us to treat the effect of our Raman beams as a classical external potential. The interference of the two Raman lasers gives a "running standing wave" with an intensity proportional to $\sin\left(\delta\vec{k}\cdot\vec{r}-\frac{k_x a}{2}-\Delta t\right)$, oscillating at the difference of the two frequencies and moving in the direction of $\delta\vec{k}$. (Here, the term $\frac{k_x a}{2}$ is purely for convenience and does not change the physics.) Next, we can quantitatively analyze the physical system and show that it maps to the Harper-Hofstadter Hamiltonian. The physical singe-particle Hamiltonian is as follows:

$$H=\frac{\vec{p}^2}{2m}+V_{\text{latt}}(\vec{r})-\frac{\Delta}{a}x+\Omega\sin\left(\delta\vec{k}\cdot\vec{r}-\frac{k_x a}{2}-\Delta t\right), \tag{3.10}$$

where V_{latt} is the normal two-dimensional lattice potential, and Ω is the AC Stark shift associated with the Raman lasers. If we restrict ourselves to the first band, we can write the Hamiltonian in a localized basis of Wannier functions in the y-direction and Wannier-Stark functions in the x direction:

$$\begin{aligned}H=\sum_{m,n}\Big[&-m\Delta\left|m,n\right\rangle\left\langle m,n\right|-J\left|m,n+1\right\rangle\left\langle m,n\right|+h.c.\\&\sum_{m',n'}\Omega\left|m',n'\right\rangle\left\langle m',n'\right|\sin\left(\delta\vec{k}\cdot\vec{r}-\frac{k_x a}{2}-\Delta t\right)\left|m,n\right\rangle\left\langle m,n\right|\Big].\end{aligned} \tag{3.11}$$

To calculate the Raman matrix element, we shift the center and define $\theta_{m,n}=\Delta t-\delta\vec{k}\cdot\vec{r}_{m,n}=\Delta t-\phi_{m,n}$:

$$\left\langle m,n\right|\sin\left(\delta\vec{k}\cdot\vec{r}-\frac{k_x a}{2}-\Delta t\right)\left|m+l,n+p\right\rangle=\left\langle 0,0\right|\sin\left(\delta\vec{k}\cdot(\vec{r}+\vec{r}_{m,n})-\frac{k_x a}{2}-\Delta t\right)\left|l,p\right\rangle. \tag{3.12}$$

We split the sin function, and in the tight binding limit, we have the following rela-

tions:

$$\begin{aligned}
\langle 0|\sin(k_y y)\,|p=0\rangle &= 0\\
\langle 0|\cos(k_y y)\,|p=0\rangle &= 1\\
\langle 0|\sin(k_x x)\,|l=0\rangle &= 0\\
\langle 0|\cos(k_x x)\,|l=0\rangle &= 1\\
\langle 0|\sin(k_x\,(x-a/2))\,|l=1\rangle &= \Phi_x \approx -2J\frac{\sin(k_x a/2)}{\Delta}\\
\langle 0|\cos(k_x\,(x-a/2))\,|l=1\rangle &= 0.
\end{aligned} \tag{3.13}$$

Plugging these into the Hamiltonian gives us:

$$\begin{aligned}
H = \sum_{m,n}\Big[&(-m\Delta - \Omega\sin(\theta_{m,n}+k_x a/2))\,|m,n\rangle\langle m,n|\\
&+\Omega\Phi_x\cos\theta_{m,n}\,|m+1,n\rangle\langle m,n| - J\,|m,n+1\rangle\langle m,n| + h.c.\Big].
\end{aligned} \tag{3.14}$$

Finally, we move into the rotating frame given by

$$U = \exp\left[i\sum_{m,n}\left(m\Delta t - \frac{\Omega}{\hbar\Delta}\cos\left(\theta_{m,n}+\frac{k_x a}{2}\right)\right)\right]|m,n\rangle\langle m,n|\,, \tag{3.15}$$

which cancels the diagonal terms, and gives off-diagonal terms:

$$\begin{aligned}
\langle m+1,n|\,H\,|m,n\rangle =& \Omega\Phi_x\cos(\Delta t-\phi_{m,n})\,e^{-i\omega t}\sum_r J_r\left(\frac{2\Omega}{\hbar\Delta}\sin\left(\frac{k_x a}{2}\right)\right)e^{ir(\Delta t-\phi_{m,n})}\\
\langle m,n+1|\,H\,|m,n\rangle =& -J\sum_r J_r\left(\frac{2\Omega}{\hbar\Delta}\sin\left(\frac{k_y a}{2}\right)\right)e^{ir(\Delta t+(k_x-k_y)a/2-\phi_{m,n})}.
\end{aligned} \tag{3.16}$$

Here, we have used the identity $e^{ix\sin\theta} = \sum_r J_r(x)\,e^{ir\theta}$, where J_r are the Bessel functions of the first kind. Averaging over a several Δ periods, and using Bessel

function identities, we find

$$\begin{aligned} Ke^{-i\phi_{m,n}} =& \Omega e^{-i\phi_{m,n}} \Phi_x J_1\left(\frac{2\Omega}{\hbar\Delta}\sin\left(\frac{k_x a}{2}\right)\right)\left(\frac{2\Omega}{\hbar\Delta}\sin\left(\frac{k_x a}{2}\right)\right)^{-1} \\ =& -JJ_1\left(\frac{2\Omega}{\Delta}\sin\left(\frac{k_x a}{2}\right)\right) \\ J =& -JJ_0\left(\frac{2\Omega}{\hbar\Delta}\sin\left(\frac{k_y a}{2}\right)\right). \end{aligned} \tag{3.17}$$

It is important to note here that, although we have previously stated that changing k_x merely leads to a gauge transformation, and does not change α, its value is important here. In the Landau gauge, with $k_x = 0$, the magnitude of the tunneling matrix element in the x-direction would be exactly zero. A non-zero k_x is necessary to the overlap integral that allows x-tunneling to happen!

3.3 Experiment

For our specific experiment, we use a 1064 nm laser to make the optical lattices, leading to either a two- or three-dimensional lattice potential with a spacing of 532 nm. For the Raman lasers, we use the same 1064 nm source, and we send one beam along each lattice direction, which provides a momentum kick with $\delta k_y a = \delta k_x a = \pi$, leading to an effective flux of $\alpha = 1/2$. We attempted several experimental sequences, which I will discuss below, all of which follow the same basic formula. We start with a BEC in an optical lattice before applying a tilt and turning on resonant Raman beams. After some hold time, we snap off all potentials and use time-of-flight imaging to view the momentum distribution. The form of the superfluid peaks seen in the momentum distribution should demonstrate the symmetries of the Harper-Hofstadter Hamiltonian, and their visibility will tell us the ground state fraction.

For our initial attempts, we tried two different methods of creating a gradient. First, we attempted to ramp on a magnetic field gradient of about 1 kHz per lattice site. However, because of the configuration of our magnetic gradient coils, this was a slow process, taking a few hundred milliseconds. During the gradient ramp time, the

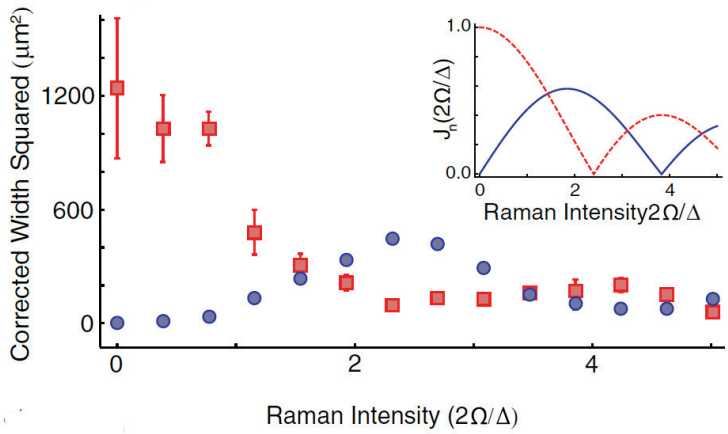

Figure 3-3: Demonstration of the amplitude of laser-assisted tunneling. Here we plot the increase in the squared width of a cloud 1500 ms after turning off dipole confinement and turning on laser-assisted tunneling through the use of Raman beams. The blue circles are the width in the tilt direction, and the red squares are in the transverse direction. The widths qualitatively agree with the Bessel function predictions shown in the inset.

system had time to undergo Bloch oscillations and totally dephase.

A faster method was to quickly turn off the confining dipole traps. After this ramp-off, the atoms are then exposed to the full force of gravity, which is also around 1 kHz per lattice site. However, this method had several limitations. First, with this method we were restricted to gradients less than or equal to the force of gravity, leaving us much closer to the tunnelling rate of around 50 Hz than the bandgap near 10 kHz. Second, there is not an easy way to shim the gradient, meaning that if the x lattice is not exactly aligned to true vertical, this will also induce Bloch oscillations in the y-direction. Finally, turning off the dipole traps imprints on the cloud not only the gradient that we want, but also curvature that is the inverse of the initial dipole confinement. This leads to the Raman beams moving in and out of resonance across the cloud, creating unwanted Bloch oscillations in the system.

Because of these non-idealities, we were initially unable to load the BEC into the ground state of the Harper-Hofstadter Hamiltonian. We were, however, able to demonstrate laser-assisted tunneling in Figure 3-3. We did this by turning off the dipole confinement at the same time as we turned on the tilt and laser-assisted

tunneling. We held for 1500 ms and measured the intrap width. We report $\sigma_f^2 - \sigma_i^2$, where $\sigma_{f,i}$ are the initial and final intrap widths, because we expect diffusive rather than ballistic expansion. As the Raman intensity is varied, we see qualitative agreement in both the laser-assisted tunneling amplitude and the transverse tunneling amplitude with the Bessel functions predicted in Equation 3.17.

3.3.1 Experimental Upgrades

In order to reach the ground state, we needed to make several upgrades to the experiment. The first two deal with problems alluded to above, while the third is of a more technical nature.

Fast Gradient Turn-on

In order to keep from having Bloch oscillations dephase during the tilt turn-on, we want to to be able to turn the gradient on faster than a Bloch oscillation. This is done using a hybrid gradient. First, we use a magnetic field gradient to levitate a BEC in the $|F = 1, m_f = -1\rangle$ spin state against gravity. At this point, the BEC feels a force of $-mg + mg = 0$, from gravity and the magnetic field gradient respectively. After ramping up the optical lattice, we perform a Landau-Zener RF sweep to flip all atoms into the $|2, -2\rangle$ state in 0.29 ms. The magnetic moment of $|2, -2\rangle$ is -2 times that of $|1, -1\rangle$, so the atoms now feel a force of $-mg + -2 \times mg = -3mg$, which for our atoms and lattice spacing is 3.420 kHz per lattice site. This method of creating a gradient gives us much higher gradients with much faster turn-on times.

Gradient Shimming

Now that we have a strong, fast gradient, it is important to ensure that it is exactly aligned with the x-lattice to prevent slow Bloch oscillations and dephasing in the transverse directions. To do this, we use amplitude modulation of the x-lattice as a calibration tool [66, 67]. First, we apply a tilt as described above. Instead of restoring tunneling using Raman lasers, we restore it by modulating the amplitude of the x-

lattice at the tilt frequency. It is possible to fully analyze the system as in Section 3.2, but here I will give only an intuitive explanation. We can view a lattice modulated at $\delta\omega$ as two sidebands at $\pm\delta\omega$ superposed on then normal lattice beam. If an atom accepts a photon from one of the sidebands and emits one into the main lattice beam, it will either move up or down one lattice site while conserving energy if $\delta\omega = \Delta$. This will restore *real* tunneling in the x-direction, and the lifetime of the superfluid in this system is then limited by any projection of the gradient along transverse lattice directions. We optimize the superfluid lifetime and therefore minimize the transverse gradient by using small shim coils along the two transverse lattice axes.

Phase Locking

The final major improvement of the experiment was to ensure the phase stability of the Raman lasers, since any relative phase slips are equivalent to randomly shifting the origin of the system. To provide passive stability, we sourced both Raman beams from the same fiber, and split the two beams on the machine table. Both beams are frequency shifted by identical 80 MHz acousto-optic modulators, set at 80 MHz and 80 MHz + Δ. After the beams propogate along the x- and y-directions, they are recombined on another beam cube, and their interference is measured on a photodiode. A lock-in amplifier set to Δ measures the phase fluctuations caused by non-common-mode vibrations and gives an error signal that is fed back to the phase of the RF drive of one of the acousto-optic modulators.

3.3.2 Final Experimental Sequence

The experiment begins with a nearly pure $|1,-1\rangle$ BEC of $\sim 1 \times 10^5$ ^{87}Rb atoms confined in a crossed dipole trap. We turn on a magnetic field gradient to levitate the atoms against gravity. From here, there are two possible sequences, which we term the "non-adiabatic" and "adiabatic" sequences, shown in Figure 3-4.

In the nonadiabatic sequence, the condensate is first adiabatically loaded into a two-dimensional optical lattice in the x (vertical) and y (horizontal) directions, with

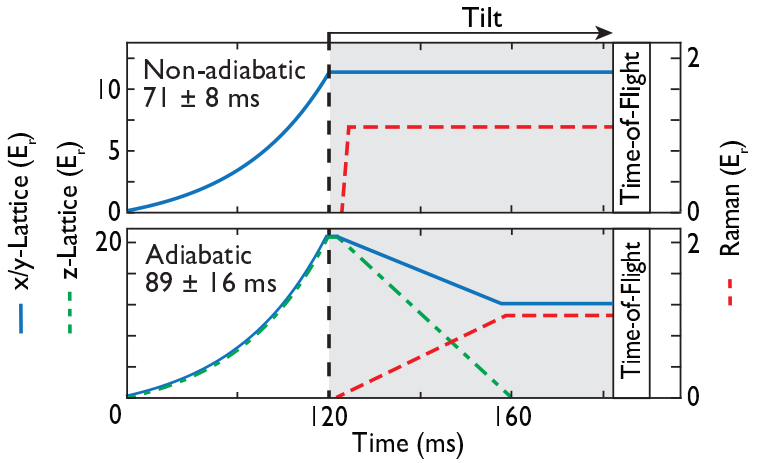

Figure 3-4: Experimental sequences for two different state preparation protocols. The non-adiabatic scheme switches suddenly from a standard 2D lattice to the Harper-Hofstadter lattice. The adiabatic protocol uses a quantum phase transition to the 3D Mott insulator as an intermediate step. For this, lattice beams are adiabatically ramped up in all three directions to 20 E_r to enter the Mott insulating phase, after which the hyperfine state is flipped with a 0.29 ms RF sweep as done in the non-adiabatic scheme. The lattices are then ramped down to their final values while the Raman lattice is ramped up in 35 ms. Lifetimes of both methods are given in the top corner of each figure; the lifetime of the adiabatic approach is measured from the end of the 35 ms ramp. Errors are statistical and given by the exponential fit to the decay of the peak visibility.

a depth of 11 recoil energies (E_R) in each direction. The third direction is confined only by the overall harmonic confinement, and so we have a two-dimensional array of tubes. At the same time, we raise a very weak Raman lattice ($< 0.1E_R$) and hold for a short time to allow phase lock to be achieved as discussed above.

Next, we apply a gradient in the method of Section 3.3.1 and linearly ramp the intensity of the Raman beams in 0.58 ms to $2\Omega/\Delta = 1.6$, where Ω is the two-photon Rabi frequency. We hold for a variable time before snapping off all laser beams to allow a 20 ms time-of-flight and absorption imaging to reveal the momentum distribution.

The non-adiabatic sequence is rather violent and quenches the system from a Hamiltonian where the ground state has a constant phase to one with a complex phase pattern. It is surprising that we can even form a Harper superfluid at all with this method, but we have found it to give consistently crisp superfluid peaks. This can be explained by looking at the third dimension. When we take absorption images, we automatically integrate over this dimension and therefore cannot see excitations in the z-direction. Since the system is only weakly trapped in z, we should treat each lattice site as a tube of about 500 atoms with gapless excitations along z. When we apply the tilt and laser-assisted tunneling, we perform a quench and create excitations in the phase between the tubes. As the system thermalizes, the z-direction acts as a bath and absorbs entropy created during the non-adiabatic sequence.

While this sequence works well for studying non-interacting physics, it does not allow a lattice in the third dimension, which is used to modify interactions and studying the strongly-interacting regime. In order to do this, we developed what we call the "many-body adiabatic" sequence. In this sequence, before applying the tilt, we ramp up a three-dimensional lattice to 20 E_R in all directions. The system is then in a Mott Insulator, where there is no phase coherence between the sites. In fact, in the deep lattice limit of $U \gg J, K$ the ground state wavefunction for the Harper-Hofstadter Hamltonian is the same as in the standard Bose-Hubbard Hamiltonian. Therefore, once we are in the deep Mott Insulator, we can apply the tilt and turn up the laser-assisted tunneling with the proper phase as quickly as we like without adding entropy. Then we ramp the lattice depths down to the final values for the

experiment before holding and imaging as usual. We call this sequence "many-body adiabatic" because it is adiabatic at all points except one, where it is protected by the many-body gap of the Mott Insulator.

We used both sequences in this work and found that the adiabatic sequence was less robust against technical noise, leading to a higher shot-to-shot variability. This is likely because of the higher specific heat of a system with gapless excitations in one direction. We do, however, find that the coherence lifetimes of the system after each turn-on procedure are comparable.

3.4 Results

For our first experiment, we use the non-adiabatic sequence to prepare the Harper superfluid and observe its momentum distribution in Figure 3-5h-j. The sharp peaks are the hallmark of a superfluid BEC in a lattice potential and demonstrate that we have prepared a low entropy state in the bulk Harper-Hofstadter Hamiltonian.

We first look at the pattern of peaks in Figure 3-5, which directly indicate the reduced symmetry of the Hamiltonian, despite the translational symmetry of the uniform magnetic field. The way to understand the pattern of peaks in the momentum distribution of a superfluid begins with the real-space symmetries of the Hamiltonian. In a square lattice with real tunneling in both directions, the Hamiltonian has the discrete symmetry vectors $a\hat{x}$ and $a\hat{y}$ and has a unit cell of size $a \times a$. In momentum space, the symmetry vectors map to $2\pi/a\ \hat{k}_x$ and $2\pi/a\ \hat{k}_y$, and the unit cell to a Brillouin zone of size $2\pi/a \times 2\pi/a$, as shown in Figure 3-5c and g. In our analysis of the Harper Hofstadter Hamltonian, Figure 3-5a, we must also take the tunneling phase into account, which leads to two new unit cells — gauge and magnetic. For our gauge, the new symmetry vectors are $2\pi/a\,(\hat{x} \pm \hat{y})$, and both the magnetic and gauge unit cells are twice the size of the bare lattice unit cell. The magnetic unit cell is gauge independent and is the smallest unit cell that contains an integer number of flux quanta [68]. For a magnetic flux $\alpha = p/q$, the magnetic unit cell is q times larger than the original unit cell and contains q indistinguishable sites [64]. The gauge unit

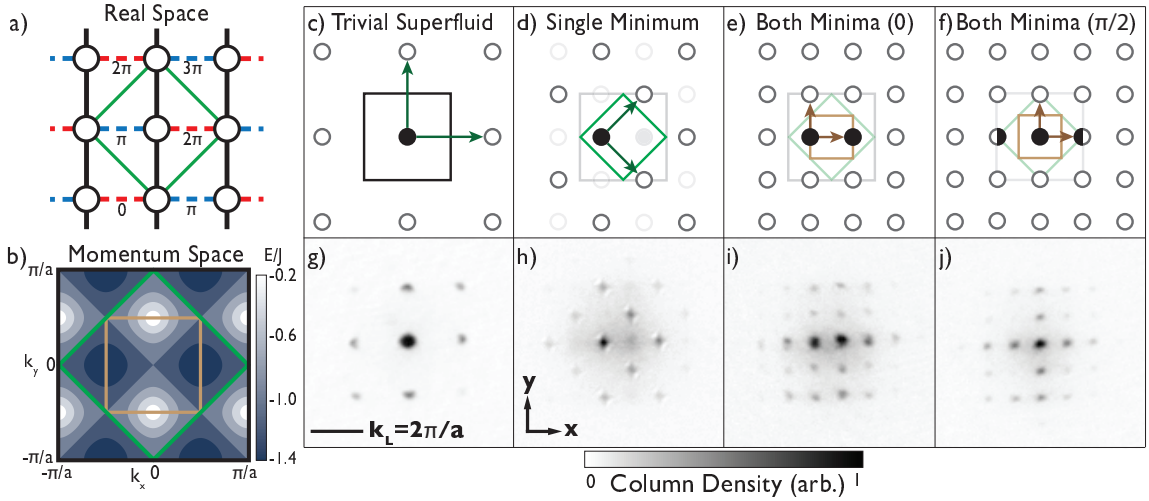

Figure 3-5: Observation of Bose-Einstein condensation in the Harper-Hofstadter model. (a) Spatial structure of the cubic lattice with the synthetic vector potential – (dashed) x-bonds feature a spatially dependent tunneling phase, whereas tunneling along (solid) y-links is the normal tunneling. The synthetic magnetic field generates a lattice unit cell that is twice as large as the bare cubic lattice (green diamond). (b) The band structure of the lowest band shows a twofold degeneracy of the ground state. The magnetic Brillouin zone (green diamond) has half the area of the original Brillouin zone. Due to the twofold degeneracy, the primitive cell of the band structure is even smaller (doubly reduced Brillouin zone, brown square). These lattice symmetries are both revealed in time-of-flight pictures showing the momentum distribution of the wavefunction. (c-f) Schematics of the momentum peaks of a superfluid. The dominant momentum peak (filled circle) is equal to the quasimomentum of the ground state. Due to the spatial periodicity of the wavefunction, additional momentum peaks (empty circles) appear, separated by reciprocal lattice vectors (green arrows) or vectors connecting degenerate states in the band structure (brown arrows). (g-j) Time-of-flight images. The superfluid ground state of the normal cubic lattice is shown in (g) in comparison to different repetitions of the same sequence for the superfluid ground state of the HH lattice (h-j). In (h), only one minimum of the band structure is filled, directly demonstrating the symmetry in our chosen gauge. The number of momentum components in (i-j) is doubled again due to population of both degenerate ground states. The micromotion of the Floquet Hamiltonian is illustrated in (e-f, i-j) as a periodically shifted pattern in the x-direction, analogous to a Bloch oscillation. All diffraction images have a field of view of 631 μm $\times$ 631 μm and were taken at a lattice depth of 11 E_r and 2.7 kHz Raman coupling with at least 30 ms hold in the HH lattice.

cell takes into account the specific gauge implemented in an experiment, and in highly symmetric gauges like ours can entirely overlap with the magnetic unit cell. There is a further symmetry caused by the indistinguishability of the q sites contained in each magnetic unit cell, which leads to a q-fold degeneracy of each state within the magnetic Brillouin zone, seen clearly in Figure 3-5b.

If the condensate occupies only one of the two degenerate momenta, we see a momentum distribution (Figure 3-5d and h), which clearly shows that the gauge symmetries are in the $2\pi/a\,(\hat{x} \pm \hat{y})$ directions. Figure 3-5e and i show the full symmetry of the bandstructure. Here, both energy minima are equally populated, and we can understand the image as the sum of Figure 3-5h with a second copy shifted by the gauge-invariant scale $2\pi/\,(qa)$ in either $\hat{x}$ or $\hat{y}$. The fourfold increase in visible peaks [69] should be thought of as a factor of two from the reduced symmetry of the lattice vectors and an additional factor of two from the degeneracy of the ground band. This is the first direct observation of the several symmetries of a square lattice in a uniform magnetic field.

Finally, in Figure 3-5e, f, i, and j, we comment on a subtlety of our method of simulation. In Section 3.2, we moved into a rotating frame for our analysis. However, we actually do our measurements in the stationary lab frame! Shifting from the rotating frame to the lab frame manifests itself as a kick in the x-direction that is dependent on the hold time, the initial phase of the stationary and Raman lattices [22], and the relative position of the harmonic confinement beams [70]. In our experiment, these wavelength scale drifts are not controlled from shot-to-shot, and we present two example shots with a phase of 0 and $\pi/2$.

3.4.1 Apparent Gauge Dependent Observables

In our above dicussion, we stated the time-of-flight images show the symmetries of the gauge, which seems to contradict the common wisdom that all observables are gauge-independent. There are two ways to square this with what we see in our systems with synthetic magnetic fields. First, we can view time-of-flight imaging, where we snap off all potentials, as preserving the form of the wavefunction at snap-off, but then

allowing it to evolve under the untrapped Hamiltonian $H = \vec{p}^2/2m$. This maps the gauge-dependent canonical momentum to mechanical momentum, which we observe [71, 62, 63].

A second, equivalent, description looks at this from the perspective of Maxwell's equations. When we perform time-of-flight measurements, we are turning off the vector potential $\vec{A}$ at the same time as all other fields. By Maxwell's equations, the changing vector potential creates an electric field $\vec{E} = -\partial\vec{A}/\partial t$, which leads to an impulse $\Delta\vec{p} = \int \vec{E} \cdot dt$. Thus, the mechanical momentum immediately after the field is turned off is given by a combination of the initial mechanical momentum and the starting vector potential in the natural gauge. This natural gauge is the one that has the same symmetry as whatever is physically creating the vector potential. In our case, this is the symmetry of the Raman lasers, while for a real magnetic field, it is the symmetry of the current used to create it. It is possible to analyze the system in a gauge with a different symmetry, but the gauge transformation will also add a term to the electric field pulse that cancels any physical effect of the gauge transformation. Thus, when we say that we have implemented a system with a specific gauge, we mean that our implementation has symmetries that make a given gauge the most natural for our analysis.

3.4.2 Population Imbalance

Nearly all iterations of the experiment result in roughly equal populations in both minima, and less than 1% of the shots show a single minima filled as in Figure 3-5h. To quantify this, we use a bandmapping technique before time-of-flight imaging. In bandmapping, we ramp down the lattice potentials slower than the timescale given by the bandgap, but faster than that given by the external harmonic confinemnt. This maps a quasimomentum q in lattice band n to a momentum state $2\pi n/a + q$ in a harmonic trap. We then rapidly snap off the harmonic confinement and perform time-of-flight imaging. This technique would be useful for us because it allows us to "collapse" all the peaks seen in Figure 3-5 into only one or two, depending on how many minima are filled.

However, there are two subtleties of our bandmapping procedure for an $\alpha = 1/2$ Harper superfluid that differ from the standard bandmapping. First, the two subbands are connected at Dirac points, and there is no bandgap! Bandmapping would fail at quasimomentum at or near the Dirac points, but since our atoms are condensed into the minima, they are sufficiently far from the Dirac points, and the gap we care about is the local gap. Note that this means that this bandmapping technique would not work for fermions or thermal atoms that fill a significant part of the lowest band. The second subtlety is that this rampdown is occuring in a real magnetic field gradient, which will cause potentially destructive Bloch oscillations. Thus, the whole procedure needs to be done on a time of the order of a Bloch oscillation time. We empirically found that first ramping down the Raman beams in 0.88 ms, then the lattice beams in 0.43 ms, and finally snapping off the harmonic confinement provides a good signal-to-noise.

Figure 3-6 shows the results of this bandmapping. As a control, we first applied the bandmapping sequence to a superfluid with only real tunneling created by amplitude modulation (labeled "AM" in the inset). As expected, we see only one quasi-momentum occupied. For a Harper superfluid, we nearly always see two peaks, one for each degenerate minima. We integrate the density in each peak and plot a histogram of the absolute population imbalance between the two for 30 shots, each taken at a 29.4 ms hold time.

We find that the population imbalance is sharply peaked around zero, demonstrating the degeneracy of the two minima. In some gauges, such as the Landau gauge, it is predicted that a superposition of the two single particle minima avoids density modulation and is therefore the ground state for a weakly interacting system [63, 64]. However, in our gauge, the quasimomentum eigenstates already have uniform occupation of the lattice sites, and so the weakly interacting ground state should be a single minimum. Therefore, we interpret the equal populations to be attributable to domain formation, likely as a result of technical fluctuations or non-adiabatic state preparation. Domain formation in a different Floquet system has been studied recently, and it was shown that single domains can be achieved with proper adiabatic

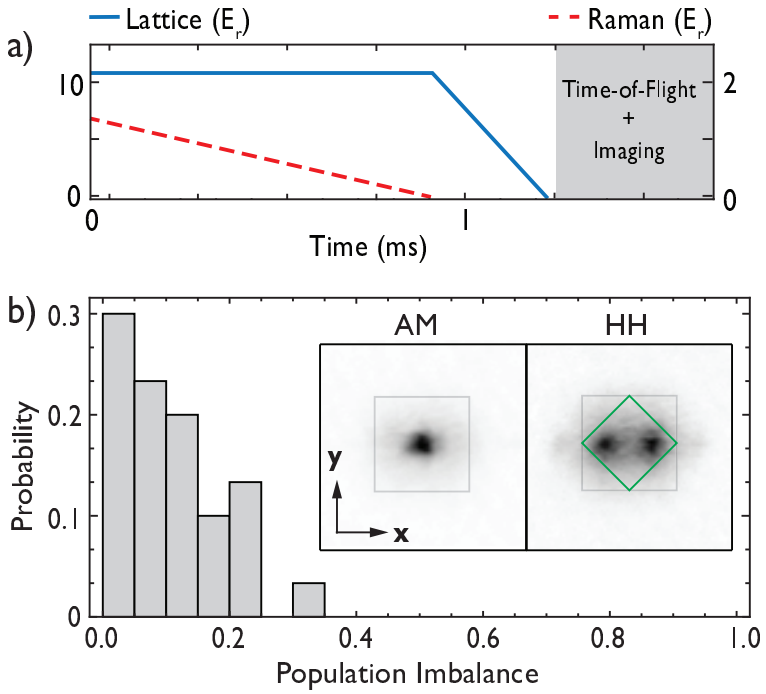

Figure 3-6: Population imbalance of the two ground states of the Harper-Hofstadter Hamiltonian with 1/2 flux. (a) Band mapping sequence adiabatically connecting quasimomentum to free space momentum. The Raman beams were ramped down from the initial strength of $1.4E_r$ to zero in 0.88 ms, followed by a linear ramp down of the lattice beams from $11E_r$ to zero in 0.43 ms. (b) The histogram shows the relative population imbalance of the two degenerate minima. Equal population in the two diffraction peaks is suggestive of domain formation due to spontaneous symmetry breaking but can also be driven by lattice noise and technical fluctuations. The data consists of 30 shots taken after a hold time of 29.4 ms in the HH lattice. The inset displays a raw image for the band mapping of the 1/2 flux superfluid with two degenerate ground states compared to a topologically trivial superfluid with one ground state (see text). The Brillouin zones of the cubic lattice (grey) and the gauge (green) are overlaid for clarity.

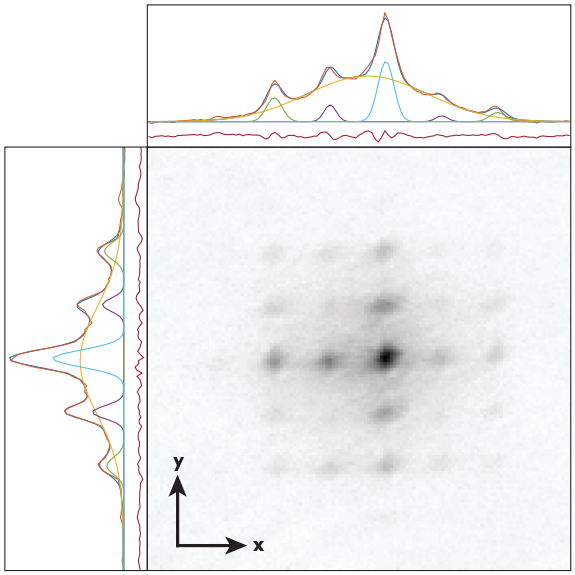

Figure 3-7: An example fit for a 1/2 flux superfluid image after a hold time of 34 ms. The thermal fraction fit is shown in yellow with the components of the superfluid diffraction fit in cyan, purple, and green. Their sum is shown in dark blue laid over the raw data in orange. The residuals are shown in dark red. A visibility of $V = 0.40$ is derived from the amplitudes of this fit.

state preparation [72].

3.4.3 Superfluid Peak Fitting

In order to move forward with our experiments, we want a measure of the coherence of the system, which we quantify using peak visibility. All of our absorption images are the sum of the superfluid peak pattern with 25 peaks and a broad incoherent background, which we associate with the thermal portion of the system. In analogy with Michelson's definition of optical fringe contrast, we define the visibility of a given superfluid peak as its amplitude divided by twice the thermal background at its center.

The full two-dimensional image has too many degrees of freedom to fit reliably, so our fitter works by fitting to two one-dimensional line cuts, one in each lattice direction. We make these line cuts by first finding the center of mass and then averaging several rows or columns of pixels around this. We then fit the x and y line cuts to the sum of six Gaussian peaks, which correspond to the one thermal and five

superfluid peaks mentioned above. We report the average visibility of the peaks in both directions.

Even restricting ourselves to one lineout requires us to fit a high-dimensional parameter space — we need to find the center of the thermal background, its width and amplitude, the phase of the micromotion, the distance between superfluid peaks, the width of the superfluid peaks, and each peak's amplitude. We can constrain the fit so that the superfluid peak differences are equal and that they all have the same width, but this still leaves 11 fitting parameters. Therefore, our nonlinear least squares fit requires good initial guesses. Find our initial guesses for the thermal bakground first by fitting a single Gaussian to the image with frequencies of order the normal superfluid peak spacing and higher filtered out. Next, we subtract this fit from the raw data and pick the highest five remaining peaks, whose position and amplitude become the initial guess for the superfluid peaks in the final fit. Finally, we fit the full model using the initial conditions collected from the pre-processing. An example of a typical fit is shown in Figure 3-7.

3.4.4 Adding Strong Interactions

Now that the single-particle physics of the Harper-Hofstadter Hamiltonian has been verified, we wish to study the strongly interacting limit, near the Mott Insulator transtion. This transition for $\alpha = 1/2$ and a filling factor of five occurs at $J/U \sim 0.016$ [73]. For an isotropic HH lattice, the transition happens around 15-16 E_r, with the precise value depending on multiple lattice parameters such as anisotropy, Raman drive strength, and tilt strength. For lower filling factors, the critical $J/U \sim 0.059$, and the transition occurs around 12 E_r, so our experiments with a three-dimensional lattice can be in the strongly interacting regime.

We use the many-body adiabatic sequence, with a lattice in the third dimension, to reach this regime. We keep the final lattice depths (and therefore tunneling strenghts) along the x- and y-directions constant, while varying the z lattice depth, which can give us a Hubbard U parameter from nearly zero to ∼450 Hz, which with the filling factor of five mentioned above, brings us near the Mott Insulator transition.

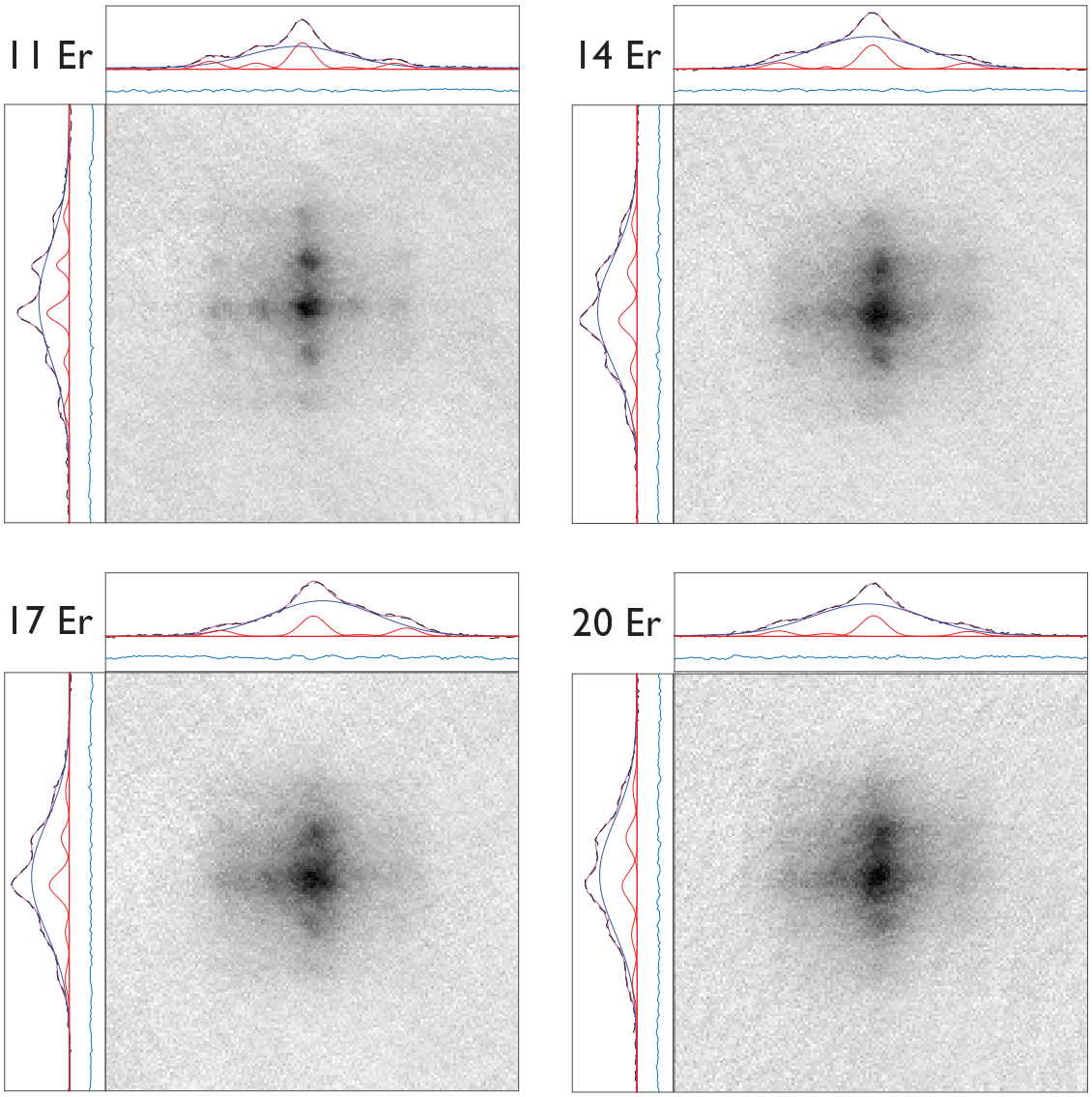

Figure 3-8: Harper-Hofstadter Hamiltonian with strong interactions. Here we present a selection of shots with the x-and y-lattices fixed at 11 E_r and a variable z lattice of 11, 14, 17, and 20 E_r.

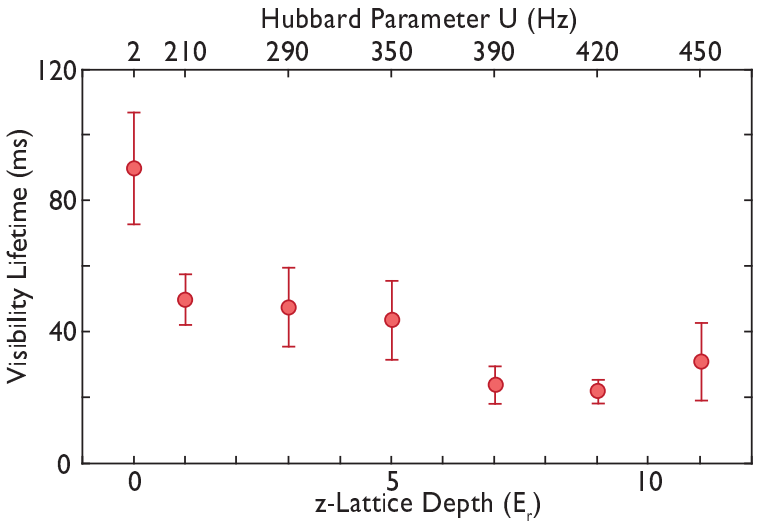

Figure 3-9: Strongly interacting Harper superfluid lifetime. Shown is the lifetime of the visibility of the diffraction pattern versus z-lattice depth. The top axis shows the Hubbard interaction parameter U. All lifetimes are measured from the end of the 35 ms ramp exiting the Mott insulator. Uncertainty is given by the statistical error of the mean of five repetitions of the experiment, added in quadrature to uncertainty in the peak visibility fitting.

In Figure 3-8, we present representative shots of a BEC in the Harper-Hofstadter Hamiltonian with strong interactions. We see visible, if weak, superfluid peaks for z-lattice depths up to 20 E_r, while the other two lattices are held at 11 E_r. Above a z-lattice of 11 E_r, we found significant shot-to-shot variation, likely due to technical fluctuations, so in Figure 3-9, we measured the visibility lifetime of strongly interacting Harper superfluids with interaction parameters up to $U = 450$ Hz. We find that the lifetime is reduced in the strongly-interacting system in compariston to the non-interacting system, but only by a factor of $\sim 2 - 4$.

3.5 Lifetime of the Harper Superfluid

There are many open questions about topological physics in the presence of strong interactions, which often involve small energy scales and therefore require longer coherence lifetimes than we have achieved. Since our system is relatively complex, there are several categories of heating that can limit our lifetimes. First, there is what we call "generic technical heating," which encompasses the sorts of heating which are

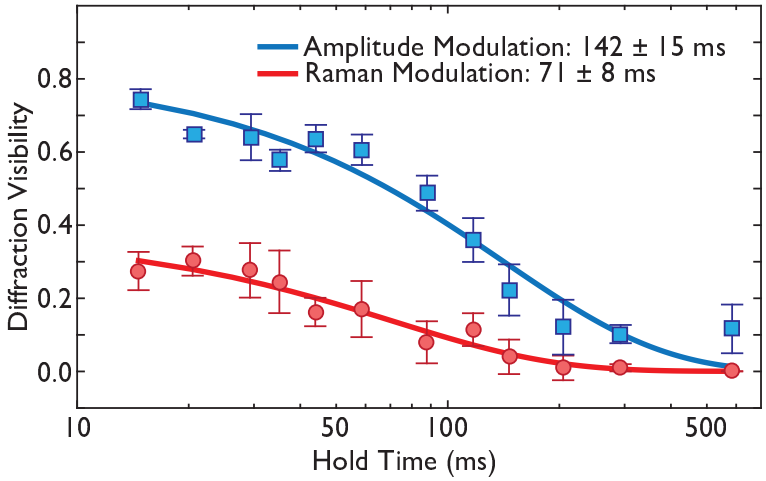

Figure 3-10: Decay of Bose-Einstein condensates in modulated lattices. The figure compares the decay of the 1/2 flux Harper superfluid (red circles) to the decay of the amplitude-modulated superfluid (blue squares). Note that the lower visibility of the Harper superfluid is due to the peak doubling, which at the same condensate fraction, leads to lower visibility. Exponential fits to the decay of the visibility of the diffraction patterns give lifetimes of 142 ± 15 ms and 71 ± 8 ms, respectively. Data were taken with 11 E_r cubic lattice with either 2.7 kHz Raman coupling or 20% amplitude modulation and start after a 10 ms hold time after switching on the final Hamiltonian using the non-adiabatic procedure. Uncertainty is given by the statistical error of the mean of five repetitions of the experiment, added in quadrature to uncertainty in the peak visibility fitting.

common to all lattice systems, e.g., lattice and amplitude modulation, beam pointing drifts, and magnetic field fluctuations. The second category is "Floquet heating," which include all heating processes that occur in periodically driven Floquet systems as ours is. The final category is heating specific to the Harper-Hofstadter Hamiltonian, which is still an open field.

In order to disentagle these different sorts of heating, we compared our non-interacting Harper superfluid to a normal superfluid created using amplitude modulation [66, 67]. This system is also a Floquet system, and should have many heating sources in common with the Harper superfluid. In Figure 3-10, we show the lifetime of the superfluid peak visibility for both the Harper superfluid and the amplitude-modulated superfluid. At first, the Harper superfluid's lifetime was notably shorter than that of the amplitude-modulated superfluid, but the experimental upgrades discussed in Section 3.3.1 improved the Harper superfluid lifetime until it was comparable

to the amplitude-modulated lifetime.

By looking at atom number loss, we can rule out several possible sources of noise. We observed no discernable number loss out to 500 ms, which immediately tells us that neither two-body dipolar collisions nor three-body recombination are the limiting source of heating. Because the tilt Δ is so strong, higher Bloch bands are coupled to the continuum and would rapidly be lost from our system, so the lack of atom loss during experimental timescales makes it clear that the majority of the heating is intra-band.

3.5.1 Floquet Fermi's Golden Rule

We next look to a Floquet heating explanation for intra-band heating. The lowest order decay path in a Floquet system is via overlap of neighboring Wannier-Stark states with offset energy Δ, which is transferred to excitations of the lowest bands, or to the free particle motion along the tubes orthogonal to the two-dimensional lattice. We can analyze this by using Fermi's golden rule for Floquet systems [74, 75]. We follow and extend [75], which calculates the heating rate for a one-dimensional amplitude-modulated lattice. Here, the ground state of the corresponding Floquet Hamiltonian is a superfluid in a lattice in one dimension and free motion in the other two.

There are two main processes that contribute to the decay of the condensate. Wannier-Stark states – which are mostly localized in a given well n – have small components in lower wells $n-1$, with amplitude $\propto 2J/\Delta$. This small component, which has energy Δ higher than the Wannier-Stark state localized in the well $n-1$, can collide with atoms in the lower lattice site, thus creating two excitations with energy $\Delta/2$ in the transverse direction (the creation of two exitations is necessary for conservation of transverse momentum) . The second mechanism involves the counter-rotating term of the phonon or photon assisted tunneling process. The co-rotating term enables resonant tunneling to a lower lattice site by stimulated emission of a phonon. In the counter-rotating process, the atoms tunnels to a lower lattice site, but absorbs a lattice phonon. Therefore, it has now an excess energy of 2Δ which

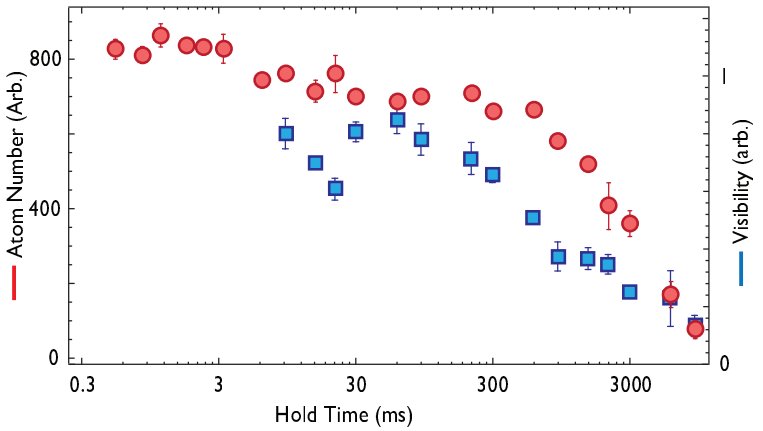

Figure 3-11: Lifetime of a Bose-Einstein condensate in a 1D lattice with resonant amplitude modulation. Shown are the decay of the number of trapped atoms, and the decay of the visibility of the diffraction pattern observed after ballistic expansion.

can create two transverse excitations where each of them has energy Δ.

These two-body elastic collisions convert modulation or tilt energy into motion along the transverse directions. The characteristic relaxation times of the two processes are given by τ_1 and τ_2:

$$\frac{1}{\tau_1} \propto \frac{4J^2}{\Delta^2} \sum_k 2\pi\delta(E_k^{(0)} - \Delta/2)$$

$$\frac{1}{\tau_2} \propto \frac{K^2}{\Delta^2} \sum_k 2\pi\delta(E_k^{(0)} - \Delta).$$

We can associate τ_1 with a process that occurs even in the absence of modulation – the rate is proportional to the tunnel coupling squared between neighboring sites, whereas the rate of the τ_2 process is proportional to the square of the phonon induced tunneling rate. Both decay processes are rather general and should apply to both tilted lattices and lattices modulated by superlattices.

As a test of these predictions, we implemented this Hamiltonian experimentally using the same experimental procedure as used for a two-dimensional amplitude-modulated superfluid. We measured the coherence and lower band population lifetimes as shown in Figure 3-11. Approximate values in our experiment were $gn = h \times 550 - 830$ Hz, $a_s = 5.03$ nm, $d = 254$ nm, $K = h \times 10$ Hz, $J = h \times 30$ Hz, and $\Delta =$

$h \times 3420$ Hz, with gn as the chemical potential, a_s the s-wave scattering length, K laser-assisted tunneling rate, J the bare tunneling rate, and Δ the energy tilt per lattice site. $d^{-1} = \int \mathrm{d}x\ \phi_x(x)^4$ is the size of the Wannier state in the x-direction $\phi_x(x)$. These give us the values of $1/\tau_2 = 0.003 - 0.005\ \mathrm{s}^{-1}$ and $1/\tau_1 = 0.13 - 0.20\ \mathrm{s}^{-1}$, which are longer than our observed lifetime. Uncertainty is driven by uncertainty in our density measurements due to redistribution during lattice ramp-up. However, during the long coherence lifetime, significant population loss was observed (due to inelatic two- or three-body collisions, or transfer to higher bands), and detailed further study is needed to identify the contributions of different processes to the decay rate.

The mechanism proposed in [75] appears to give a reasonable upper limit for collisional decay in 1D lattices. We expect the same mechanism to explain at least part of the decoherence observed for both amplitude modulation in a two-dimensional lattice and the HH Hamiltonian. For a quantitative comparison, we modify the calculation in [75] to reflect that a 2D lattice has only one orthogonal direction of free motion, which changes the density of states for decay processes. For resonant modulation, in the Floquet basis, the Hamiltonian is

$$H = \sum_k \epsilon_{\mathbf{k}}(t) b^\dagger_{\mathbf{k}} b_{\mathbf{k}} + \frac{g}{2V} \sum_{\mathbf{k_1},\mathbf{k_2},\mathbf{k_3}} b^\dagger_{\mathbf{k_1}} b^\dagger_{\mathbf{k_2}} b_{\mathbf{k_3}} b_{\mathbf{k_4}}$$

with $\mathbf{k_4} = \mathbf{k_1} + \mathbf{k_2} - \mathbf{k_3}$, V as the system volume, and $b_{\mathbf{k}}$ and $b^\dagger_{\mathbf{k}}$ as the annihiliation and creation operators for states with quasimomentum $\mathbf{k}$. The interaction parameter is given by

$$g = \frac{4\pi\hbar^2 a_s}{m} \lambda^2 \int \mathrm{d}x\ \mathrm{d}y \phi_x(x)^4 \phi_y(y)^4 = \frac{4\pi\hbar^2 a_s}{m} \frac{\lambda^2}{d^2}$$

where $\phi_x(x)$ and $\phi_y(y)$ are the Wannier functions in the tilted (x) and untilted (y) lattice directions, λ is the lattice spacing, and d is the size of the Wannier state. The instantaneous single particle dispersion $\epsilon_{\mathbf{k}}(t)$ is given by

$$\epsilon_k(t) = -2K\cos(k_x) - 2J_y\cos(k_y) - 2K\cos(k_x - 2\Delta t) - 2J_x\cos(k_x - \Delta t) + \frac{\hbar^2 k_z^2}{2m}.$$

where J_x and J_y are the bare tunneling rates in the x and y directions, and K

is the effective tunneling in the tilt direction (x). We ignore the overall harmonic confinement and treat motion along z as free. Following a similar argument, we find that the scattering rate is given by

$$\frac{1}{\tau} = \frac{1}{\tau_2} + \frac{1}{\tau_1}$$

$$\frac{1}{\tau_2} = \frac{2(gn/2)^2}{N\hbar}\frac{K^2}{\Delta^2}\sum_k 2\pi\delta(E_k^{(0)} - \Delta)$$

$$\frac{1}{\tau_1} = \frac{2(gn/2)^2}{N\hbar}\frac{4J^2}{\Delta^2}\sum_k 2\pi\delta(E_k^{(0)} - \Delta/2)$$

with the effective dispersion:

$$E_k^{(0)} = 2K[1-\cos(k_x)] + 2J_y[1-\cos(k_y)] + \sqrt{\frac{gn}{m}(\hbar k_z)^2 + \left(\frac{(\hbar k_z)^2}{2m}\right)^2}.$$

Note that ref. [75] uses a Hartree-Fock excitation energy with free particle dispersion. The high mean field energy in the one dimensional tubes created by a two dimensional lattice, gn, is similar in energy scale to the tilt frequency, and we thus use the full Bogoliubov spectrum for the energy of quasi-particles.

Since K and J_y are small, we neglect the dependence of $E_k^{(0)}$ on k_x and k_y, giving

$$\rho(\nu) = \sum_k 2\pi\delta(E_k^{(0)} - \nu) \tag{3.18}$$

$$= \frac{V}{\lambda^2}\int \frac{\mathrm{d}k_z}{2\pi} 2\pi\delta\left(\sqrt{\frac{gn}{m}(\hbar k_z)^2 + \left(\frac{(\hbar k_z)^2}{2m}\right)^2} - \nu\right) \tag{3.19}$$

$$= \frac{Vm}{\hbar^2\lambda^2}\frac{\nu}{\sqrt{(gn)^2+\nu^2}}\frac{\sqrt{\frac{2\hbar^2}{m}}}{\sqrt{-(gn)+\sqrt{(gn)^2+\nu^2}}} \tag{3.20}$$

and thus

$$\frac{1}{\tau_2} = \frac{gn}{\hbar}\frac{4\pi a_s}{d}\frac{K^2}{\Delta^2}\frac{\Delta}{\sqrt{(gn)^2+\Delta^2}}\frac{\sqrt{\frac{\hbar^2}{2md^2}}}{\sqrt{-(gn)+\sqrt{(gn)^2+\Delta^2}}}$$

$$\frac{1}{\tau_1} = \frac{gn}{\hbar}\frac{4\pi a_s}{d}\frac{4J^2}{\Delta^2}\frac{\Delta/2}{\sqrt{(gn)^2+(\Delta/2)^2}}\frac{\sqrt{\frac{\hbar^2}{2md^2}}}{\sqrt{-(gn)+\sqrt{(gn)^2+(\Delta/2)^2}}}$$

For our system, representative numbers are $gn = h \times 740 - 1740$ Hz, and $\Delta = h \times 3420$ Hz, $K = h \times 10$ Hz, $J = h \times 30$ Hz, $a_s = 5.03$ nm, $d = 254$ nm, and $m = 1.4 \times 10^{-25}$ kg, resulting in $1/\tau_2 = 0.006 - 0.014$ s^{-1} and $1/\tau_1 = 0.29 - 0.67$ s^{-1}. This is less than the decay rates measured in the experiment by a factor of $\sim 10 - 20$.

A three-dimensional lattice should be helpful for reducing heating described by the Floquet Fermi's golden rule. If a three-dimensional lattice has a bandbap at energies Δ and $\Delta/2$, we expect to see a "gapping out" of this heating and a strong increase in the lifetime [76]. However, in our experiment, we do not see this strong change when changing the bandgap. We therefore believe that the heating we see is either technical heating common to both amplitude-modulated and Harper superfluids, or some as-yet-unexplained heating process for Floquet systems.

3.6 Conclusion

In conclusion, for the first time, we have demonstrated Bose-Einstein condensation in a strong synthetic magnetic field. The momentum distribution of the ground state clearly shows how the vector potential and gauge break the translation symmetry of the bare lattice and uniform magnetic field. We have added strong interactions to our system and have demonstrated reasonable coherence times near the Mott Insulating transition. With longer lifetimes, modifications of our system could lead to the realization of Weyl points [77], the quantum spin Hall Hamiltonian and ultracold atom topological insulators [78], and bosonic Laughlin states [73, 79, 38, 80]. A full understanding of Floquet heating is still an open area of research in the field [81, 82], while it is possible that a tripled-superlattice system could avoid some of the heating processes in this work [78].

Chapter 4

Superfluid Shielding

A central feature of quantum mechanics is the wave-particle duality, where matter that we normally think of as composed of particles can be described by a wavefunction $\psi(x)$. Since the probability of finding a particle is given by $|\psi(x)|^2$, it is tempting to think of the wavefunction as merely a probability distribution. However, we must note that the probability distribution is the squared modulus of the wavefunction, and that $\psi(x)$ has an additional degree of freedom in its complex phase $\psi(x) = \exp[i\phi(x)]\,|\psi(x)|$. This quantum phase is directly relevant for many applications in in quantum information, quantum simulation [83, 84, 65], atom interferometry [25], and force sensing [29, 30, 31].

Important applications rely on maintaining phase coherence between spatially separated quantum subsytems. However, our ability to split a quantum system, perform an operation on the separated subsystems, and use interference to read out phase information is limited. For now, I will ignore technical or environmental limitations and focus on the fundamental limits. In a non-interacting system of size N, classical shot noise leads to fluctuations of $\sim 1/\sqrt{N}$ in the number of particles in each subsystem, which determine the final signal-to-noise ratio and precision of the measurement of the phase, but do not affect the coherence lifetime.

In an interacting system, on the other hand, the coherence time is also set by shot noise. The phase of each subsystem evolves at a rate given by the total energy $E_{\text{total}} = E_{\text{external}} + \mu$, where μ is the chemical potential. The shot noise fluctuations mentioned

above give rise to fluctuations of the chemical potential $\delta\mu = \delta N \times |\partial\mu/\partial N|$, leading to decoherence. Previous work has focused on either one of the two terms in the formula for $\delta\mu$. In [85], the researchers use Feshbach resonances to modify interatomic interactions and therefore $|\partial\mu/\partial N|$, which lead to very long coherence times. Other work has modified δN by using non-classical squeezed states, which can be created using nonlinear interactions [86, 87] or quantum measurements [88]. While most work on squeezing has been done with relatively small numbers of atoms, highly spin-squeezed states have been observed for pairs [89] and arrays [90] of independent Bose-Einstein condensates.

In this chapter, I present a new method for increasing the phase coherenc time of separated BECs beyond the projection noise limit. If we immerse the separated BECs in a common superfluid bath, we find that the interactions between the bath and the system can compensate for technical and number fluctuations that normally shorten the phase coherence time. I begin with a review of atom interferometry, which provides an intuitive way to think about the effects of phase coherence and separated quantum objects. I then discuss the phenomenon of Bloch oscillations, where a BEC in a tilted lattice precesses through the Brillouin zone, and demonstrate how this effect can be thought of as a form of atom interferometry. I provide a more quantitative explanation of superfluid shielding, and report on several experiments that explore the effect in various parameter regimes that demonstrate that superfluid shielding is a robust effect that can in principle reduce chemical potential fluctuations in atom interferometers by two orders of magnitude.

This chapter covers work covered in [91].

4.1 Atom Interferometry

The importance of phase coherence is most obvious in the technique of atom interferometry. This technique exemplifies the wave nature of ultracold atoms by making an analogy with optical interferometry. I will first review classical optical interferometry and then point to the analogs of each piece in atom interferometry.

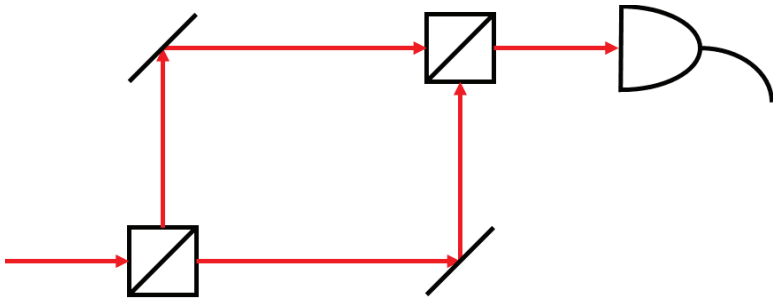

Figure 4-1: A basic optical interferometer. A coherent light source (red arrows) is split by a 50:50 beamsplitter and travels along two different paths. The two paths are recombined on a second beamsplitter and interfere. The path length difference between the two arms becomes a phase difference and determines the photodiode reading.

The simplest form of an optical interferometer (cartoon in Figure 4-1) starts with a single coherent light source (i.e. a laser), which is split on a 50:50 beamsplitter. The light travels in two arms, of length l_1 and l_2, and then is re-combined at the second beamsplitter. The two arms will interfere with a phase given by $2\pi\left(l_1 - l_2\right)/\lambda$, where λ is the wavelength of the light, and we can thus use a photodiode or camera to read out the difference in path-length. The conceptually simplest atom interferometers map exactly to this optical interferometer. Instead of a laser, start with a BEC, which is a coherent state and therefore has a well-defined phase. The beam splitter can be implemented with Raman pulses, which provide a momentum kick that separates the clouds, or optical lattices, which can remove tunneling between different sites, effectively separating the condensates. The phases of each now-separated condensate evolve at a rate given by $-E_{(1,2)}/\hbar$, where $E_{(1,2)}$ are the energies of the two condensates. The condensates are re-combined and interfered by physically overlapping the two condensates. If they were split using a Raman pulse, subsequent Raman pulses can reverse the momentum and push the clouds back together. On the other hand, if a lattice was used to separate the condensates, we use time-of-flight imaging, where we snap off all trapping potentials. Then the condensate on each lattice site acts as an emitter of a spherical matter wave with a phase given by the phase of the wavefunction on that site. Once they have expanded to several times the initial system size, the interference pattern can be used to read out the phase information

from the interferometer.

An important difference between an atom interferometer and its optical counterpart is the role of interactions. As discussed above, inter-particle interactions (which are not present for an optical interferometer) can limit the coherence lifetime and decrease the contrast of the interferometer. Thus, most atom interferometers use atoms just above the BEC transition point, where interactions are negligible, and are therefore more similar to a white-light interferometer. Superfluid shielding on the other hand allows us to use a high-brightness coherent source without being limited by interaction effects, and should lead to better overall contrast and coherence times in atom interferometers.

4.2 Bloch Oscillations

In our experiments, we used the coherence of Bloch oscillations as our measure of coherence of the separated condensates. Since Bloch oscillations are not normally described as an atom interferometry effect, it makes sense to take some time to discuss the effect now. We should emphasize that the following discussion and our experiments are in the high-tilt regime, in contrast to most previous work on Bloch oscillations, which have focused on the low-tilt regime [92, 93, 94] where adjacent Wannier-Stark states overlap and tunneling is still allowed.

As discussed in Section 2.1, the single-particle eigenstates in a one-dimensional lattice potential are described by Bloch wavefunctions $|\psi_k\rangle$ with quasimomentum k and energy $E_k = -4J\cos(ka)$. The traditional explanation of Bloch oscillations is that if we apply a constant energy tilt per lattice site of Δ, we can write this as a

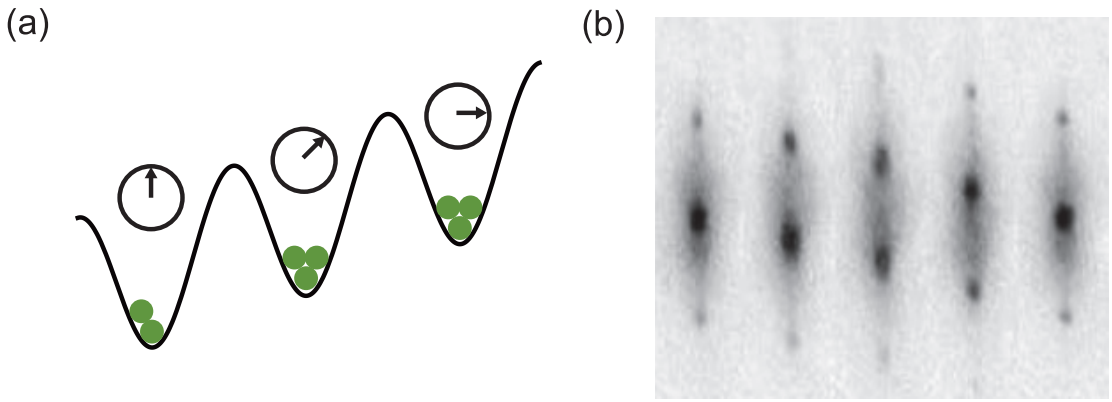

Figure 4-2: (a) Cartoon of Bloch oscillations as an atom interferometry effect. Bloch oscillations occur when a BEC is placed into a tilted optical lattice. After the tilt, each lattice site has a separated condensate whose phase is represented by the clocks. Each phase evolves at a different rate, given by the on-site energy, which leads to different interference patterns after different evolution times. (b) Interference patterns of ^{87}Rb atoms in a lattice the course of a Bloch cycle at times 0, $\pi/2$, π, $3\pi/2$, 2π.

force $F = -\Delta/a$, and quasi-classical dynamics then tells us

$$\begin{aligned} \hbar\frac{dk}{dt} &= F \\ v &= \frac{1}{\hbar}\frac{dE}{dk} \\ &= \frac{4Ja}{\hbar}\sin(ka) \\ &= \frac{4Ja}{\hbar}\sin\left(\frac{Fat}{\hbar}\right) \end{aligned} \tag{4.1}$$

which shows that a constant force begets oscillations whose frequency provide a measure of the applied force. However, this traditional explanation does not make obvious the connection to atom interferometry and the importance of phase coherence.

To do this, first note that in the tight-binding limit, we can write $|\psi_k\rangle$ as the sum of Wannier states centered on site j, with $|\psi_k\rangle = \sum_j \exp[ikaj]\, a_j^\dagger |0\rangle$ where $a_j^\dagger$ is the Wannier state creation operator. To see Bloch oscillations, we start in with an untilted lattice, so the atoms are in some $|\psi_k\rangle$. This is the equivalent to the initial single BEC in traditional atom interferometry. We then rapidly turn on a constant

tilt Δ. The Hamiltonian is simply given by

$$H = -J \sum_j a_{j+1}^\dagger a_j + \Delta \sum_j j a_j^\dagger a_j. \tag{4.2}$$

Since we assume the high-tilt regime of $\Delta \gg 4J$, the lattice sites are decoupled, which is equivalent to physically separating the two sub-condensates. The state evolves to

$$|\psi(t)\rangle = \sum_j \exp\left[ij\left(ka - \Delta/\hbar\right)\right] a_j^\dagger |0\rangle = \left|\psi_{k+F/\hbar}\right\rangle. \tag{4.3}$$

We can picture this, as in Figure 4-2 as each lattice site having a clock attached to it, that runs at the phase evolution rate. When all the clocks have evolved by a multiple of 2π, we are back at the starting point, leading to oscilliatory motion. Finally, to see this effect, we can interfere parts of the wavefunction from different lattice sites by performing time-of-flight imaging, as discussed above.

4.3 Superfluid Shielding

If we are using an interacting system for the atom interferometer, number fluctuations in the separated condensates lead to chemical potential fluctuations. These chemical potential fluctuations change the phase evolution of the systems, leading to dephasing and a shortened coherence time. Rather than attempting to reduce the number fluctuations using sqeezed states, or reduce the interactions via a Feshbach resonance, we present a new technique. In superfluid shielding, the separated condensates are immersed in a superfluid bath. The interactions between the bath and the interferometer cancel out the effect of projection noise on the phase evolution and increase the coherence time.

Fig. 4-3a-c provides a graphical view of superfluid shielding in our experiment. After the sudden tilting of the $|\downarrow\rangle$ atoms, each lattice site is a separate condensate, with no resonant tunneling from site to site. Then, if there is no shielding component, the evolution of the phase on each site is given only by the local chemical potential

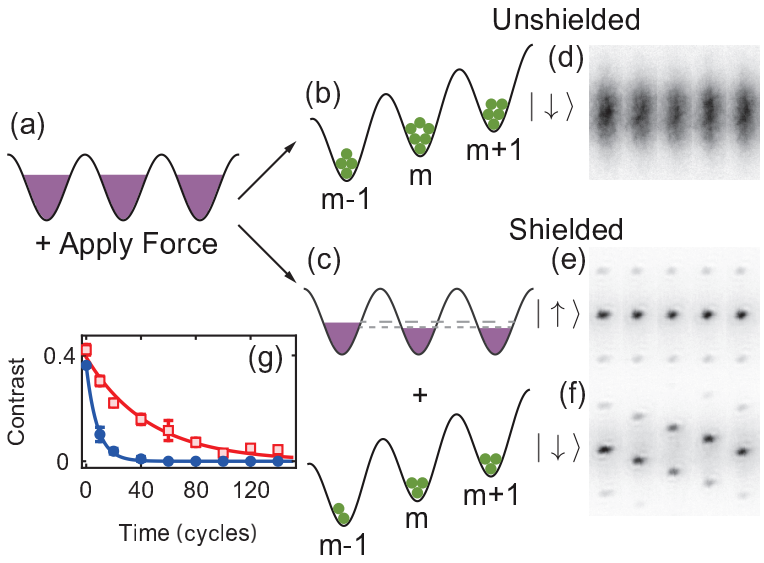

Figure 4-3: Schematic of superfluid shielding. (a) Before applying a tilt, the atoms are in a superfluid, which is approximately described by a coherent state on each site. The chemical potential is constant across the cloud. (b) In the limit of a strong tilt ($\Delta \gg J$), the wavefunction at each lattice site is projected onto the number basis, leading to fluctuations in the number of atoms and chemical potential from site to site. (c) If the gas has two components, one which is localized by the tilt, and one which remains superfluid, the itinerant component can compensate for fluctuations in the localized component. (d-f) Momentum distribution over the course of a single Bloch oscillation after ten cycles. (d) Without superfluid shielding, the diffuse cloud indicates decoherence of the condensate. (e) The itinerant component feels no force and does not Bloch oscillate. (f) For the shielded component, the Bloch oscillation contrast is high. (g) Exponential decay of the Bloch oscillation contrast for a one-component (blue dots) and two component (red squares) gas, for a transverse lattice depth of 11 E_r and $\sim 8 \times 10^3$ atoms.

and its fluctuations, $\mu_j^{\downarrow}$, and has a relatively short coherence time. On the other hand, when the system is immersed in a superfluid of $|\uparrow\rangle$ atoms, which are not subject to the tilt, we see superfluid shielding. The $|\downarrow\rangle$ atoms and the $|\uparrow\rangle$ atoms on a given site interact repulsively. However, because $|\uparrow\rangle$ atoms remain superfluid, these atoms can freely adjust their local density in order to counteract the fluctuations in $|\downarrow\rangle$ atoms and thus maintain a uniform global chemical potential. This leads to an anti-correlation in the densities of the two components, which mitigates the fluctuations in the chemical potential of the $|\downarrow\rangle$ component. Previous work in the low-tilt regime has shown that the presence of disorder applied before the tilt leads to a shortened coherence time of Bloch oscillations, and that this can be partially compensated for by weak interactions [95, 96]. This work demonstrates a different regime, where a separate superfluid bath can compensate for disorder created during and after the tilt, including projection noise disorder.

We use two more quantitative descriptions of the effect of superfluid shielding: one is based on the Gross-Pitaevskii equation and provides a useful intuitive picture, while the other treats the effect fully quantum mechanically.

4.3.1 Gross-Pitaevskii Description

In the Thomas-Fermi approximation, the Gross-Pitaevskii equation for a two component gas in a lattice is given by the following:

$$\mu_j^{\downarrow} = g^{\downarrow\downarrow} n_j^{\downarrow}(x,y) + V_{\mathrm{ext},j}^{\downarrow}(x,y) + g^{\uparrow\downarrow} n_j^{\uparrow}(x,y) \tag{4.4}$$

$$\mu_j^{\uparrow} = g^{\uparrow\uparrow} n_j^{\uparrow}(x,y) + V_{\mathrm{ext},j}^{\uparrow}(x,y) + g^{\uparrow\downarrow} n_j^{\downarrow}(x,y), \tag{4.5}$$

where $\mu_j^{(\uparrow,\downarrow)}$ and $n_j^{(\uparrow,\downarrow)}$ are the chemical potential and number density, for a given component and lattice site index j. The interaction terms $g^{\uparrow\uparrow,\downarrow\downarrow,\uparrow\downarrow}$ are the standard contact interactions $4\pi\hbar^2 a^{(\uparrow\uparrow,\downarrow\downarrow,\uparrow\downarrow)}/m$ with $a^{(\uparrow\uparrow,\downarrow\downarrow,\uparrow\downarrow)}$ as the s-wave scattering lengths for intra- and inter-component collisions. In our experiment, before the tilt is applied, both spin components are superfluid, and are subject to a common trapping potential $V_{\mathrm{ext},j}^{(\uparrow,\downarrow)} = V_{\mathrm{trap},j}$. Then the initial densities are such that the chemical potentials $\mu_j^{(\uparrow,\downarrow)}$

are constant, and the trapping potential is fully compensated by an inhomogeneous Thomas-Fermi density profile [97].

After our experiment is initialized, we apply an additional potential with a spin-independent part δV_j, and a spin-dependent force $-j\Delta$, which is only felt by $|\downarrow\rangle$ atoms. The spin-dependent force separates the condensates of $|\downarrow\rangle$ atoms, which feel an energy shift of Δ per lattice site, while leaving $|\uparrow\rangle$ atoms, which feel no shift, in a superfluid state with a constant chemical potential. We label the frozen-in number fluctuations $\delta n_j^{\downarrow}$ and the $|\uparrow\rangle$ chemical potential $\mu_j^{\uparrow} = \mu^{\uparrow}\ \forall\ j$. The constraint on $\mu_j^{\uparrow}$ allows us to determine the induced density fluctuations in $|\uparrow\rangle$:

$$\delta n_j^{\uparrow} = -\frac{\delta V_j}{g^{\uparrow\uparrow}} - \frac{g^{\uparrow\downarrow}}{g^{\uparrow\uparrow}}\delta n_j^{\downarrow}. \tag{4.6}$$

If we plug this into Equation 4.4, we find that the $|\downarrow\rangle$ chemical potential after the applied tilt is

$$\begin{aligned}\mu_j^{\downarrow} &= g^{\downarrow\downarrow}\left(n_j^{\downarrow} + \delta n_j^{\downarrow}\right) + V_{\mathrm{ext},j}^{\downarrow} + g^{\uparrow\downarrow}\left(n_j^{\uparrow} + \delta n_j^{\uparrow}\right) \\ &= \mu^{\downarrow,0} - j\Delta + \delta\mu_j^{\downarrow}\end{aligned} \tag{4.7}$$

where $\mu^{\downarrow,0}$ is defined as the constant chemical potential of $|\downarrow\rangle$ before the tilt is applied. Here $\delta\mu_j^{\downarrow}$ are the *final* fluctuations of the $|\downarrow\rangle$ chemical potential:

$$\delta\mu_j^{\downarrow} = \eta_1 g^{\downarrow\downarrow}\delta n_j^{\downarrow} + \eta_2 \delta V_j, \tag{4.8}$$

which are reduced by the factors $\eta_1 = \left(g^{\uparrow\uparrow}g^{\downarrow\downarrow} - \left(g^{\uparrow\downarrow}\right)^2\right)/g^{\uparrow\uparrow}g^{\downarrow\downarrow}$ and $\eta_2 = \left(g^{\uparrow\uparrow} - g^{\uparrow\downarrow}\right)/g^{\uparrow\uparrow}$. For the case of ^{87}Rb, $g^{\uparrow\uparrow} \approx g^{\downarrow\downarrow} \approx g^{\uparrow\downarrow}$, to the percent level, so the shielding factors can be around 100. Since the chemical potential is then dependent only on the linear tilt $-j\Delta$, we should see long-lived Bloch oscillations.

4.3.2 Quantum Mechanical Description

The previous section is useful for intuition and calculations in the limit of large atom numbers, but it raises a question. Atom number and condensate phase are conjugate variables, and so cannot both be definite, but the above derivation appears

to treat them as such. In this section, I present a more complete quantum mechanical description that resolves this tension. For this analysis, I will look at the wavefunction on a single lattice site, written in the basis $|n_\downarrow, n_\downarrow + n_\uparrow\rangle$, and assume that all scattering lengths are equal.

First, look at the situation without superfluid shielding, where the atoms begin in a $|\downarrow\rangle$ coherent state

$$\left|\psi\left(0^-\right)\right\rangle = e^{-|\beta|^2/2} \sum_N \frac{\beta^N}{\sqrt{N!}} |N, N\rangle \,. \tag{4.9}$$

Then the only dynamics are phase evolution given by the on-site interaction energy $UN\,(N-1)$ and at later times, the wavefunction is

$$|\psi(t)\rangle = e^{-|\beta|^2/2} \sum_n \frac{\beta^N}{\sqrt{N!}} e^{-iUN(N-1)t} |N, N\rangle \,, \tag{4.10}$$

which diverges from a coherent state and therefore loses its phase information at later times.

On the other hand, in the situation of superfluid shielding, we begin with a coherent state of $|\downarrow\rangle$ atoms within each component of the coherent state of overall atom number

$$\left|\psi\left(0^+\right)\right\rangle = e^{-|\beta|^2/2} e^{-|\alpha|^2/2} \sum_{n<N} \frac{\beta^N}{\sqrt{N!}} \frac{\alpha^n}{\sqrt{n!}} |n, N\rangle \,. \tag{4.11}$$

We allow the wavefunction to evolve under the same operator as above, and at later times the density matrix is

$$\rho(t) = e^{-|\beta|^2} e^{-|\alpha|^2} \sum_{\substack{n<N \\ m<M}} \frac{\beta^N}{\sqrt{N!}} \frac{\alpha^n}{\sqrt{n!}} e^{-iUN(N-1)t} |n, N\rangle \langle m, M| e^{iUM(M-1)t} \frac{\alpha^{*m}}{\sqrt{m!}} \frac{\beta^{*M}}{\sqrt{M!}}. \tag{4.12}$$

Our measurement looks only at $|\downarrow\rangle$ atoms, so we trace over the total atom number to get

$$\mathrm{Tr}_N \rho = e^{-|\beta|^2} e^{-|\alpha|^2} \sum_P \sum_{\substack{n<P \\ m<P}} \frac{\beta^P \beta^{*P}}{P!} \frac{\alpha^n \alpha^{*m}}{\sqrt{n!m!}} |n\rangle \langle m| \,, \tag{4.13}$$

which if the fraction in $|\downarrow\rangle$ is small enough (I.E. $|\alpha|^2$ is sufficiently smaller than $|\beta|^2$), is close to the density matrix for a pure coherent state in $n_\downarrow$ for all time. In our experiments, where $|\beta|^2 \sim 1000$, we need only a small proportion of superfluid component ($|\beta|^2 - |\alpha|^2$) to see good superfluid shielding.

4.4 Experiment

In order to demonstrate the effect of superfluid shielding, we use two spin components in a spin-independent lattice with a spin-dependent force. The experiments start with a BEC in the $|F, m_f\rangle = |1, -1\rangle$ state, levitated against gravity by a magnetic field gradient and confined in a crossed dipole trap made with 1064 nm light. We raise a three-dimensional lattice potential with a lattice spacing of 532 nm in 100 ms. The vertical lattice is always raised to 12 E_r, and the transverse lattice height is varied, which allows us to control the on-site density and therefore interaction parameters.

To create a spin-dependent force, we perform an RF sweep to transfer a fraction of the atoms from the $|\uparrow\rangle \equiv |1, -1\rangle$ state to the $|\downarrow\rangle \equiv |2, -2\rangle$ state. Using an RF sweep makes us robust against fluctuations in the bias field, and allows us to control the fraction of atoms flipped into $|\downarrow\rangle$ by varying the intensity of the RF drive.

The magnetic moment of $|\downarrow\rangle$ atoms is equal to -2 times the magentic moment of the levitated $|\uparrow\rangle$ atoms, and so they feel a force equal to three times gravity, which gives a tilt per lattice site of $\Delta = h \times 3410$ Hz along the vertical direction. tunneling is $\sim h \times 24$ Hz, so for $|\downarrow\rangle$, we are deep in the separated condensate regime. Based on our atom number and harmonic trap, we have about ten pancake shaped condensates, each with up to 3500 atoms. The $|\uparrow\rangle$ atoms remain untilted and act as the superfluid bath. After we prepare the two component system, we allow it to evolve for a variable time before switching off all confining potentials for time-of-flight imaging. During the expansion, we perform a Stern-Gerlach pulse to separate the two spin components, allowing us to image the interference pattern of the $|\downarrow\rangle$ atoms only.

4.4.1 Contrast Fitting

The figure of merit for our experiment is the contrast of the interference pattern. We obtain the contrast from two-dimensional absorption images, which have already integrated the atomic density along the imaging axis (one of the transverse directions). We then integrate along the other transverse direction to get a one-dimensional plot of two-dimensional density as a function of momentum along the tilt direction. For a perfectly coherent cloud, we expect to see a series of peaks whose spacing is given by the lattice spacing, width by the initial spatial extent of the cloud, and overall envelope by the shape of the on-site Wannier function. Our lattice depth is such that only the zeroth and first order peaks are non-negligible. On the other hand, for a perfectly incoherent cloud, we expect to see a single broad peak given just by the envelope function from the Fourier tranform of the Wannier function.

We fit the integrated atomic density to a sum of four Gaussians with appropriate constraints on the fitting parameters to ensure that the fitting routine picks out which three are associated with the coherent part and which one is associated with the incoherent part. We define contrast as the fitted number of atoms under the three coherent peaks divided by the total fitted number of atoms. For most of the following experiments, we report the $1/e$ lifetime of the contrast, which has a one-to-one correspondence to the coherence lifetime.

4.5 Projection Noise Limit Analysis

In order to demonstrate that superfluid shielding can move the coherence lifetime beyond the projection noise limit, we must first calculate what the projection noise limit actually is. We do this by numerically simulating the discrete Gross-Pitaevskii equation in the direction of the tilt. Along the other two directions, we use a discrete Thomas-Fermi profile to find the average occupation number in each two-dimensional pancake. We then project onto states with a definite number, drawn from one of two distributions. If we were to snap the lattice up from a low value, the atom number distribution would be Poissonian. On the other hand, if the lattice ramp

were perfectly adiabatic, the distribution should exhibit some number squeezing (see Section 4.5.2). Since we know our lattice ramps are not perfect, we run the simulations for each distribution, and plot both results, which should place bounds on the true projection noise limit.

Once we have added the number fluctuations to the model, we time evolve the system. Since tunneling is suppressed, we can assume that the only relevant dynamics are given by the two-dimensional Gross-Pitaevskii equation as $|\psi_j(t)\rangle = \exp[-i\mu_j t/\hbar]\,|\psi_j(0)\rangle$ for each pancake at a lattice site j. The chemical potential μ_j is given by the two-dimensional Thomas-Fermi profile to take into account the pancake shape of the condensate on each site, as discussed in Section 4.5.1. After a variable evolution time, we take a Fourier tranformation of the wavefunction to simulate time-of-flight imaging. We average twenty simulated images, and then fit them using the same fitting method as our experimental data. In this chapter, the simulated projection noise limits are marked by dashed black lines for both the upper and lower bounds.

4.5.1 Two-Dimensional Discrete Thomas-Fermi Profile

Since we have lattices in the two transverse dimensions, we slightly modify the normal Gross-Pitaevskii equation in the Thomas-Fermi approximation to

$$\mu_j = U n_{jkl} + \frac{1}{2} m a^2 \left(\omega_z^2 j^2 + \omega_x^2 k^2 + \omega_y^2 l^2\right), \tag{4.14}$$

where U is the Hubbard interaction parameter, a is the lattice spacing, $\omega_{x,y,z}$ are the harmonic trapping frequencies, j is the index along the tilt direction, and k and l are the indices along the two transverse directions. To solve for μ_j, we write

$n_{jkl} = n_j(x,y)$ and find the total atom number in a pancake N_j:

$$\begin{aligned} n_j(x,y) &= \mathrm{Max}\left(\frac{\mu - \frac{1}{2}ma^2\left(\omega_z^2 j^2 + \omega_x^2 k^2 + \omega_y^2 l^2\right)}{U}, 0\right) \\ N_j &= \iint n_j(x,y)\, dxdy \\ &= \frac{\pi}{m\omega_x\omega_y U a^2}\left(\mu_j - \frac{1}{2}ma^2\omega_z^2 j^2\right)^2. \end{aligned} \tag{4.15}$$

Inverting this expression shows us that $\mu_j \propto (N_j U)^{1/2}$.

4.5.2 Two-Mode Number Squeezing Model

In order to determine the maximum number squeezing expected, we use a two-mode model [98], but modify it to take into account the two-dimensional nature of the lattice sites.

This model looks at a double-well system, with a two-dimensional BEC in each well and tunnel-coupling J between them. For large total atom number $2N$, the effective Hamiltonian is

$$H = -J\left(a_l^\dagger a_r + a_r^\dagger a_l\right) + \frac{2\mu_0}{3\sqrt{N_0}}\left(n_l^{3/2} + n_r^{3/2}\right) \tag{4.16}$$

with a_l and a_r as the annihilation operators for the two wells, and n_l and n_r as the respective number operators. At first, the interaction term looks unusual. The form of the interaction term is chosen so that $\mu = \partial E/\partial N \propto \sqrt{N}$ for a single well as required by the two-dimensional Gross-Pitaevskii equation. We have defined the prefactor to make the chemical potential μ_0 when N_0 atoms are in the well.

We can write the Hamiltonian in the Fock state basis of $|n\rangle \equiv |N+n\rangle_l |N-n\rangle_r$:

$$\begin{aligned} H\sum_n c_n |n\rangle = \sum_n [&-J(\sqrt{N+n}\sqrt{N-n+1}c_{n-1} + \\ &\sqrt{N-n}\sqrt{N+n+1}c_{n+1}) + \\ &\frac{2\mu_0}{3\sqrt{N_0}}N^{3/2}\left(2 + \frac{3}{4}\left(\frac{n}{N}\right)^2\right)c_n]\,|n\rangle\,, \end{aligned} \tag{4.17}$$

dropping terms of order $O\left(\left(\frac{n}{N}\right)^4\right)$ and higher. In the spirit of [98], we write $c_{n\pm1}$ as $c_{n\pm1} \equiv C(n \pm 1) = C(n) \pm C'(n) + \frac{1}{2}C''(n) + \ldots$ and then expand the coefficients $C(n),\ C'(n),\ C''(n)$ in powers of $1/N$. Dropping constant terms and all orders higher than $1/N$ gives us

$$\epsilon C(n) = \left(-JN\partial_n^2 + \left(\frac{J}{N} + \frac{3}{4}\frac{2\mu_0}{3\sqrt{N_0}}\frac{1}{N^{1/2}}\right)n^2\right)C(n). \tag{4.18}$$

This has the same form as the Schroedinger equation for the simple harmonic oscillator, and so the ground state is a Gaussian with the width

$$\delta n^2 = N\left(\frac{J}{J + \frac{\mu_0\sqrt{N/N_0}}{2}}\right)^{1/2}. \tag{4.19}$$

4.6 Results

In order to demonstrate the efficacy of superfluid shielding, we performed several different experiments. In Figure 4-3d-f, we present the time-of-flight patterns of the tenth Bloch oscillation after applying a tilt in two scenarios. Figure 4-3d is our control, with all atoms in the tilted state, and no superfluid shielding. It is clear that there is no appreciable phase coherence left in the system. The time-of-flight patterns for a sequence with superfluid shielding are shown in 4-3e-f. Subfigure e is the shielding component, which we can see is not oscillating, demonstrating that $|\uparrow\rangle$ atoms do not feel the gradient. Subfigure f is the oscillating component, whose crisp peaks make clear that the phase coherence is protected by the superfluid shielding. Finally, Figure 4-3g shows the contrast decay for an unshielded (red, for all figures) and shielded (blue, for all figures) system, which we have fit to an exponential to obtain the coherence lifetime. Even by eye, it is clear that the shielded system has a longer coherence lifetime.

Next, we quantitatively compare coherence lifetimes, with and without superfluid shielding, over a range of chemical potentials. In the absence of technical fluctuations, the fundamental limit on coherence lifetime is given by the projection noise

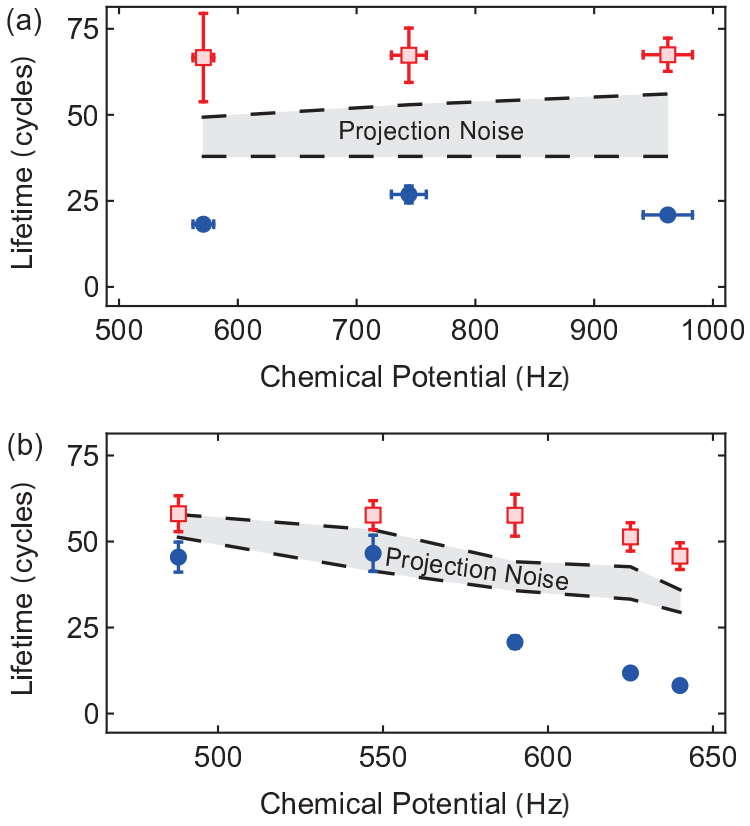

Figure 4-4: Superfluid shielding for different atom numbers and densities. Shown are the exponential decay lifetimes of spin $|\downarrow\rangle$ Bloch oscillating component for unshielded (blue dots) and shielded (red squares) cases versus chemical potential. In (a), the chemical potential is changed by varying atom number from $\sim 6 \times 10^3$ to $\sim 2 \times 10^4$ while keeping the lattice depths at 10 E_r in both transverse directions. In (b), the chemical potential is varied by changing the transverse lattice depth from 4 E_r to 11 E_r. In both plots, the dashed lines represent the projection noise limit given by two theoretical models.

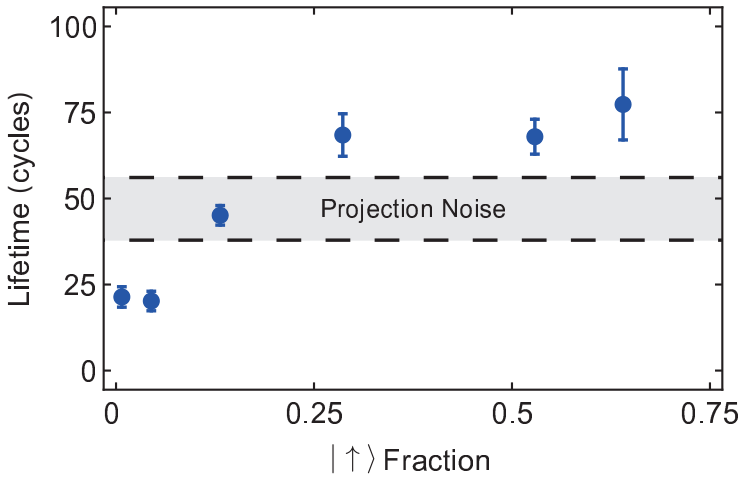

Figure 4-5: Contrast lifetime versus shielding fraction. Exponential decay lifetime of spin $|\downarrow\rangle$ Bloch oscillating component upon varying the number of atoms in spin $|\uparrow\rangle$ state (i.e. fraction of atoms in $|\uparrow\rangle$ state over total number of atoms) indicates that shielding is effective beyond projection noise limits once more than 25% atoms are in the $|\uparrow\rangle$ state.

discussed above. An upper and lower bound for the projection noise limits are plotted as dashed lines in the following figures. In Figure 4-4a, we vary the chemical potential by changing the total atom number. Recall that for a two-dimensional cloud in a harmonic oscillator, $|\partial\mu_j/\partial N_j| \propto N_j^{-1/2}U^{1/2}$. Since the lower bound is given by Poissonian number fluctuations, which are $\propto N_j^{1/2}$, the lower limit is actually independent of atom number, while the upper limit slightly increases with increasing atom number. We observe that the shielded lifetimes in 4-4a are all above the projection noise limit in either model, and are constant to within experimental uncertainty. In Figure 4-4b, we vary the transverse (non-tilted direction) lattice depths while keeping the atom number constant. This varies the chemical potential via U, and we see that the projection noise limit decreases with increasing U. For low U, the shielded and unshielded lifetimes are consistent with the projection noise limits, but at higher U, the unshielded lifetimes are clearly below the projection noise limit, and the shielded lifetimes clearly above it.

Having demonstrated that superfluid shielding with equal weight in both the shielding and oscillating components works over a range of parameters, we next ask

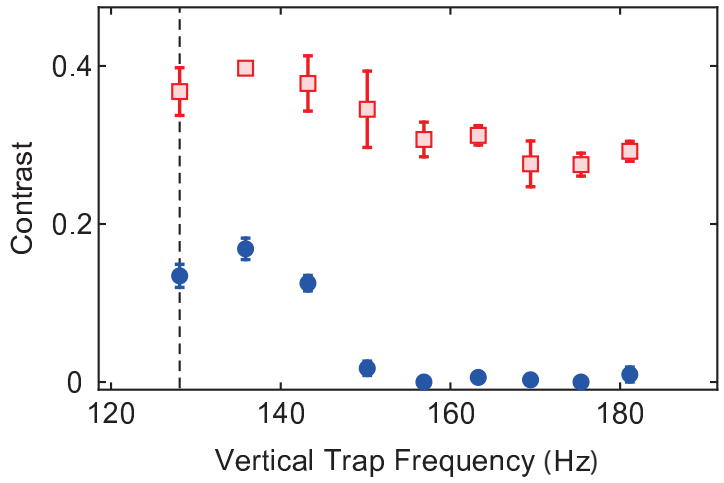

Figure 4-6: Superfluid shielding of external fields, applied by increasing the trap frequency. The vertical dashed line is the initial trap frequency that corresponds to a linear chemical potential for the $|\downarrow\rangle$ atoms. We compare the contrast after 25 Bloch oscillation cycles for unshielded (blue dots) and shielded (red squares) components. In this figure only, for technical reasons, one of the transverse lattices had a spacing of 392.5 nm.

how much of the shielding component is actually needed. If we are limited to a constant total atom number, then there must be a tradeoff: as we increase the fraction in the shielding component f, the signal-to-noise of the measurement decreases by a factor of $\sqrt{1-f}$. In Figure 4-5, we hold the *total* atom number constant and vary the fraction that is in the shielding component to see that as long as the shielding fraction is at least 20-30%, we get the full effect of superfluid shielding., and that at $f \approx 1/2$, we find an increase in lifetime of a factor of 3.2. Thus, the increase in coherence time because of superfluid shielding is much more important than the decrease in signal-to-noise because of the reduced atom number in the measurement component. In principle, the chemical potential of the shielding component needs only be of order the residual fluctuations in the oscillating component to provide full superfluid shielding.

Since $\delta n_j^{\downarrow}/n_j^{\downarrow} \approx 0.02$ is much less than the observed fraction required to achieve full shielding, we most likely have technical sources of dephasing in our system. For unshielded samples in Figure 4-4, we may have introduced chemical potential curvature if the lattice ramp was not fully adiabatic with respect to global density redistribu-

tion. However, this curvature would be common mode to both the $|\uparrow\rangle$ and $|\downarrow\rangle$ atoms, and in principle, superfluid shielding should be able to compensate for this. To test this, we intentionally added common-mode curvature to the system after applying the tilt, when the $|\downarrow\rangle$ density is already frozen in. In Figure 4-6, we increase the vertical trapping frequency from $\omega_i = 2\pi \times 128$ Hz to a variable ω_f, adding a quadratic term $\delta V_j = \frac{1}{2}m\left(\omega_f^2 - \omega_i^2\right) z_j^2$ to the chemical potential. It is clear that added curvature drastically reduces the lifetime of an unshielded system, and that adding superfluid shielding cancels much of this effect.

However, even taking this into account, the increase in shielded lifetimes seen in Figure 4-4 are still lower than the factor of ~ 100, as Equation 4.8 suggests, tells us that there is some non-common-mode disorder in our system. We estimate the curvature of the applied magnetic field to be ~ 100 Hz across the sample, which is consistent with the shielded lifetimes observed.

4.7 Conclusion

In this chapter, I have presented a new method to increase the phase coherence lifetime of separated quantum systems — superfluid shielding. The shielding component, which stays superfluid acts to "fill in the gaps" caused by technical and inherent fluctuations in the chemical potential of the measuring component. We have used Bloch oscillations as a measure of phase coherence to demonstrate that superfluid shielding can increase the coherence lifetime beyond the projection noise limit. Not only is this work directly applicable to force sensors based on Bloch oscillations [30], but it is also part of a growing body of work in atomic clocks [99, 100, 101] and atom interferometers [87, 89] demonstrating that interactions can be useful in precision measurement.

While this work has focused on the phase coherence of the oscillating component, there are also interesting dynamics in the superfluid component. For example, since the mean field of the $|\downarrow\rangle$ atoms acts as disorder for the $|\uparrow\rangle$ superfluid, in certain regimes, we should see localization of the $|\uparrow\rangle$ atoms as well. In addition, adding laser-

assisted tunneling to the tilted component [83, 84, 65] (see Chapter 3) would lead to an interacting system with a spin-dependent synthetic magnetic field.

Chapter 5

Spin-1 Heisenberg Hamiltonian

A major theme of research in ultracold atoms in recent years has been to attempt to achieve low-entropy spin-ordered ground states of magnetic Hamiltonians [102, 103, 104, 105, 106]. The paradigmatic magnetic Hamiltonian is the Heisenberg Hamiltonian, which describes the interactions of quantum spins pinned to a lattice and has many interesting phases. Recently, there has been much success using fermions in quantum gas microscopes to study anti-ferromagnetic order [104, 105, 106], but despite the fact that BECs can achieve much lower temperatures than degenerate fermi clouds, there has been less progress on the bosonic side.

In this chapter, I present a method for using a spinful bosonic Mott insulator to study the spin-1 Heisenberg Hamiltonian [39, 40] and discuss preliminar results. This Hamiltonian has a gapped magnetically ordered state known as the spin Mott insulator, which can be used as a cold starting point for explorations of the phase space. The next state that is most natural for us to look at is the xy-ferromagnet, which is a spin superfluid and exhibits spin-charge separation. I begin by discussing how we map our Bose-Hubbard Hamiltonian onto the Heisenberg Hamiltonian. I then discuss the phase diagram and some special properties of the spin-1 Heisenberg Hamiltonian. I conclude with dicussion of the current state of the experiment and proposals for moving forward.

5.1 Heisenberg from Bose-Hubbard

In order to study the spin-1 Heisenberg Hamiltonian, we use a two-component Mott Insulator with two atoms per site. At first, this seems counter-intuitive — the ground state of ^{87}Rb is in $F = 1$ and so is already a spin-1 system. However, as we describe here, using a pair of spin-1/2 bosons instead of a single spin-1 particles gives us more flexibility and control over the system parameters.

First, we restrict our analysis to sites with exactly two atoms, both in the lowest band. Then because of the symmetry requirements for bosons, the pair of atoms must be in the triplet spin state. For this chapter, we use $|\uparrow\rangle$ and $|\downarrow\rangle$ to represent the physical atomic spins and $|+1\rangle$, $|-1\rangle$, and $|0\rangle$ for the effective spins in the Heisenberg Hamiltonian. We identify the effective spins with the physical states as follows:

$$\begin{aligned} |+1\rangle &= |\uparrow,\uparrow\rangle \\ |0\rangle &= \frac{1}{\sqrt{2}}\left(|\uparrow,\downarrow\rangle + |\downarrow,\uparrow\rangle\right) \\ |-1\rangle &= |\downarrow,\downarrow\rangle\,. \end{aligned} \tag{5.1}$$

In a one-dimensional lattice, the physical Hamiltonian is given by the multi-spin Bose-Hubbard Hamiltonian [39, 40]

$$\begin{aligned} H = &- t_\uparrow \sum_j \left(a^\dagger_{\uparrow,j} a_{\uparrow,j+1} + h.c.\right) - t_\downarrow \sum_j \left(a^\dagger_{\downarrow,j} a_{\downarrow,j+1} + h.c.\right) \\ &+ U_{\uparrow\downarrow} \sum_j \left(n_{\uparrow,j} - \frac{1}{2}\right)\left(n_{\downarrow,j} - \frac{1}{2}\right) \\ &+ \frac{U}{2} \sum_j \left[n_{\uparrow,j}\left(n_{\uparrow,j} - 1\right) + n_{\downarrow,j}\left(n_{\downarrow,j} - 1\right)\right] \\ &- \mu_\uparrow \sum_j n_{\uparrow,j} - \mu_\downarrow \sum_j n_{\downarrow,j} \end{aligned} \tag{5.2}$$

where $a_{\sigma,j}$ and $n_{\sigma,j}$ are the annihilation and number operators for a given spin and lattice site. U is the intra-spin interaction, which is assumed to be symmetric, while the inter-spin interaction $U_{\uparrow,\downarrow}$ can vary. The chemical potentials $\mu_\uparrow$ and $\mu_\downarrow$ are set by the total atom number. To find the effective Hamiltonian, we restrict ourselves to

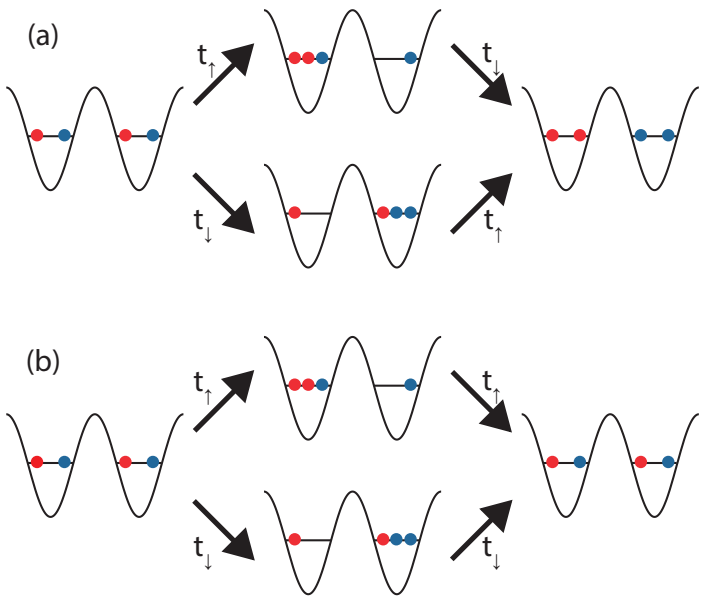

Figure 5-1: Cartoon of the superexchange process. Superexchange is a second order process, with two tunneling events an intermediate virtual particle-hole excitation, which is mapped to terms in the spin Hamiltonian. (a) Superexchange that leads to spin changes give $J_\perp$. (b) Superexchange terms that leave spin unchanged give J_z.

sites with exactly two atoms and define the spin operators

$$\begin{aligned} S_j^+ =& a_{\uparrow,j}^\dagger a_{\downarrow,j} \\ S_j^- =& a_{\downarrow,j}^\dagger a_{\uparrow,j} \\ S_j^z =& \frac{1}{2}\left(n_{\uparrow,j} - n_{\downarrow,j}\right). \end{aligned} \tag{5.3}$$

We can use second-order perturbation theory to find the forms of the coefficients in the spin-1 Heisenberg model:

$$H_{eff} = -\sum_j \left[\frac{J_\perp}{2}\left(S_j^+ S_{j+1}^- + S_j^- S_{j+1}^+\right) + J_z S_j^z S_{J+1}^z\right] + u\sum_j \left(S_j^z\right)^2 - h\sum_j S_j^z. \tag{5.4}$$

Figure 5-1 shows examples of the sort of processes that go into $J_\perp$ and J_z, known as *superexchange*. Figure 5-1a shows one process that lowers the spin in the right well by one while raising the spin in the left well. In the intermediate state, there is an energy deficit of U, so the matrix element $J_\perp \propto t_\uparrow t_\downarrow / U$. In Figure 5-1b, the state goes back to the initial state through two different paths, so we can see that $J_z \propto \left(t_\uparrow^2 + t_\downarrow^2\right)/U$.

The $\left(S_j^z\right)^2$ term u is the energy difference between having two atoms of the same spin on one site and one of each, and h is the difference in chemical potentials. The full analysis [39, 40] gives the following coefficients:

$$\begin{aligned} J_\perp =& \frac{4t_\uparrow t_\downarrow}{U} \\ J_z =& 2\frac{t_\uparrow^2 + t_\downarrow^2}{U} \\ u =& U - U_{\uparrow\downarrow} \\ h =& \mu_\uparrow - \mu_\downarrow, \end{aligned} \tag{5.5}$$

and so when $t_\uparrow = t_\downarrow = t$, the spin term is symmetric:

$$\frac{J_\perp}{2}\left(S_j^+ S_{j+1}^- + S_j^- S_{j+1}^+\right) + J_z S_j^z S_{J+1}^z = \frac{4t^2}{U}\vec{S}_j \cdot \vec{S}_{j+1}. \tag{5.6}$$

5.1.1 Spin-Dependent Lattice

Our experiments are all done in an optical lattice, which allows us to easily vary t and U, but the novel piece of the experiment comes from our control over $U_{\uparrow\downarrow}$. If the Wannier functions for the two atomic species are $w_{\uparrow,\downarrow}(\vec{r})$, we can write

$$U_{\uparrow\downarrow} = \frac{4\pi\hbar^2 a_{\uparrow\downarrow}}{m}\int d\vec{r}\left|w_\uparrow(\vec{r})\right|^2\left|w_\downarrow(\vec{r})\right|^2, \tag{5.7}$$

where for ^{87}Rb, the S-wave scattering length $a_{\uparrow\downarrow}$ is approximately spin-independent. In other atoms, including ^{7}Li, Feshbach resonances are available to vary the ratio of $a_{\uparrow\downarrow}/a_{\uparrow\uparrow}$, but for ^{87}Rb, the Feshbach resonances are either too lossy or at too high of a field. Instead, we focus on the second part of Equation 5.7, the overlap between the Wannier functions of the two spins.

To do this, we use an effect known as the vector AC Stark shift. In Section 2.1, we introduced the scalar AC Stark shift by treating an atom as a two-level system exposed to an oscillating electromagnetic field. The AC Stark shift associated with a

specific intermediate state is given by

$$V = -2\pi\alpha a_0^2 I \frac{|M_{gi}|^2}{\delta}, \tag{5.8}$$

where M_{gi} is the dipole matrix element between the ground state and the intermediate state being off-resonantly addressed and δ is the detuning from that resonance. (For simplicity, we have dropped the counter-rotating term.) If δ is large, we can generally ignore the fine and hyperfine structure, and treat the laser field as addressing one combined resonance. However, closer to the atomic resonance, this assumption breaks down and we have to take different M_{gi} and δ_i into account. In general, the matrix elements will depend on the starting state, the intermediate state, and the polarization of the light. We will restrict ourselves to looking at circularly polarized light σ^+ or σ^- and will look at the combined effect for the D1 line and the D2 line. We will denote the possible matrix elements as $M^{+,-}_{(\uparrow,\downarrow)(1,2)}$. We also assume that $|\uparrow\rangle$ and $|\downarrow\rangle$ form a pair in the ground state manifold $|F, \pm m_f\rangle$. Finally, we define the energy difference between the D1 and D2 lines Δ_{FS} and let the detuning δ be the detuning from the midpoint between the lines.

We write the potentials as

$$V^{+,-}_{(\uparrow,\downarrow)} = -2\pi\alpha a_0^2 I \left(\frac{\left|M^{+,-}_{(\uparrow,\downarrow),1)}\right|^2}{\delta + \Delta_{FS}/2} + \frac{\left|M^{+,-}_{(\uparrow,\downarrow),2)}\right|^2}{\delta - \Delta_{FS}/2} \right) \tag{5.9}$$

and by symmetry, we can say

$$\begin{aligned} V^+_\downarrow &= V^-_\uparrow \\ V^-_\downarrow &= V^+_\uparrow. \end{aligned} \tag{5.10}$$

For a given polarization, the two spins will feel different potentials. We define the common-mode part of the potential to be the scalar AC Stark shift and the differential potential to be the vector AC stark shift. In general, when we interfere two linearly-polarized laser beams of the same frequency, we will get both an intensity lattice, as usual, and a polarization lattice, where the polarization changes from σ^+ to linear

and then σ^- and back. In this case, we can associate the intensity lattice with the scalar shift and the polarization lattice with the vector shift. With a few symmetry relations, we can say

$$\begin{aligned} V_{vec} \propto & \frac{1}{\delta + \Delta_{FS}/2} - \frac{1}{\delta - \Delta_{FS}/2} \\ \propto & \frac{\Delta_{FS}}{\delta^2} \end{aligned} \tag{5.11}$$

for large δ.

Now if we use the states $|1, \pm 1\rangle$ and a polarization lattice, we can separate the two spins and therefore reduce $U_{\uparrow\downarrow}$. There are two ways to do this. The conceptually simplest way has us creating two independent lattices at the same wavelength, one with a polarization σ^+, and one with σ^-. We retro-reflect both of them off the same mirror, which forces the standing waves to both have a zero at that point. We can give them a slight frequency offset δf, and if the distance between the atoms and the retro-reflecting mirror is l, then at the atoms, the two lattices will have a phase difference of $2\pi\frac{2l\delta f}{c}$. This is most easily implemented by using a double-pass AOM on one of the arms to give a variable frequency offset. Unfortunately, this is relatively power inefficient, so for most of this work, we use a second method. In this method, the input beam is linearly polarized, and in the retro-reflecting path, we have a quarter-waveplate and liquid crystal phase retarder, which when combined and double-passed rotate the linear polarization by a variable amount. Two linearly polarized beams with their polarizations at an angle to each other create lattices of σ^+ and σ^- light with a phase offset between the sublattices that varies from 0 when the polarizations are parallel to π when they are perpindicular.

Finally, we note that while the vector Stark shift is non-zero at large detunings, the scalar-to-vector ratio scales as δ. At high scalar-to-vector ratios, two effects are important. First, the effect of the curvature of the gaussian envelope of the lattice beam, which is usually negligible, is given by the scalar Stark shift, and so becomes dominant at large δ. In addition, if we have any polarization impurity when we are attempting to separate the sublattices by π, this will lead to a small intensity lattice whose strength scales with the scalar Stark shift. Therefore, at large detunings, we

are extremely sensitive to polarization fluctuations or impurities, leading to a practial upper limit on the detuning at which we can work.

5.2 Spin-1 Heisenberg Hamiltonian Phase Diagram

Before going into the details of the experiment, we wish to discuss the phase diagram of our system, as well as the states that are available to us, the xy-ferromagnet and the spin Mott insulator. Following [40], we can make the ansatz that the ground state wavefunction of the spin-1 Heisenberg Hamiltonian will have the form

$$|\Psi\rangle = \prod_j \left(\cos\left(\frac{\theta}{2}\right) |0\rangle_j + e^{i\eta} \sin\left(\frac{\theta}{2}\right) \left(e^{i\phi} \cos\left(\frac{\chi}{2}\right) |1\rangle_j + e^{-i\phi} \sin\left(\frac{\chi}{2}\right) |-1\rangle_j \right) \right). \tag{5.12}$$

We wish to look for the phase transition between the xy-ferromagnet, which is a spin superfluid, and the spin Mott insulator, so in analogy with charge superfluids, which use $\langle a \rangle$ as their order prarameter, we look at

$$\langle S_j^- \rangle = \frac{1}{\sqrt{2}} e^{i\eta} \sin\theta \left(e^{-i\phi} \sin\left(\frac{\chi}{2}\right) + e^{i\phi} \cos\left(\frac{\chi}{2}\right) \right) \tag{5.13}$$

and define the order parameter $\psi = \sin\theta$. We then plug our ansatz into the Hamiltonian to get the energy functional

$$\begin{aligned} E =& -\frac{J_\perp}{2} \sin^2\theta \left(1 + \sin\chi \cos 2\eta\right) - J_z \sin^4\frac{\theta}{2} \cos^2\chi + u \sin^2\frac{\theta}{2} - h \sin^2\frac{\theta}{2} \cos\chi \\ =& -\frac{J_\perp}{2} \psi^2 \left(1 + \sin\chi \cos 2\eta\right) - J_z \left(1 - \sqrt{1-\psi^2}\right)^2 \cos^2\chi + (u - h\cos\chi) \left(1 - \sqrt{1-\psi^2}\right) \\ =& \left(-\frac{J_\perp}{2} \left(1 + \sin\chi \cos 2\eta\right) + \frac{u}{4} - \frac{h}{4} \cos\chi \right) \psi^2, \end{aligned} \tag{5.14}$$

where in the last line, we have dropped all terms higher order than ψ^2. Our experiments are done with equal $|\uparrow\rangle$ and $|\downarrow\rangle$ atom number, so we can set $h = 0$. In addition, we see that $\sin\chi \cos 2\eta$ is bounded in $[-1, 1]$, and so the energy is minimized when $\sin\chi \cos 2\eta = 1$ and

$$E = \left(-J_\perp + \frac{u}{4} \right) \psi^2. \tag{5.15}$$

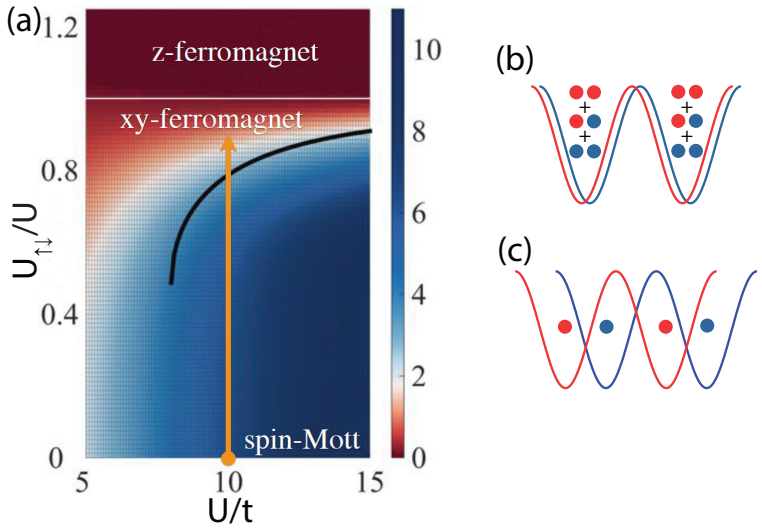

Figure 5-2: (a) Phase diagram of the spin-1 Heisenberg Hamiltonian with DMRG calculations from [39]. The color scale gives the calculated gap in units of t for a system of 12 particles on 6 sites. (b) At high $U_{\uparrow\downarrow}$, u is small and the ground state is an xy-ferromagnet, with a superposition of $|0\rangle$ and $|\pm 1\rangle$ on each lattice site. (c) When $U_{\uparrow\downarrow}$ is small, u dominates the system and the ground state is a spin Mott insulator, with $|0\rangle$ on every site.

The phase transition occurs where the energy switches from being minimized by $\psi = 0$ to being minimized by a non-zero ψ, or in other words, when

$$\frac{J_\perp}{u} = \frac{1}{4}, \tag{5.16}$$

which is the black line plotted in Figure 5-2a, along with DMRG calculations from [39]. We should note that the DMRG calculations give a phase transition at a higher $J_\perp/u$ than the mean field calculations done here, but this is not surprising because mean field calculations are known to be innacurate for one-dimensional systems.

5.2.1 xy-Ferromagnet

The variational ansatz, despite its slight disagreement with some DMRG calculations, provides intuition for the form of the wavefunction and can be used to calculate observables useful for our experiment. We first want to look at the properties of the "deep" xy-ferromagnet.

First, we set $\chi = \pi/2$ and $\eta = 0$, which minimize Equation 5.14 as discussed above. For the deep xy-ferromagnet, the order parameter ψ is maximized, and since $\psi = \sin\theta$, we set $\theta = \pi$, giving us a wavefunction of

$$|\psi_{xy}\rangle = \prod_j \left(\frac{1}{\sqrt{2}} |0\rangle_j + \frac{1}{\sqrt{2}} \left(\frac{e^{i\phi}}{\sqrt{2}} |1\rangle_j + \frac{e^{-i\phi}}{\sqrt{2}} |-1\rangle_j \right) \right). \tag{5.17}$$

From this, we immediately see that the population on any site is in a superposition of $|0\rangle$ and $|\pm 1\rangle$, with weights 1/2, 1/4, and 1/4, respectively. We also see that there is a free phase ϕ, which does not appear in the energy function Equation 5.14. This leads to Goldstone modes and gapless excitations from long-wavelength variations in ϕ across the system, and thus Equation 5.17 gives the ground state when all ϕ_j are equal. In order to get a better intuition of the form of these excitations, we can write the wavefunction in the atomic basis

$$|\psi_{xy}\rangle = \prod_j \left[\frac{\left(e^{i\phi_j/2} |\uparrow\rangle + e^{-i\phi_j/2} |\downarrow\rangle \right)}{\sqrt{2}} \otimes \frac{\left(e^{i\phi_j/2} |\uparrow\rangle + e^{-i\phi_j/2} |\downarrow\rangle \right)}{\sqrt{2}} \right]. \tag{5.18}$$

From this, it is clear that the xy-ferromagnetic ground state has exactly two atoms on a site, each with a spin pointing along the equator of the Bloch sphere with a direction given by ϕ. Thus, variations in ϕ should be interpreted as gapless spin waves, and we can think of the xy-ferromagnet as a superfluid in the spin sector. Interestingly, the state always has exactly two atoms per site, and normal charge tunneling is forbidden, so the state is still a charge insulator. Therefore, the xy-ferromagnet shows spin-charge separation, a very unusual and interesting property.

5.2.2 Spin Mott

The xy-ferromagnet occurs in both the spin-1/2 and the spin-1 Heisenberg Hamiltonian, but we chose to implement the spin-1 version for the following state, which occurs when the $\left(S_j^z\right)^2$ term is dominant. We call this state the spin Mott, and in the same way that the xy-ferromagnet is a superfluid in spin space, this is a Mott

insulator. Deep in the spin Mott, the wavefunction is given by

$$|\psi\rangle = \prod_j |0\rangle_j = \prod_j \frac{1}{\sqrt{2}} \left(|\uparrow,\downarrow\rangle_j + |\downarrow,\uparrow\rangle_j \right) \tag{5.19}$$

and the state has a gap of u.

The form of the ground state is clearest in the limit of $u = U$, or when $U_{\uparrow\downarrow} = 0$, which occurs when the σ^+ and σ^- lattices are offset by π. Then, we can think of the system as two interleaved, but non-interacting Mott insulators, each with exactly one atom per site. It is obvious then that we must have exactly one atom of each type per site, and that we are protected by the normal Mott insulator gap U, which should make adiabatic ramps into the spin Mott easier than into the xy-ferromagnet.

In our experimental system, we have an additional harmonic confining potential, which forces us to use the local density approximation. Thus, when the center of the cloud is in the spin Mott state, it will be surrounded by a superfluid, which has no gap. For a system in thermal equilbrium, entropy will be pushed from the gapped to the gapless part of the cloud, leaving the center at a locally lower entropy than average. This acts as additional cooling if we are later able to selectively measure the Mott insulating shell only.

5.3 Experiment

Our goal is to ramp into the ground state of the xy-ferromagnet by using the spin Mott insulator as a cold starting point. We start with a BEC of $|F = 1, m_f = -1\rangle$ atoms in a bias field of $\sim$9 G, after using a dimple trap and side evaporation to precisely control the atom number. We then convert the atoms into an equal mixture of $|1, 1\rangle = |\uparrow\rangle$ and $|1, -1\rangle = |\downarrow\rangle$ atoms via two Landau-Zener transitions through $|2, 0\rangle$. A three-dimensional lattice is ramped up to take the system into a Mott insulating state. The two transverse arms are made by spin-independent 1064 nm beams, while the lattice arm along the direction of the magnetic field bias is our spin-dependent lattice. We use a Ti-sapphire laser with a wide tuning range to create the spin-dependent lattice and

determine the separation between the σ^+ and σ^- sublattices by one of the methods discussed in Section 5.1.1. We can then move the sublattices to ramp $U_{\uparrow\downarrow}/U$ through the phase diagram.

5.3.1 On-Site Correlations

Once we have prepared a state, we first wish to measure the on-site correlations. For this, we will ignore the phases ϕ_j and look only at the spin population on a site. Since we know that we have an equal number of $|\uparrow\rangle$ and $|\downarrow\rangle$ atoms, measuring the fraction of sites that are in $|0\rangle$ will also tell us how many are in $|\pm1\rangle$. We also need to note that because the harmonic traps cause density variation across the cloud, not all atoms are in an $n = 2$ Mott insulating state. Thus, we need to measure the fraction of atoms in $|0\rangle$ relative to those in sites which have exactly two atoms, which we call the "spin-paired doublon fraction," or SPDF.

Figure 5-3 demonstrates how we measure the SPDF in three different experimental runs. At the end of each run, we ramp up the lattice height and merge the spin-dependent sublattices together, projecting the system to a set of independent sites, each with a fixed atom number and spin configuration. In the first run, we measure the total atom number N using an intrap absorption image. For the second run, we want to measure the number of atoms in $|0\rangle$. This is done through the use of a lossy Feshbach resonance [107, 108]. We use an RF sweep to convert the $|1,-1\rangle$ atoms to $|2,-2\rangle$, which have a Feshbach resonance with $|1,1\rangle$ at 9.045 G. We then sweep the bias field to this value and modulate it for 25 ms. During this time, the sites that started in $|0\rangle$ (i.e. the sites with one atom of each spin) will decay through Feshbach loss, while the $|\pm1\rangle$ sites stay stable. Measuring the remaining atom number and subtracting from N gives us the number of atoms in $|0\rangle$. Finally, we need to measure the fraction of atoms that are on an $n = 2$ site. We first use an RF sweep to flip all of the $|1,-1\rangle$ atoms to $|2,0\rangle$, which has a lossy Feshbach resonance with $|1,1\rangle$ at 9.091 G. As before, we shift and modulate the bias field, but that is not enough to kill all of the $n = 2$ sites, so we additionally perform about ten 50:50 Landau-Zener sweeps between $|1,1\rangle$ and $|2,0\rangle$. If a site started in $|0\rangle$, then it will decay after the

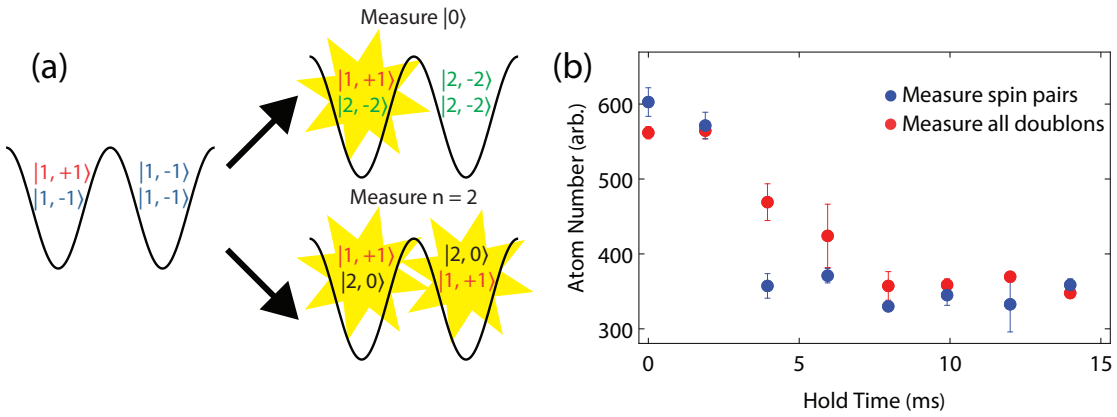

Figure 5-3: Description of our measurement for on-site correlations. (a) To measure the spin-paired doublon fraction (SPDF), we used three experimental runs. First, we measure the total atom number. In the second run, we flip the $|1,-1\rangle$ atoms into $|2,-2\rangle$, which has a lossy Feshbach resonance with $|1,1\rangle$, so all of the sites with one spin of each type will decay. For the third run, we flip the $|1,-1\rangle$ atoms into $|2,0\rangle$ and then perform several incomplete Landau-Zener sweeps between it an $|1,1\rangle$. This causes all of the sites with two atoms to decay. (b) Here we plot the atom number remaining as a function of hold time during the Feshbach loss process for a spin Mott initial state. We see that for both of the processes, the loss saturates by 10-15 ms, which is much shorter than any other relevant time scales in the system.

first sweep. On the other hand, a site that started in $|\pm 1\rangle$ has a 50% chance to turn have one of each spin and therefore decay after a 50:50 Landau-Zener sweep. After the ten sweeps, all but a negligible fraction ($(1/2)^{10} \sim 0.1\%$) of the $n = 2$ sites have decayed, while $n = 1$ sites are unaffected. Again, by measuring the atom number remaining and subtracting from N, we can get the total number of atoms in $n = 2$ sites. The ratio of these two results gives us the SPDF.

There are three important possible results that we could get when we measure the SPDF. First, look at a system in a thermal state with a temperature T, larger than the Heisenberg energy scales, but lower than the Mott insulator gap, $u, J_\perp, J_z \ll T \ll U$. Then the three possible spin states should be equally populated, and the SPDF will be 1/3. For a spin Mott insulator or an xy-ferromagnet, the wavefunctions from Section 5.2 give an SPDF of 1 and 1/2 respectively.

5.3.2 Off-Site Correlations

While the spin Mott is a relatively simple system, with no off-site correlations, much of the xy-ferromagnet's interesting properties come from offsite correlations. Recall that the ground state wavefunction is

$$|\psi_{xy}\rangle = \prod_j \left[\frac{1}{\sqrt{2}}|0\rangle + \frac{1}{\sqrt{2}}\left(\frac{e^{i\phi_j}}{\sqrt{2}}|1\rangle + \frac{e^{-i\phi_j}}{\sqrt{2}}|-1\rangle\right)\right]. \tag{5.20}$$

If all of the ϕ_j are equal, then we are in the ground state. On the other hand, non-constant ϕ_j are caused by some excitations or spin waves. We can quantify the level of excitation with the spin correlation $\left\langle S_0^+ S_j^- + S_0^- S_j^+ \right\rangle$. There are two ways in which we can measure the correlation length.

Fluctuation Analysis

To understand the first way to measure correlation length, write the wavefunction in the atomic basis

$$|\psi_{xy}\rangle = \prod_j \left[\frac{\left(e^{i\phi_j/2}|\uparrow\rangle + e^{-i\phi_j/2}|\downarrow\rangle\right)}{\sqrt{2}} \otimes \frac{\left(e^{i\phi_j/2}|\uparrow\rangle + e^{-i\phi_j/2}|\downarrow\rangle\right)}{\sqrt{2}}\right] \tag{5.21}$$

and note that we can interpret this wavefunction as having two atoms on each site, each of which is on the equator of the Bloch sphere, with a direction given by ϕ_j. To measure the correlation length, we apply a $\pi/2$-pulse and measure the resulting polarization, defined as $(N_\uparrow - N_\downarrow)/N$. Even in the perfect case of constant ϕ_j across the cloud, the result will be random, as it depends on $\phi_{mw} - \phi_j$, where ϕ_{mw} is the uncontrolled phase given by our microwave source and ϕ_j is spontaneously chosen by the system. However, looking at the fluctuations in the polarization over many iterations can tell us the number of domains and therefore the correlation length. Each domain, after the $\pi/2$-pulse, becomes a patch of constant polarization. Since the domains are uncorrelated, the fluctuation of the average polarization will scale as $1/\sqrt{N_{\text{domains}}} \sim \sqrt{l_{corr}}$, where l_{corr} is the correlation length. Note that other fluctuations (e.g. fluctuations in initial polarization) will add to this measure, and so this

can only give us an upper bound on the correlation length.

Arbitrary Order Spin Correlations

While the above method can give us a measure of the correlation length, it makes no distinction between true random domains and something like a phase gradient caused by a slight magnetic field gradient. In order to distinguish between the two, we present a method that uses the spin-dependent lattice to measure arbitrary order spin correlation functions in an $n = 1$ xy-ferromagnet.

Look at the wavefunction at sites 0 and j of the xy-ferromagnet

$$|\psi_{xy}\rangle = \frac{e^{i\phi_0}|\uparrow\rangle_0 + |\downarrow\rangle_0}{2} \otimes \frac{e^{i(\phi_0+\delta)}|\uparrow\rangle_j + |\downarrow\rangle_j}{2} \otimes |\psi_{else}\rangle \tag{5.22}$$

where $\delta = \phi_j - \phi_0$ and $|\psi_{else}\rangle$ is the wavefunction on all sites except for 0 and j. Then the spin correlation can be related to δ as

$$\begin{aligned} C_S =& \left\langle S_0^+ S_j^- + S_0^- S_j^+ \right\rangle \\ =& \frac{e^{i\delta}}{4} + \frac{e^{-i\delta}}{4} \\ =& \frac{\cos(\delta)}{2}. \end{aligned} \tag{5.23}$$

We define $R_{\pi/2}$ to be a $\pi/2$-rotation operator, and the shift operator S_j to be the operator that shifts $|\downarrow\rangle$ atoms over by j sites, so that $|\downarrow\rangle$ atoms that start on site k end up at the same position as $|\uparrow\rangle$ atoms starting at site $k + j$. This can be implemented by adding $2\pi j$ to the phase difference between σ^+ and σ^- lattices [109]. Finally, we denote the effect of interaction term of the Bose Hubbard Hamiltonian $W(t) = \exp[-iU\sum_k (n_{\uparrow,k} + n_{\downarrow,k})((n_{\uparrow,k} + n_{\downarrow,k}) - 1)]$, where we have assumed that $U_{\uparrow\downarrow} = U$, as is valid when the phase difference between the sublattices is a multiple of 2π.

We can measure δ by use of a Ramsey-style sequence:

$$|\psi_f\rangle = R_{\pi/2} S_j^\dagger W(t)\, S_j R_{\pi/2} |\psi_{xy}\rangle . \tag{5.24}$$

Let us go step-by-step to understand this sequence. First, the $\pi/2$-rotation transforms the state on each site into a mixture of $|\uparrow\rangle$ and $|\downarrow\rangle$ with weights $\sin^2(\phi_j/2)$ and $\cos^2(\phi_j/2)$, respectively. We have converted phase information into population information. $W(t)\,S_j$ allows the $|\downarrow\rangle$ component on site 0 to interact with the $|\uparrow\rangle$ component on site j. If there is a non-zero δ, then the shift operation will move more atoms away from site j and the site receives from site 0 or vice versa. Then, since the action of $W(t)$ depends only on the total atom number per site, a phase will be imparted that directly depends on the value of δ. We then shift the lattice back, and perform a second $\pi/2$-rotation, which converts the phase information created by $W(t)$ into population on site 0.

Measuring the polarization on site 0 gives us

$$\begin{aligned}\left\langle \frac{n_{\uparrow,0}-n_{\downarrow,0}}{n_{\uparrow,0}+n_{\downarrow,0}} \right\rangle =& -\cos^2\left[\frac{\phi_0+\delta}{2}\right]\sin[Ut]\sin[\phi_0] \\ =& \frac{\sin[\delta]}{4}\end{aligned} \tag{5.25}$$

where for the second line we have assumed that t is chosen such that $\sin[Ut] = 1$, and we have averaged over ϕ_0. Thus, we can measure spin correlations to arbitrary distances, limited only by how quickly we can apply the shift operator without losing phase coherence.

5.4 Results

Our first experiments looked at the on-site spin correlations of a Mott insulator with varying distances between the spin-dependent sublattices. The spin-dependent lattice was given a polarization structure using the liquid crystal phase retarder and quarter-waveplate setup discussed in Section 5.1.1, and was held at a wavelength of 810 nm, slightly red-detuned of both the D1 and D2 line. With the liquid crystal phase retardance held constant, we raised up a three-dimensional lattice to 25 E_R in the transverse directions, and 10 E_R in the spin-dependent lattice direction. In Figure 5-4, we plot the spin-paired doublon fraction versus the ratio of inter-spin to intra-spin

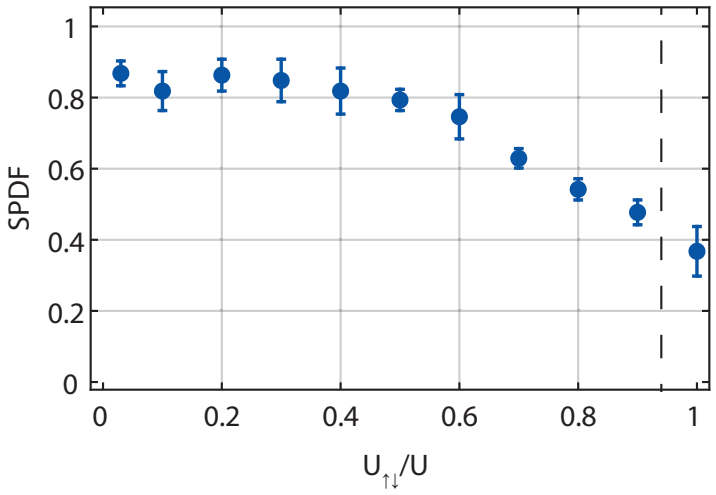

Figure 5-4: Spin paired doublon fraction after ramping directly into the Mott insulator at varying $U_{\uparrow\downarrow}/U$. For this experimental run, we used two 25 E_R lattices in the transverse directions and an 10 E_R spin-dependent lattice. The dashed line marks the expected phase transition point calculated in [39]. We see that deep in the spin Mott, we have a SPDF near one, and that at $U_{\uparrow\downarrow} = U$, we have a thermal Mott insulator.

interactions $U_{\uparrow\downarrow}/U$ at the final lattice depth.

Near $U_{\uparrow\downarrow}/U = 0$, we are in the deep spin Mott, and we see that the SPDF is approximately 1. The phase transition from a spin Mott to an xy-ferromagnet occurs at $U_{\uparrow\downarrow}/U = 0.94$ [39] and is marked by the dashed line. While we would expect the SPDF to stay near one up until the phase transition, we instead see that it starts to drop around $U_{\uparrow\downarrow}/U = 0.4$, indicating that our ramp is not perfectly adiabatic for small u. On the other end, at $U_{\uparrow\downarrow}/U = 1$, if we were perfectly cold, we would be in the xy-ferromagnet, but we instead achieve a SPDF that is consistent with 1/3, a thermal Mott insulator, as discussed above.

Instead, in order to prepare the xy-ferromagnet, we want to use the spin Mott as a cold starting state. To do this, we first ramp the lattices up in the deep spin Mott $U_{\uparrow\downarrow}/U = 0$ configuration before ramping the liquid crystal retardance and spin-dependent lattice intensity to keep the lattice depth constant but change the sublattice separation and therefore $U_{\uparrow\downarrow}/U$. In Figure 5-5, we plot the final SPDF at different final $U_{\uparrow\downarrow}/U$. The SPDF begins to drop before the phase transition, but at $U_{\uparrow\downarrow}/U = 0.6$, rather than 0.4, and the SPDF at $U_{\uparrow\downarrow}/U = 1$ is between 1/3 and the 1/2 that we

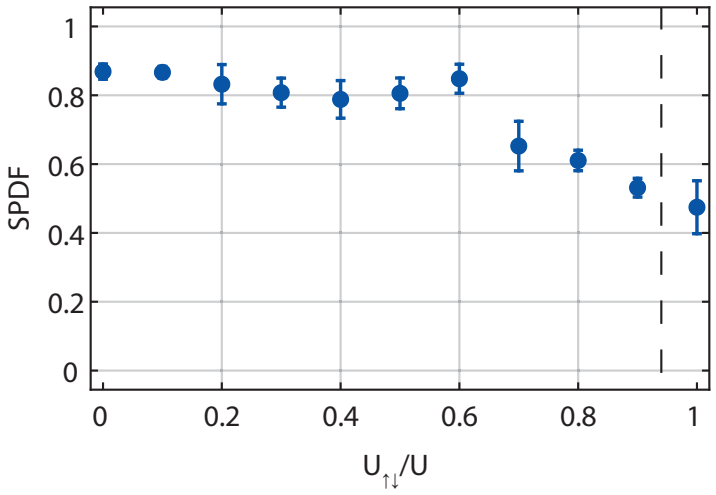

Figure 5-5: Spin paired doublon fraction after ramping from the spin Mott insulator to varying $U_{\uparrow\downarrow}/U$. As before, we used two 25 E_R lattices in the transverse directions and an 10 E_R spin-dependent lattice, and the dashed line marks the expected phase transition point calculated in [39]. At $U_{\uparrow\downarrow} = U$, we see that the SPDF is between 1/3 and 1/2, which tells us that we are doing some cooling with this sequence, but not enough to be truly in the xy-ferromagnet.

expect for an xy-ferromagnet. Our sequence is doing some cooling, but not enough.

At first, this is confusing, since we can consistently make what appear to be high-purity spin Mott insulators. However, our measurements until now have looked exclusively at spin temperature. The paradigmatic charge excitation in a Mott insulator is a "hole," or a site with one fewer atom than expected. Our spin measurement procedure cannot distinguish a hole from a site that is in the surrounding superfluid or $n = 1$ shell, and therefore normalizes them out. First, look at the effect of a hole in the deep spin Mott, as in Figure 5-6a. In this regime, we can think of the system as two interleaved $n = 1$ Mott insulators — one for each spin. Therefore, a hole is simply an empty site in one of these two Mott insulators, and that site is unmeasured. A hole on the $|\uparrow\rangle$ sublattice can only tunnel to another site on that lattice, and so also with a $|\downarrow\rangle$ hole. Therefore, a hole tunneling event will simply change the position of the excitation, but will not change the total number of sites with $|0\rangle$ on them.

Figure 5-6b shows the effect of holes for a shallow spin Mott or an xy-ferromagnet. If u is comparable to the hole bandwidth $\sim 4t$, then from a site next to a hole, either a $|\uparrow\rangle$ atom or a $|\downarrow\rangle$ atom can tunnel to fill the hole, regardless of the second atom

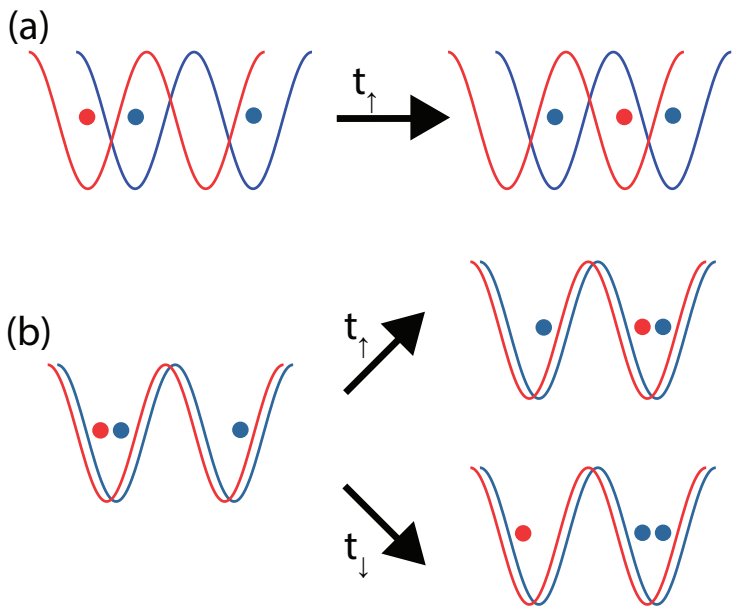

Figure 5-6: Cartoon of the effect of hole tunneling on the measured SPDF. (a) In a deep spin Mott, a hole tunneling event will not change the SPDF, and therefore charge and spin excitations are decoupled. (b) When $u \lessapprox 4t$, some tunneling events (top) preserve SPDF, but others (bottom) can cause a spin excitation.

sitting on the hole site. If the tunneling atom happens to be the one "missing" on the other site, then the SPDF is unchanged. However, if it is the wrong spin state, this will create a spin excitation.

To measure charge excitations, after creating the state we are interested in, we adiabatically ramp the lattices down to 0 E_R and perform time-of-flight imaging. We fit to a bimodal distribution and extract the condensate fraction, which is a measure of the entropy in the system. In Figure 5-7 we see the measured condensate fraction for one- and two-component clouds at various spin-dependent sublattice differences. We note that both adding a second spin component and moving towards $U_{\uparrow\downarrow}/U = 0$ significantly hurt the condensate fraction.

In order to get a quantitative understanding of the numbers involved in Figure 5-7, we calculate the relationship between the measured condensate fraction CF, and the hole fraction at the center of the Mott insulator. For an ideal BEC of N atoms,

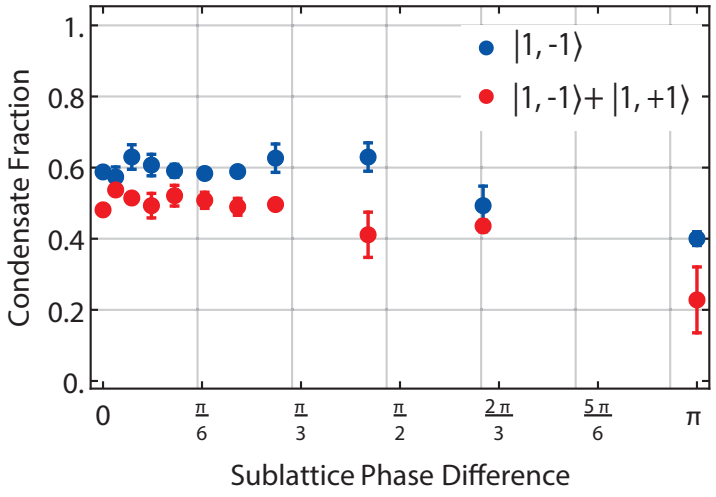

Figure 5-7: Initial condensate fraction measurements after ramping back to BEC. For these measurements, we ramped up a three-dimensional 20 E_R lattice, held for 10 ms, and ramped back to BEC before measuring the condensate fraction in time-of-flight. The spin-dependent lattice was made with 810 nm wavelength light, and we varied the phase difference between the σ^+ and σ^- sublattices. At a phase difference of 0, $U_{\uparrow\downarrow} = U$, while a phase difference of π corresponds to $U_{\uparrow\downarrow} = 0$. We report condensate fractions measured for one component (blue) and two component (red) systems.

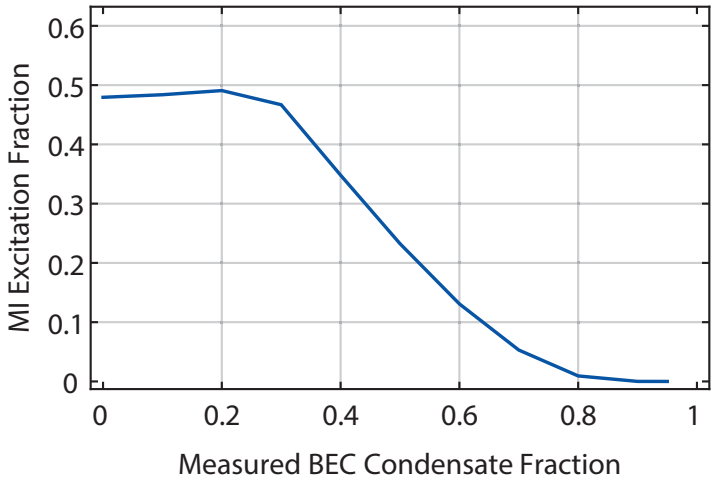

Figure 5-8: Calculated excitation fraction at the center of the Mott insulator as a function of measured condensate fraction when ramped down to BEC.

the total entropy is given by

$$S = 3.602\, k_B N \left(1 - CF\right). \tag{5.26}$$

To find the entropy associated with the Mott insulator, we ignore tunneling and look at each individual site, which has an energy $E_n = \frac{U}{2} n\left(n-1\right) - n\mu$. We can find the partition function and average filling for a given temperature and chemical potential:

$$\begin{aligned} Z =& \sum_{n=0}^{\infty} e^{-\frac{E_n}{k_B T}} \\ \langle n \rangle =& \frac{\sum_{n=0}^{\infty} n e^{-\frac{E_n}{k_B T}}}{Z}. \end{aligned} \tag{5.27}$$

To find the entropy on a given site, we recall

$$\begin{aligned} F =& -k_B T \ln[Z] \\ S =& -k_B \frac{\partial F}{\partial T}. \end{aligned} \tag{5.28}$$

Finally, given a known harmonic confinement, we can make the local density approximation $\mu \to \mu - V(\vec{r})$ and sum over all lattice sites to get a total entropy and atom number. We numerically find the chemical potential and temperature required to have the entropy and atom number in the Mott insulator match that which is measured in the BEC. From there, it is easy to find the excitation fraction at the center of the Mott insulator. Figure 5-8 plots the Mott insulator excitation fraction versus the measured condensate fraction for representative parameters for a single-component $n = 1$ Mott insulator, which should be equivalent to our system at $U_{\uparrow\downarrow}/U = 0$. We see that a measured condensate fraction of ~ 0.65 is equivalent to about 10% charge excitation fraction in the Mott insulator, and that lower condensate fractions are correspondingly worse.

Over the past year, we have performed several upgrades to the experimental sequence and apparatus, which have led to increased condensate fraction in the single component system. In Figure 5-9, we plot the condensate lifetime of the system with

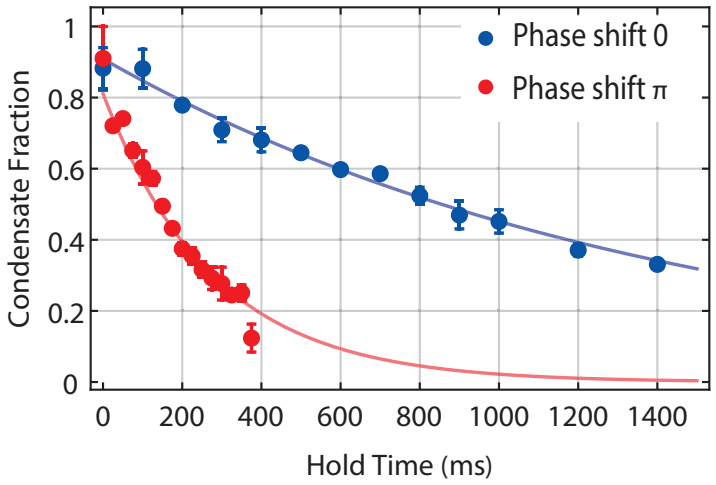

Figure 5-9: Condensate fraction measurements after experimental upgrades. Here, we plot the condensate fraction lifetime measurements for a one-component system with 20 E_R in all three directions and a spin-dependent lattice wavelength of 810. These lifetimes were measured after the upgrades discussed in the text.

all three lattices at 20 E_R, and a spin-dependent lattice wavelength of 810 nm. The starting condensate fraction and $1/e$ lifetime at a phase shift of 0 are 0.91 and 1,400 ms, respectively, and are 0.81 and 280 ms for a phase shift of π. Both of these are notably better than the previous condensate fractions, leading us to believe that we may be able to ramp into the xy-ferromagnet as described above.

The most important upgrades are as follows:

- We empirically found the optimal shape for a piecewise linear lattice ramp with ten pieces. The optimal ramp closely matches a form of $\exp\left[(t/\tau)^7\right]$, which we use in order to reduce the search space to one parameter whenever we change the lattice depth or sublattice phase.

- We set all lenses at a small angle to the optical axis, to ensure that stray reflections from the lens do not hit the atoms.

- We ensure that all dipole beams, lattice beams, and retro beams are aligned to the center of the cloud to within 2 μm.

- We added passive low frequency vibration isolation with a corner frequency $\sim$10 Hz to the breadboard that supports the two non-vertical retroreflection mirrors.

The last two items seem initially surprising, since the conventional wisdom is that a Mott insulator is robust against any noise with a frequency less than its gap at U. While this is true, the initial purity of a Mott insulator state is extremely sensitive to excitations during the lattice ramp up, where we cross a phase transition and the excitation gaps close.

5.5 Spontaneous Scattering

It appears that in the spin Mott configuration, when the lattice intensity is highest, the condensate fraction lifetime is limited in part by spontaneous scattering, which is a process where an atom will accept a photon from the spin-dependent lattice to go into a virtual excited state, which then decays to some spin state (maybe not the same one) and emits a real photon. The emitted photon can destroy any phase coherence the atom initially had and can scatter atoms into higher bands. For a single intermediate state, the scattering rate takes the form

$$R = \frac{8\pi\alpha^2 a_0^4 I}{3\hbar c^2}\omega^3 \left|M_{i\to f}\right|^2 \tag{5.29}$$

where α and a_0 are the fine structure constant and the Bohr radius. The local intensity of the lattice beam and its frequency are denoted I and ω, and the second order perturbation theory matrix element for the transition from intial spin state i to the final spin state f is $M_{i\to f}$. It is tempting to treat scattering from the D1 and D2 lines separately, and simply add the rates given by analyzing each one by itself. This will work for large detunings, but is not valid close to the atomic resonance. For a set i and f, we must linearly add the matrix elements associated with different intermediate states, and then square the magnitude. To find the total scattering rate of an atom in state i, we can then add in quadrature the matrix elements associated with different final states f, as these processes cannot interfere.

For far detunings δ, the scattering rate drops as $\sim 1/\delta^2$, which is the same scaling as the vector AC Stark shift discussed in Section 5.1.1. This seems to imply that

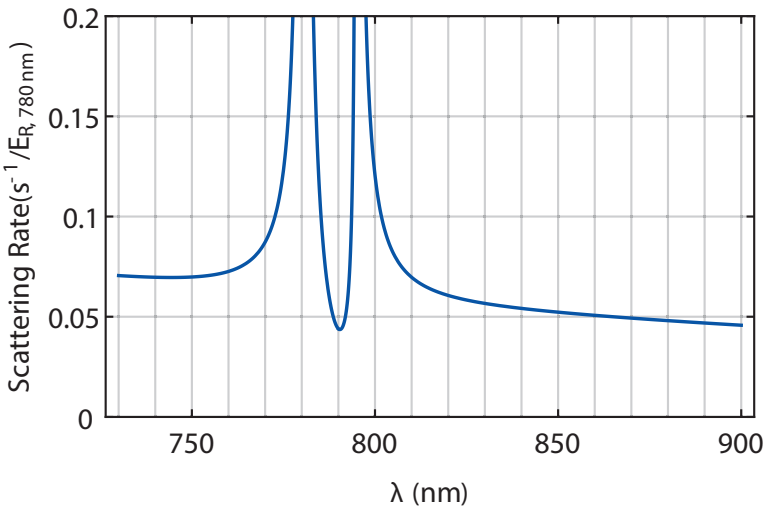

Figure 5-10: Calculated photon scattering rate of an atom sitting in a purely vector AC Stark shift lattice of 1 $E_{R,\,780\,nm}$. We see that at large detunings, the scattering rate is flat with wavelength, but near resonance there is non-trivial structure and optimization to be had.

the spin-dependent lattice wavelength does not matter, and that the heating rate will always be the same. The analysis is more subtle for several reasons. First, look at Figure 5-10, which shows the calculated scattering rate for a vector Stark shift of 1 $E_{R,\,780\,nm}$. At wavelengths greater than ~ 820 nm, the scattering rate dependence on wavelength is flat, but closer to resonance, we can find scattering rates that are much greater.

In addition, not all spontaneous scattering is the same. As shown in Figure 5-11, at far detunings, most of the scattering is Rayleigh scattering, which preserves the atomic spin and will only add band excitations. On the other hand, at closer detunings and between the D1 and D2 lines, scattering is dominated by Raman scattering, where the atom is flipped to a different spin state. If the new spin state has a different magnetic moment than the initial spin state, after scattering, the atom will be sitting at the maximum rather than the minimum of the potential. This highly excited state has much more energy than a band excitation.

Finally, although much of our work so far has been in the fully separated regime of $U_{\uparrow\downarrow}/U = 0$, we have seen evidence that we can make a relatively cold spin Mott with $U_{\uparrow\downarrow}/U$ up to at least 0.4. For this configuration, the lattice potential has both vector

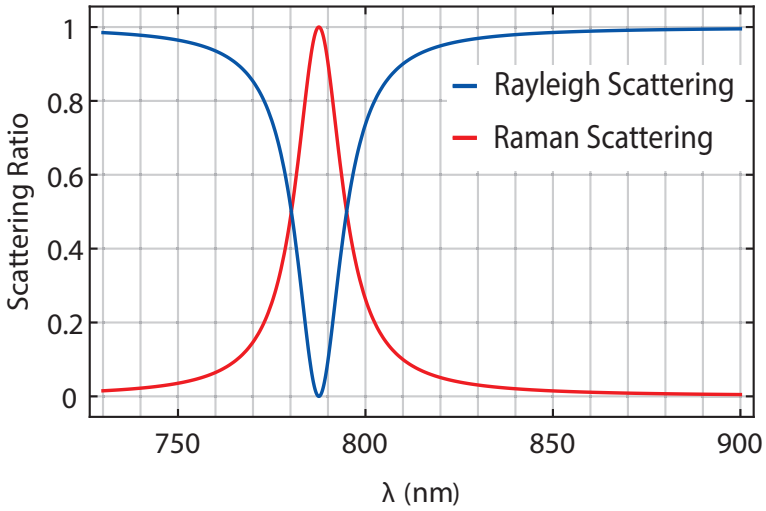

Figure 5-11: Scattering fraction of Raman and Rayleigh scatteing off of a σ^- lattice. We see that when the lattice wavelength is between the D1 and D2 lines, spin-changing (Raman) scattering events are dominant, while at far detunings, spin-preserving (Rayleigh) scattering dominates.

and scalar Stark shift components, and so the required intensity scales somewhere between δ and δ^2, leading to a scattering rate that decreases sub-linearly with δ at far detunings. Therefore, we believe that the optimal wavelength for the spin-dependent lattice is as far detuned as possible given power constraints and the curvature and stability considerations in Section 5.1.1.

5.6 Conclusion

In this chapter, I have presented a method for using a two-component Mott insulator and a spin-dependent lattice to create a highly tunable spin-1 Heisenberg Hamiltonian. We have already shown that we can create a spin Mott insulator that is cold in spin space and discussed possible upgrades to reduce the charge excitations. Once this is done, we will be able to use the measures discussed here to read out both on-site and off-site spin correlations through the clever use of RF fields, Feshbach resonances, and the spin-dependent lattice.

For future work, there are two main directions that could increase the flexibility and stability of the system. First, we are currently working on designing and installing

a quantum gas microscope that will have single site resolution. In addition to single-site readout, this allows us to project arbitrary potentials, which can be used as a "cookie cutter" to remove entropy from the system once the spin Mott has pushed it into the superfluid wings.

The second possible upgrade is the addition of a large gradient along the spin-dependent lattice direction. If we are in the spin Mott state, and then quickly apply a gradient $\Delta \gg t$, normal tunneling is frozen out. This will localize all the charge excitations, which travel with t and will not allow entropy flow from the superfluid edges to the center. In addition, for a strong enough tilt, the first excited band will be strongly coupled to the continuum, and any band excitations will escape. This will mean that instead of depositing a bandwidth and possibly a bandgap of energy and the corresponding entropy into the system, each band excitation will result in only one lost particle, which is much lower entropy. Finally, we note that this tilt, while it blocks normal tunneling, still allows for superexchange. Instead of the normal $J = t^2/U$, the superexchange tunneling will be renormalized to $t^2/(U - \Delta)$, which can be much higher than the normal J and even change sign. This will allow us to explore new regimes of the spin-1 Heisenberg Hamiltonian phase space, including the possibility of observing the Haldane phase [110].

Chapter 6

Conclusion

The work in this thesis has covered applications of ultracold bosons in optical lattices to both precision measurement and quantum simulation. It is unified in its focus on the phase coherence between different lattice sites.

Chapter 4 presented the work most closely related to precision measurement and had the most obvious connection to phase coherence. When condensates sitting on different sites in a lattice are separated, either by applying a strong energy gradient or by rapidly increasing the lattice depth, each condensate's phase evolves independently of the others, with a phase evolution given by the local energy. Since in a condensate, interactions are generally non-negligible, density fluctuations lead to noise in the phase evolution and thereby dephasing between the condensates on separate sites. We presented and explored the technique of superfluid shielding, which uses the interactions with a superfluid bath to cancel out the effects of density fluctuations, which allows the separated condensates to maintain phase coherence. We have demonstrated that superfluid shielding can protect against fundamental projection noise as well as common-mode external curvature, and this method should allow for greater coherence in BEC atom interferometers. In addition, the system used here, where one spin feels a strong magnetic tilt and the other does not, should have dynamics that are interesting in themselves, like localization of the superfluid component or potentially a spin-dependent synthetic gauge field.

In Chapters 2 and 5, we present work on quantum simulation. Chapter 2 dis-

cusses our simulation of the Harper-Hofstadter Hamiltonian, which describes charged particles in a high magnetic field. The ground state of a simple lattice superfluid, without a magnetic field, has a simple phase pattern — every site has a coherent state of atoms on it, all of which have the same phase. On the other hand, the ground state of a Harper superfluid has the same constant density, but a complex phase pattern, like that of a vortex lattice. In our system, this phase pattern is given by the complex tunneling that we have added to the system using a tilt and laser-assisted tunneling. However, in general, if we start with a trivial superfluid and immediately switch to a novel Hamiltonian, we will end in some highly excited mixture of states without phase coherence between lattice sites. We have explored two ways to get around this and transform a trivial superfluid into a ground-state Harper superfluid. In the first, we use a two-dimensional lattice, so that the condensate on each site is a long one-dimensional tube. Immediately after switching from the Bose-Hubbard to the Harper-Hofstadter Hamiltonian, there is no phase coherence between the lattice sites, as we feared. However, the excitations in the lattice direction quickly thermalize with the tube direction, which has many low-lying excited states. Each tube needs only accept $\sim$1 k_B of entropy to fully restore phase coherence, and so we still achieve a cold sample. This method allowed us to study the single particle physics of the Hamiltonian, including demonstrating the gauge-dependent nature of some observables. To observe the result of strong interactions, we needed a three-dimensional lattice, so this loading technique was unavailable. Instead, we created a many-body adiabatic sequence. In this loading sequence, we started with a trivial superfluid and adiabatically ramped into the deep Mott insulator, where the ground state has a definite number on each site, and therefore no well-defined phase. Then, we switch the Hamiltonian to the Harper-Hofstadter Hamiltonian with interactions, which also has a Mott insulating regime. From there, we "melt" the Mott insulator into a relatively cold Harper superfluid. This allowed us to study the lifetime of the interacting Harper superfluid near the Mott insulating transtion and will be a useful tool in future simulations of interacting systems.

The work on simulating the spin-1 Heisenberg model is discussed in Chapter 5.

Since phase is a continuous variable, the presence of phase correlations is generally associated with gapless excitations. Because we work exclusively in a Mott insulating shell, one may think that there is no phase coherence, and so we have some measure of protection. While this is true in the charge sector, the xy-ferromagnet has a phase in the spin sector. One can picture the ground state xy-ferromagnet as having a spin on every lattice site pointing in the same direction along the equator of the Bloch sphere. The direction within the plane is given by the phase, so any phase gradients or fluctuations are interpreted as spin waves. These gapless excitations make it difficult to adiabatically ramp directly from a BEC into the xy-ferromagnet, so we propose and study a ramping sequence similar to the many-body adiabatic sequence used above. We first wish to ramp from a BEC into the spin Mott insulator, which has no phase coherence in either spin or charge space and has a gapped excitation spectrum. This protects our system from non-adiabaticities and noise during the initial ramp-up. Then, once we are in the spin Mott phase, we wish to ramp into the xy-ferromagnet, where phase correlations will be created by superexchange processes. In this work, we have focused on the first part, and have begun by creating a spin Mott insulator that is cold in spin space. Technical upgrades, as discussed in Chapter 5, have reduced our charge temperature to the point that adiabatic ramps to the xy-ferromagnet are in reach.

In the near future, our lab is planning a major upgrade — adding a quantum gas microscope to the setup, which will greatly expand our capabilities. We are using a custom-made objective with an NA of 0.8 and a long working distance of 11 mm. The objective will sit directly on the top window, which also provides a reference for the vertical lattice. This removes three degrees of freedom from the objective alignment (focus and two angles from the optical axis) and so should be more stable against long-term alignment drifts.

The most obvious application of the quantum gas microscope is for single-site imaging. By allowing us to directly image particle-hole excitations, it will speed the optimization of lattice ramps and Mott insulator preparation. In addition, single-site readout will make measuring nearest neighbor correlations in the xy-ferromagnet

much easier. Single-site imaging is not the only benefit of a quantum gas microcsope — perhaps the more important one is that it allows for single-site addressing of the applied potential. Ramping to a Mott insulator in a harmonic trap pushes entropy out into the superfluid wings of the system. With a microscope, we can add a sharp wall at the edge of the Mott insulating region of the cloud to act as a "cookie-cutter" and selectively remove the high entropy superfluid wings, leaving us with an even colder system to start our simulations in. Another use of projected potential walls is to create sharp edges, which will allow us to image the topological edge currents associated with a Harper superfluid. By combining our lab's expertise in laser-assisted tunneling and spin-dependent lattices with the new tools provided by a microscope, we will open new doors in the realm of quantum simulation.

Appendix A

Lattice Noise Measurements

In order to achieve a low entropy in our spin Mott insulating state, we must minimize excitations driven by external noise. In this appendix, I report on emprical studies of noise coming from our lattices, as measured in Spring 2018.

We assume that all of our heating in the deep lattice is parametric heating of separate harmonic oscillators, with frequency ω_0, equal to the bandgap. Then we are only sensitive to intensity noise at $2\omega_0$ and phase noise at ω_0.

The calculated excitation rates $R_{0\to2}$ and $R_{0\to1}$ are given by

$$R_{0\to2} = \frac{\pi\omega_0^2}{8} S\left(2\omega_0\right) \tag{A.1}$$

$$R_{0\to1} = \frac{\pi m\omega_0^3}{2\hbar} S_x\left(\omega_0\right) \tag{A.2}$$

where $S\left(\omega\right)$ is the power spectral density of the relative intensity noise of the laser measured in $1/\mathrm{s}^{-1}$, and $S_x\left(\omega\right)$ is the power spectral density of the phase noise of the laser and retro mirror, measured in $\mathrm{nm}^2/\mathrm{s}^{-1}$.

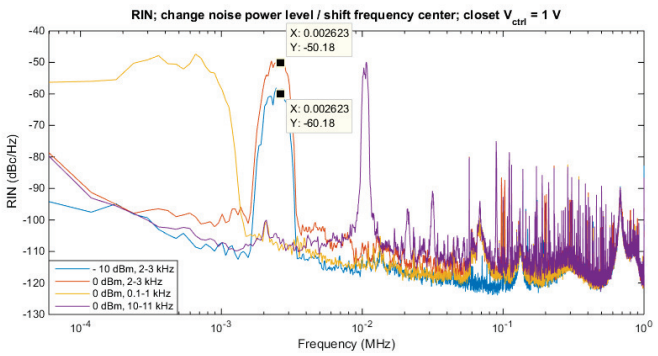

Figure A-1: Intensity spectrum after injecting noise at various frequencies. This plot shows that our injection is linear up to at least tens of kiloHertz.

A.1 Empirical Measure of Condensate Fraction Decay

Regardless of the calculations that we do, an empirical way to tell whether we are limited by noise is to first measure the noise present in the system. Then add noise until the injected noise is a few dB above background, and see if this affects the coherence lifetime. Note that for the phase noise measurements so far, we have measured with the interferometer and the mirror on the same breadboard, so there may be common-mode vibration that we do not measure.

A.1.1 Intensity Noise

We inject intensity noise into the closet arm (1064 nm light) simply by directly adding intensity noise to the output of the PID controller of our intensity stabilization. Figure A-1 shows that this process is linear up to tens of kiloHertz. We see that injecting 0 dBm noise with a 1kHz bandwidth gives a response of about -50 dBc/Hz, while the background noise is around -110 dBc/Hz at twice the bandgap, which is about 26 kHz for a 19 E_R lattice. If we plug these numbers into Equation A.1, we calculate a rate of 4×10^{-3} s^{-1} for the background noise.

In Figure A-2, we inject intensity noise at twice the bandgap in a 19 E_R Mott Insulator for 100 ms. We see that we have to inject noise above -20 dBm to significantly heat our atoms. This corresponds to -70 dBc/Hz, which is 40 dB above

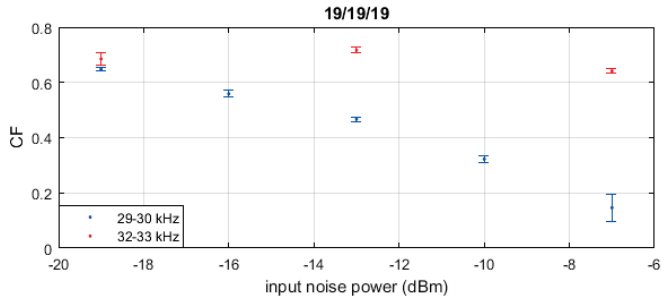

Figure A-2: Condensate fraction lifetime with intensity noise applied.

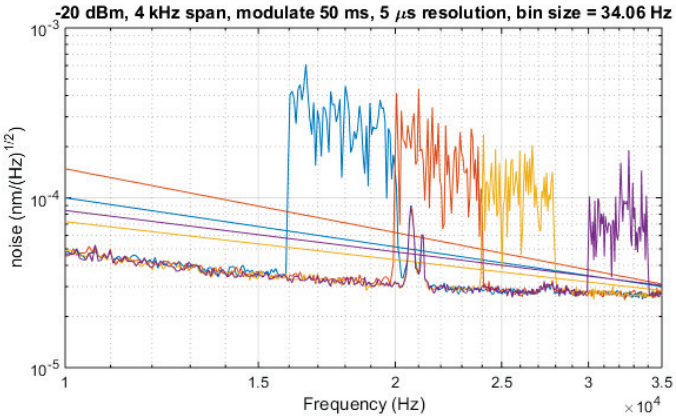

Figure A-3: Spectrum after injecting phase noise at -20 dBm at various frequencies. Note that at 16-20 kHz, we are about 10 dB above background.

background in heating, where, theory predicts an excitation rate of 40 s^{-1}. Since we needed to inject noise that is so much higher than the background to see an effect, we can conclude that the intensity noise at the bangap is not the primary heating source.

A.1.2 High Frequency Phase Noise

In Figure A-3, we see that injecting noise at -20 dBm in boxed white noise from 16-20 kHz gives us noise that is about 10 dB above background in amplitude. The bandgap for a 1064 nm lattice at $24E_R$ is around 18 kHz, and the background phase noise is about 3×10^{-5} nm/$\sqrt{\text{Hz}}$. If we plug these numbers into Equation A.2, we calculate a rate of 5×10^{-4} s^{-1}.

We measured the lifetime of the condensated fraction with different noise intensities, as seen in Figure A-4, and fit to exponential decays with lifetimes given in Table

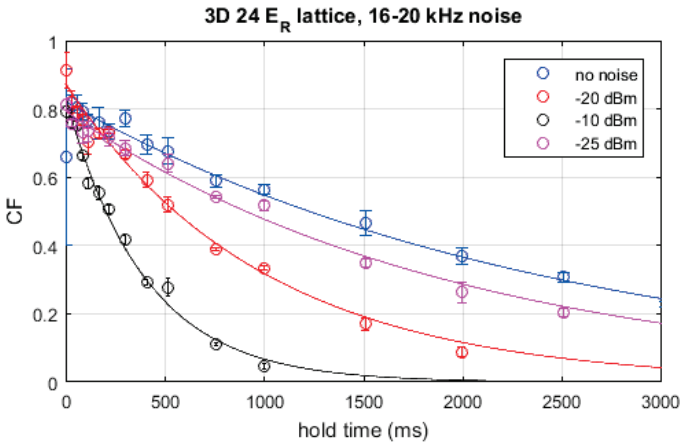

Figure A-4: Condensate fraction lifetime with high-frequency phase noise applied.

Table A.1: $1/e$ lifetimes of a $24E_R$ Mott Insulator with 16-20 kHz noise added.

Noise Intensity (dBm)	dB above background	Lifetime (ms)
None	0	2480 ± 170
-25	10	1970 ± 190
-20	20	990 ± 90
-10	30	400 ± 40

A.1. We see that if we go about a factor of ten in amplitude (which should be a factor of a hundred in heating) above the background, we only get a factor of about two change in lifetime. If we add a further factor of ten in noise intensity, to -10 dBm, we get only an additional factor of two in lifetime.

A.1.3 Low Frequency Phase Noise

In Figure A-5, we see that mirrors mounted like the vertical retro have about 10 dB extra amplitude noise at low frequencies, but are similar to the horizontal-type retro mirrors at bandgap frequencies. We want to see if this higher low-frequency phase noise possibly heats the atoms. We can add -12 dBm of phase noise from 0.6-1.3 kHz, which raises the low frequency noise by more than 10 dB in amplitude above background. As seen in Figure A-6 and Table A.2, we see little increase in the heating rate when we add -12 dBm noise. When we increase the noise injection by 20 dB in intensity (which should be a factor of a hundred in heating) we only see a decrease in lifetime of a factor of four or five.

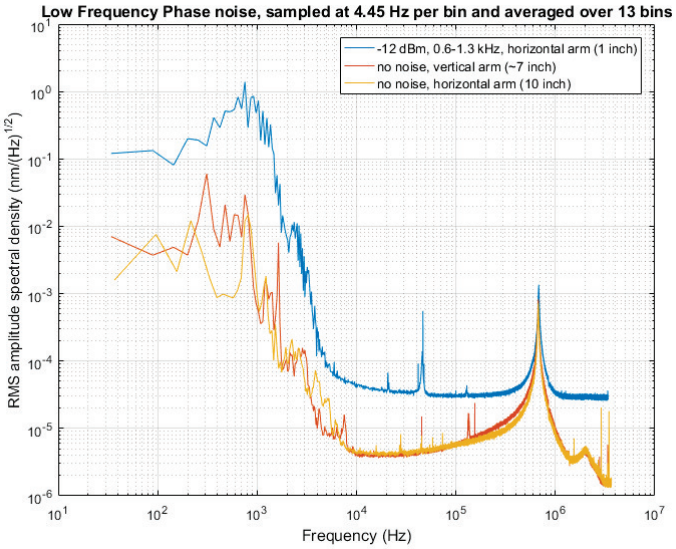

Figure A-5: Spectrum after injecting -12 dBm phase noise at low frequencies. The legend gives the lattice arm-length.

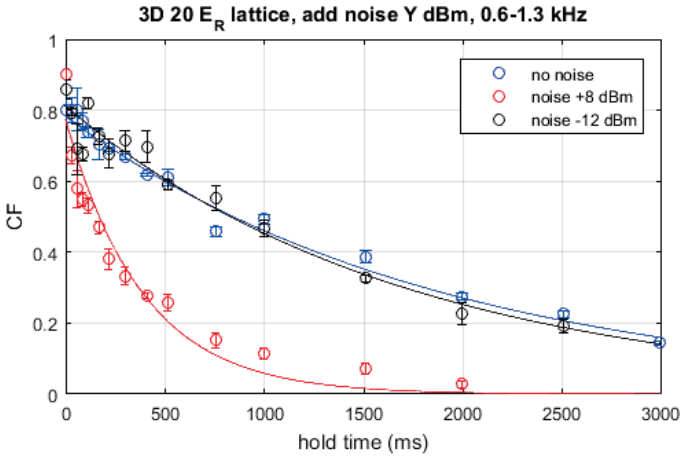

Figure A-6: Condensate fraction lifetime with low-frequency phase noise applied.

Table A.2: $1/e$ lifetimes of a 20 E_R Mott Insulator with 0.6-1.3 kHz noise added.

Noise Intensity (dBm)	dB above background	Lifetime (ms)
None	0	1890 ± 170
-12	20	1720 ± 270
+8	40	390 ± 100

A.1.4 Conclusion

Given the above data, we can conclude that intensity noise on the lattices is definitely not limiting our Mott insulator lifetime. For phase noise both at the bandgap and at low frequencies, the situation is complicated by the sub-linear scaling that we see in heating rate. We expect the inverse lifetime to be insensitive to added noise while the heating rate associated with it is lower than the background heating, and for it to then scale linearly with the intensity of added noise once we pass the background threshold. Instead, we see non-zero but strongly sublinear behavior. This may point to a saturation effect, but further study is needed before definitive statements can be made.

Appendix B

Realizing the Harper-Hamiltonian with Laser-Assisted Tunnneling in Optical Lattices

This appendix contains a reprint of [22], which was touched on, but not discussed in detail in the main text.

Realizing the Harper Hamiltonian with Laser-Assisted Tunneling in Optical Lattices

Hirokazu Miyake, Georgios A. Siviloglou, Colin J. Kennedy, William Cody Burton, and Wolfgang Ketterle

Research Laboratory of Electronics, MIT-Harvard Center for Ultracold Atoms, Department of Physics, Massachusetts Institute of Technology, Cambridge, Massachusetts 02139, USA

(Received 6 August 2013; published 28 October 2013; publisher error corrected 28 October 2013)

We experimentally implement the Harper Hamiltonian for neutral particles in optical lattices using laser-assisted tunneling and a potential energy gradient provided by gravity or magnetic field gradients. This Hamiltonian describes the motion of charged particles in strong magnetic fields. Laser-assisted tunneling processes are characterized by studying the expansion of the atoms in the lattice. The band structure of this Hamiltonian should display Hofstadter's butterfly. For fermions, this scheme should realize the quantum Hall effect and chiral edge states.

DOI: 10.1103/PhysRevLett.111.185302 PACS numbers: 67.85.−d, 03.65.Vf, 03.75.Lm

Systems of charged particles in magnetic fields have led to many discoveries in science—including both the integer [1] and the fractional [2,3] quantum Hall effects—and have become important paradigms of quantum many-body physics [4]. Generalizations have led to important developments in condensed matter physics, including topological insulators [5,6], fractional Chern insulators [7,8], and Majorana fermions [9,10]. At high magnetic fields, exotic new phenomena like the fractal energy spectrum of Hofstadter's butterfly [11] are predicted to emerge. Its direct observation would require an inaccessibly high magnetic field of one flux quantum per unit cell—corresponding to ∼10000 T in a traditional condensed matter system. Recently, some aspects of Hofstadter's butterfly were addressed using superlattices in high magnetic fields [12–15].

Neutral atoms provide an excellent platform to simulate the physics of charged particles in magnetic fields free from disorder. Rotating quantum gases realize the limit of weak magnetic fields, exploiting the equivalence between the Lorentz force and the Coriolis force. The observed vortex lattices [16,17] are analogous to magnetic flux lattices. A more general method to create synthetic magnetic fields for neutral atoms is based on the insight that vector potentials introduce spatially varying phases ϕ into the wave function when the particle propagates $\phi = \oint \mathbf{A} \cdot \mathbf{ds}/\hbar$, where the charge is included in the vector potential. For neutral atoms, such a phase structure can be realized through Berry phases, when two hyperfine states of the atom are coupled by Raman lasers with inhomogeneous intensity or detuning [18,19]. This concept of coupling of two or several internal states to realize synthetic magnetic fields was also suggested in optical lattice geometries [20–22]. Here, the crucial element is laser-assisted hopping between neighboring sites which imprints the phase of the laser into the atomic wave function. Alternatively, instead of using Raman laser beams, lattice modulation techniques can generate complex tunneling matrix elements in optical lattices [23,24]. Experimentally, these techniques have been used so far only to realize staggered magnetic fields [24,25]. In the Munich experiment, the two internal states in the proposed schemes [20,22] were replaced by doubling the unit cell of the optical lattice using superlattices [25].

So far, all proposals for generating high magnetic fields are based on the coupling of different internal states. For alkali atoms, this involves different hyperfine states [20]. Spin flips between such states require near-resonant light which heats up the sample by spontaneous emission. At least for staggered fluxes, the realizations with lattice shaking and superlattices demonstrate that internal structure of the atom is not essential. Here, we suggest and implement a scheme which realizes the Harper Hamiltonian [26], a lattice model for charged particles in magnetic fields, the spectrum of which is the famous Hofstadter's butterfly [11]. Our scheme requires only far-off-resonant lasers and a single internal state. It is an extension of a scheme suggested by Kolovsky [27], which was shown to be limited to inhomogeneous fields [28], but as we show here, an additional momentum transfer in the laser-assisted hopping process provides a simple solution. While this work was in progress [29], an identical scheme was proposed by the Munich group [30]. In this Letter, we describe the features and implementation of this scheme, and characterize the laser-assisted hopping process.

We start with the simple Hamiltonian for noninteracting particles in a 2D cubic lattice

$$H = -\sum_{m,n} (J_x \hat{a}^\dagger_{m+1,n} \hat{a}_{m,n} + J_y \hat{a}^\dagger_{m,n+1} \hat{a}_{m,n} + \text{H.c.}), \quad (1)$$

where $J_{x(y)}$ describes tunneling in the x (y) direction and $\hat{a}^\dagger_{m,n}$ ($\hat{a}_{m,n}$) is the creation (annihilation) operator of a particle at lattice site (m, n). Tunneling in the x direction is then suppressed by a linear tilt of energy Δ per lattice site, where Δ/h is the Bloch oscillation frequency. This tilt can be created with magnetic field gradients, gravity, or an ac Stark shift gradient. Resonant tunneling is restored with two far-detuned Raman beams of two-photon Rabi frequency Ω, frequency detuning $\delta\omega = \omega_1 - \omega_2$, and momentum transfer $\delta\mathbf{k} = \mathbf{k_1} - \mathbf{k_2}$, as shown in Fig. 1(a).

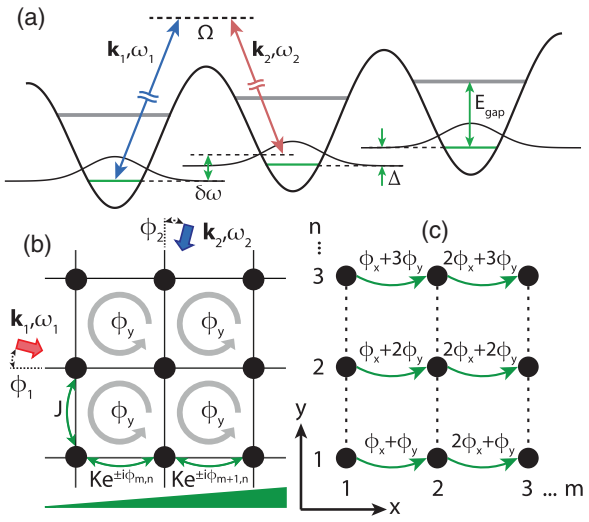

FIG. 1 (color online). (a) Raman-assisted tunneling in the lowest band of a tilted lattice with an energy offset Δ between neighboring sites and two-photon Rabi frequency Ω. (b) Experimental geometry to generate uniform magnetic fields using a pair of far-detuned laser beams and a uniform potential energy gradient. Tunneling along the x direction with amplitude K imprints a complex, spatially varying phase $\phi_{m,n}$—with site indices (m, n)—into the system due to the momentum transfer in the y direction. (c) A schematic depicting the position-dependent phases of the tunneling process. The equivalent number of flux quanta per unit cell is $\alpha = \phi_y/2\pi$.

Note that the two Raman beams couple different sites but do not change the internal state of the atoms. For resonant tunneling $\delta\omega = \Delta/\hbar$, time averaging over rapidly oscillating terms [20] yields an effective Hamiltonian which is time independent. As a result, the tilt has disappeared because, in the dressed atom picture, site (m, n) with j and k photons in the two Raman beams is degenerate with site $(m + 1, n)$ and $j + 1$ and $k - 1$ photons in the two beams. This effective Hamiltonian describes the system well, assuming that Δ is larger than the bandwidth $\sim J$ and smaller than the band gap E_{gap}. In addition, the effects of power broadening can be avoided if we choose Ω less than Δ. The resulting Hamiltonian is equivalent to one that describes charged particles on a lattice in a magnetic field under the tight-binding approximation [11,26]—the single-band Harper Hamiltonian

$$H = -\sum_{m,n}(Ke^{-i\phi_{m,n}}\hat{a}^\dagger_{m+1,n}\hat{a}_{m,n} + J\hat{a}^\dagger_{m,n+1}\hat{a}_{m,n} + \text{H.c.}) \quad (2)$$

with a spatially varying phase $\phi_{m,n} = \delta\mathbf{k}\cdot\mathbf{R}_{m,n} = m\phi_x + n\phi_y$ where $\mathbf{R}_{m,n}$ denotes the position of each lattice site. Solutions in this model are periodic with respect to the number of flux quanta per unit cell α. If the frequencies of the Raman beams are similar to those used for the optical lattice, one can tune α over the full range between zero and one by adjusting the angle between the Raman beams, and consequently k_y. A similar Hamiltonian can be realized for the tunneling of phonons between ion microtraps [31].

The spatially dependent phase imprinted by the Raman lasers, given by $\phi_{m,n}$, can be intuitively understood in a perturbative regime, where $J_{\text{pert}} = J_y$ and

$$K_{\text{pert}} = \frac{\Omega}{2}\int d^2\mathbf{r}w^*(\mathbf{r} - \mathbf{R}_{m,n})e^{-i\delta\mathbf{k}\cdot\mathbf{r}}w(\mathbf{r} - \mathbf{R}_{m,n} - a\hat{\mathbf{x}}) = Ke^{-i\delta\mathbf{k}\cdot\mathbf{R}_{m,n}}. \quad (3)$$

Adding up the accumulated phases around a closed path, one sees that this method leads to an enclosed phase of $\phi_y = \delta k_y a$ per lattice unit cell of area a^2, thus realizing the Harper Hamiltonian with $\alpha = \phi_y/2\pi$.

In a cubic lattice, the Wannier function $w(\mathbf{r})$ factorizes into $w(x)w(y)$ which are the localized Wannier-Stark and Wannier wave functions, respectively. The resulting expression for $K = (\Omega/2)\int dx w^*(x)e^{-ik_x x}w(x - a) \times \int dy w^*(y)e^{-ik_y y}w(y)$ shows that the momentum transfer in the x direction is necessary to have a nonvanishing tunneling matrix element K without changing the internal state. The x momentum transfer distinguishes our scheme from Refs. [20,22,27] and contributes to the vector potential $\mathbf{A} = [\hbar(k_y y + k_x x)/a]\hat{\mathbf{x}}$ but does not contribute to the enclosed flux or the value of the synthetic magnetic field $\mathbf{B}$. Note that this scheme does not realize the simple Landau gauge for the magnetic field.

For a more comprehensive description, we add the moving lattice—$V_{RM} = \Omega\sin(\delta\mathbf{k}\cdot\mathbf{r} - \omega t)$—of the two Raman lasers along with a linear tilt to the Hamiltonian in Eq. (1). In addition to the off-diagonal laser-assisted tunneling term, this moving lattice causes a diagonal term, which is a temporal modulation of the on-site energies. A unitary transformation, as in Refs. [29,32], leads to a frame rotating nonuniformly in time and position that eliminates the diagonal time dependence. For resonant drive $\Delta = \hbar\delta\omega$, the on-site energies are all equal and vanish while the remaining off-diagonal coupling has a time-independent part, leading to the Harper Hamiltonian, as in Eq. (2). The resulting expressions for K and J are (see the Supplemental Material [33])

$$K = \Omega\Phi_{y0}\left[\Phi_{x1}\frac{J_1(\Gamma_x)}{\Gamma_x} + i\Phi'_{x1}\frac{dJ_1(\Gamma_x)}{d\Gamma_x}\right], \qquad J = J_y J_0(\Gamma_y), \qquad \Gamma_i = \frac{2\Omega\Phi_{y0}\Phi_{x0}}{\Delta}\sin\left(\frac{k_i a}{2}\right), \quad (4)$$

where $\Phi_{i0} = \langle 0|\cos(k_i x_i)|0\rangle$ is the on-site matrix element, and $\Phi_{x1} = \langle 0|\sin[k_x(x - a/2)]|1\rangle$ and $\Phi'_{x1} = \langle 0|\cos[k_x(x - a/2)]|1\rangle$ are the off-diagonal matrix elements. This result is more general than the case of phase modulation [32] and the tight-binding limit in Refs. [30,34], where K is proportional to $J_1(x)$.

We implement the Harper Hamiltonian with each Raman laser aligned along one of the two lattice directions x and y corresponding to momentum transfer in both directions of $\hbar k_L$—the single-photon recoil of the lattice laser. The magnetic flux per unit cell resulting from $k_y = k_L$ is $\alpha = 1/2$. In the tight-binding limit for this momentum transfer, $\Phi_{i0} \approx 1$

and $\Phi_{x1} \approx -2J_x/\Delta \gg \Phi'_{x1}$, so the resonant tunneling amplitudes resulting from $k_x = k_L$ simplify to

$$K = J_x J_1\left(\frac{2\Omega}{\Delta}\right) \quad \text{and} \quad J = J_y J_0\left(\frac{2\Omega}{\Delta}\right). \tag{5}$$

Experimentally, the system is prepared by starting with a Bose-Einstein condensate of $\sim 5 \times 10^5$ ^{87}Rb atoms in the $|2, -2\rangle$ state in a crossed dipole trap. The Raman lasers are ramped up to their final intensities in 30 ms at a large detuning of 200 kHz and are switched to their final detuning after the tilt is applied to the system (see below). Unwanted interferences between lattice and Raman lasers are avoided with relative frequency offsets of >30 MHz using acousto-optic modulators. Next, we adiabatically load the condensate in 100 ms into a two-dimensional cubic optical lattice of spacing $\lambda_{\text{latt}}/2 = 532$ nm. For longer hold times, a weak $2E_r$ lattice beam along the third direction is simultaneously ramped up to provide additional confinement. Here, $E_r = \hbar^2 k_L^2/2m \approx h \times 2$ kHz is the single-photon recoil energy. The two-photon Rabi frequency of the moving Raman lattice is determined using free-space Rabi oscillations and chosen to be considerably smaller than the static lattice.

After loading the condensate into the lattice, a uniform potential energy gradient of $mga/h \approx 1.1$ kHz between adjacent lattice sites is applied by turning off the confining crossed dipole traps in 20 ms. Alternatively, we have successfully used a magnetic field gradient to access a broader range of tilts. The gravitational gradient has the advantage of a much faster switching time compared to the magnetic gradient. The cloud widths σ_x and σ_y are obtained by standard absorption imaging along the direction perpendicular to the 2D lattice.

The essential feature of our implementation of the Harper Hamiltonian is that tunneling in the x direction is suppressed by a potential tilt and reestablished by laser-assisted tunneling. This is demonstrated in Fig. 2, which shows the resonance for the laser-assisted process. For this,

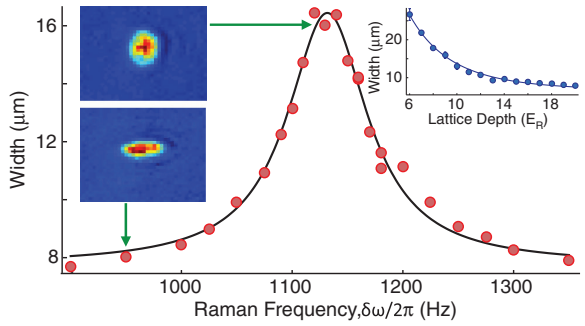

FIG. 2 (color online). *In situ* cloud width as a function of Raman detuning $\delta\omega$ after an expansion of 500 ms, with a Raman lattice depth of $\Omega = \Delta/4$. The solid line is a Lorentzian fit to the experimental data (dots) centered at 1133 Hz—consistent with the gravitational offset between sites. Pictures (of size 135×116 μm) show typical column densities on or off resonance. Inset: Dependence of the laser-assisted tunneling on optical lattice depth.

tunneling is characterized by looking at the expansion of the cloud within the lattice. Expansion occurs since the confinement by the optical dipole trap has been switched off, and due to some heating during the 500 ms hold time. Note that for fully coherent time evolution, charged particles in a magnetic field will undergo cyclotron motion which would suppress the expansion. The resonance width of 60 Hz may have contributions from laser frequency jitter, inhomogeneous lattice potential, and atomic interactions. The Lorentzian fit suggests a homogenous broadening mechanism.

The dependence of K and J on the intensity of the Raman lasers (described by Bessel functions) allows tuning of the ratio of the two. For low intensities, K increases linearly with the intensity, and J decreases quadratically. The latter reflects the depletion of the unperturbed Wannier function by the modulation due to the moving Raman lattice. Figure 3(a) shows experimental results in qualitative agreement with these predictions.

For a quantitative interpretation of the expansion of the cloud, we assume an incoherent diffusion process, where the square of the width σ of the expanded cloud is proportional to the tunneling rate times expansion time. For short times, the expansion of the cloud should be fully coherent, and the width should increase linearly with time. However, heating by light scattering and intensity fluctuations of the

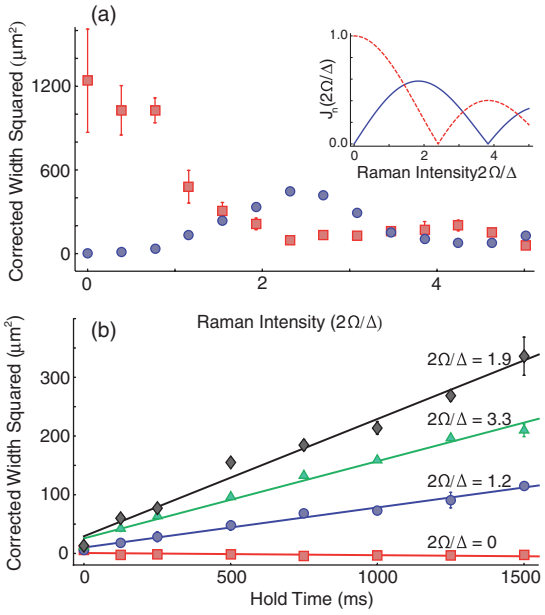

FIG. 3 (color online). (a) Expansion as a function of resonant Raman laser intensity shows the laser-assisted tunneling along the tilt direction (blue circles) and the tunneling rate J along the transverse direction (red squares). Data taken at lattice depths of $9E_r$ and hold time of 1500 ms. Inset: Theoretical prediction for the tunneling rates K and J in terms of Bessel functions [Eq. (5)]. (b) Time evolution of the squared width for different Raman laser intensities. From the slope of the lines, we obtain the laser-assisted tunneling rates and their statistical errors: 0.2 ± 0.08 (red squares), 4 ± 0.5 (blue circles), 12 ± 1 (black diamonds), and 8 ± 0.5 Hz (blue triangles).

laser beams lead to an incoherent, diffusive expansion. For finite time, we correct for the initial size σ_0 by assuming that the expansion and initial size add in quadrature, and plot the corrected squared width $\sigma_{\mathrm{corr}}^2 = \sigma^2 - \sigma_0^2$ versus time. The slope is proportional to the laser-assisted tunneling rate. Absolute tunneling rates are obtained by comparing this result to the expansion of the cloud in the y direction with the Raman beams far off resonance, when normal tunneling occurs. The ratio of the slopes is then K/J_y, with J_y calculated from the calibrated lattice depth to be $\sim h \times 48$ Hz. Figure 3(b) shows the time evolution of the square of the corrected size for various Raman intensities. The linear fits support the assumption of incoherent diffusion and allow a determination of tunneling rates, as summarized in the figure caption.

Laser-assisted tunneling is a powerful tool to manipulate the motion of atoms in optical lattices and to create novel Hamiltonians. We now describe different tunneling processes observed by a wide scan of the Raman detuning, shown in Fig. 4. A strong peak near 568 Hz fulfills the resonance condition $2\delta\omega = \Delta/\hbar$ for a four-photon nearest-neighbor tunneling process. This resonance is similar to the one observed in Ref. [35] by shaking the lattice. Note that the four-photon resonance is narrower (20 Hz versus 60 Hz) than the two-photon resonance, indicative of a higher-order process. Broad features at even lower frequency are most likely due to higher-order tunneling resonances and low-lying excitations within the first band.

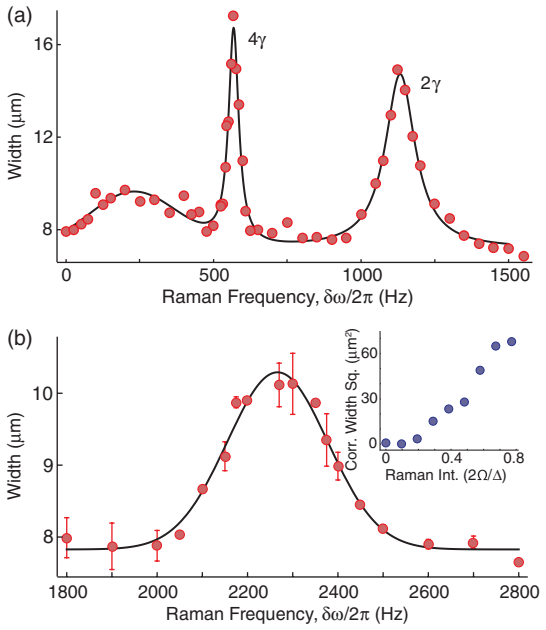

FIG. 4 (color online). Spectrum of excitations and tunneling resonances. (a) A strong, four-photon, nearest-neighbor tunneling resonance appears at $\Delta/2h$ along with the K resonance at Δ/h. These data were taken at a lattice depth of $9E_r$, for a two-photon Raman Rabi frequency of 1092 Hz and 500 ms expansion time. (b) Observation of next-nearest-neighbor laser-assisted tunneling at 2Δ and the expansion of the cloud as a function of Ω. Inset: No saturation is reached. Expansion time of 1500 ms.

Next-nearest-neighbor tunneling occurs at $\delta\omega = 2\Delta/\hbar$, twice the frequency of the fundamental resonance. For a shaken lattice (no Raman beams), this was studied in Ref. [36]. Analyzing the expansion of the cloud gives a tunneling rate of 0.4 ± 0.1 Hz, comparable to the next-nearest-neighbor tunneling rate in an untilted lattice, $\sim$0.8 Hz in our system. However, in an untilted lattice, next-nearest-neighbor tunneling is typically a hundred times slower than nearest-neighbor tunneling, whereas in laser-assisted tunneling, the two processes can be independently controlled by the laser power at the two resonant frequencies. Tunneling rates below 1 Hz are too slow for pursuing many-body physics, but the same scheme can be implemented for lighter atoms such as lithium in a shorter wavelength lattice, where the relevant scale factor, the recoil energy, is increased by a factor of 50.

After realizing and characterizing all parts of the Harper Hamiltonian, the next goal is to map out its band structure as a function of quasimomentum and magnetic field α—the Hofstadter butterfly. The ground state for a given α should be accessible by adiabatically transferring a condensate into this Hamiltonian. The ground state of the Harper Hamiltonian for $\alpha = 1/2$ has a clear signature in that its magnetic unit cell is twice as large as the lattice unit cell and its wave function has a unit cell that is 4 times as large, so time of flight imaging will reveal the resulting reduction of the Brillouin zone in momentum space by a factor of 4 [25,29,37–39]. So far, we have not been able to preserve the low entropy of the initial condensate and observe the ground state.

Preliminary experiments have shown less heating by the Raman beams at larger frequency detuning, requiring larger magnetic field gradients. An optimum detuning should be near half the band gap, avoiding inter- and intraband transitions. Possibly, an extension of the treatment of light scattering in optical lattices [40] could predict if there is a fundamental lower limit to the ratio of heating rate over K. Another potential source of heating is atomic interactions. Instabilities of certain quasimomentum states in optical lattices have been studied in Refs. [41,42]. Interaction-induced heating effects can in principle be avoided by using Feshbach resonances to tune the scattering length to zero or by using a single spin component of a fermionic gas. Once the ground state of the Harper Hamiltonian is established, different quasimomentum states can be populated through Bloch oscillations which occur at frequency $\delta = \delta\omega - \Delta/\hbar$, when the Raman lasers are slightly detuned from the resonance studied here.

The Harper Hamiltonian established in this work will be the starting point for many exciting explorations, including the quantum Hall effect, Dirac points, and novel topological phenomena [8,43]. Interactions between atoms may also lead to bosonic Laughlin states [44] and nonlinear Hofstadter eigenmodes [45]. The lowest band is topologically nontrivial with a Chern number of 1 [46] and should show chiral edge states. Most importantly, our scheme is simpler and potentially more robust than other suggestions,

since it does not require near-resonant light for connecting hyperfine states. It can be implemented for any atom—including the workhorse fermionic atoms lithium and potassium—which has small fine structure splittings, making it impossible to couple different spin states with negligible heating by spontaneous emission.

We acknowledge Yuri Lensky for experimental assistance. We thank Wujie Huang for helpful discussions and critical reading of the manuscript. This work was supported by the NSF through the Center of Ultracold Atoms, by NSF Grant No. PHY-0969731; under ARO Grant No. W911NF-13-1-0031 with funds from the DARPA OLE Program; and by ONR.

Note added.—Recently, we became aware of similar work carried out by Bloch and co-workers [34].

[1] K. von Klitzing, G. Dorda, and M. Pepper, Phys. Rev. Lett. **45**, 494 (1980).
[2] D. C. Tsui, H. L. Stormer, and A. C. Gossard, Phys. Rev. Lett. **48**, 1559 (1982).
[3] R. B. Laughlin, Phys. Rev. Lett. **50**, 1395 (1983).
[4] M. Lewenstein, A. Sanpera, and V. Ahufinger, *Ultracold Atoms in Optical Lattices* (Oxford University Press, Oxford, England, 2012).
[5] C. L. Kane and E. J. Mele, Phys. Rev. Lett. **95**, 226801 (2005).
[6] M. König, S. Wiedmann, C. Brüne, A. Roth, H. Buhmann, L. W. Molenkamp, X.-L. Qi, and S.-C. Zhang, Science **318**, 766 (2007).
[7] N. Regnault and B. A. Bernevig, Phys. Rev. X **1**, 021014 (2011).
[8] G. Möller and N. R. Cooper, Phys. Rev. Lett. **103**, 105303 (2009).
[9] L. Fu and C. L. Kane, Phys. Rev. Lett. **100**, 096407 (2008).
[10] V. Mourik, K. Zuo, S. M. Frolov, S. R. Plissard, E. P. A. M. Bakkers, and L. P. Kouwenhoven, Science **336**, 1003 (2012).
[11] D. R. Hofstadter, Phys. Rev. B **14**, 2239 (1976).
[12] B. Hunt, J. D. Sanchez-Yamagishi, A. F. Young, M. Yankowitz, B. J. LeRoy, K. Watanabe, T. Taniguchi, P. Moon, M. Koshino, P. Jarillo-Herrero, and R. C. Ashoori, Science **340**, 1427 (2013).
[13] L. Ponomarenko, R. V. Gorbachev, G. L. Yu, D. C. Elias, R. Jalil, A. A. Patel, A. Mishchenko, A. S. Mayorov, C. R. Woods, J. R. Wallbank, M. Mucha-Kruczynski, B. A. Piot, M. Potemski, I. Grigorieva, K. S. Novoselov, F. Guinea, V. I. Falko, and A. K. Geim, Nature (London) **497**, 594 (2013).
[14] C. R. Dean, L. Wang, P. Maher, C. Forsythe, F. Ghahari, Y. Gao, J. Katoch, M. Ishigami, P. Moon, M. Koshino, T. Taniguchi, K. Watanabe, K. L. Shepard, J. Hone, and P. Kim, Nature (London) **497**, 598 (2013).
[15] C. Albrecht, J. H. Smet, K. von Klitzing, D. Weiss, V. Umansky, and H. Schweizer, Phys. Rev. Lett. **86**, 147 (2001).
[16] K. W. Madison, F. Chevy, W. Wohlleben, and J. Dalibard, Phys. Rev. Lett. **84**, 806 (2000).
[17] J. R. Abo-Shaeer, C. Raman, J. M. Vogels, and W. Ketterle, Science **292**, 476 (2001).
[18] Y.-J. Lin, R. L. Compton, K. Jimenez-Garcia, J. V. Porto, and I. Spielman, Nature (London) **462**, 628 (2009).
[19] J. Dalibard, F. Gerbier, G. Juzeliūnas, and P. Öhberg, Rev. Mod. Phys. **83**, 1523 (2011).
[20] D. Jaksch and P. Zoller, New J. Phys. **5**, 56 (2003).
[21] E. J. Mueller, Phys. Rev. A **70**, 041603 (2004).
[22] F. Gerbier and J. Dalibard, New J. Phys. **12**, 033007 (2010).
[23] J. Struck, C. Ölschläger, M. Weinberg, P. Hauke, J. Simonet, A. Eckardt, M. Lewenstein, K. Sengstock, and P. Windpassinger, Phys. Rev. Lett. **108**, 225304 (2012).
[24] J. Struck, M. Weinberg, C. Ölschläger, P. Windpassinger, J. Simonet, K. Sengstock, R. Höppner, P. Hauke, A. Eckardt, M. Lewenstein, and L. Mathey, Nat. Phys., doi: 10.1038/nphys2750 (2013).
[25] M. Aidelsburger, M. Atala, S. Nascimbène, S. Trotzky, Y.-A. Chen, and I. Bloch, Phys. Rev. Lett. **107**, 255301 (2011).
[26] P. G. Harper, Proc. Phys. Soc. London Sect. A **68**, 874 (1955).
[27] A. R. Kolovsky, Europhys. Lett. **93**, 20 003 (2011).
[28] C. E. Creffield and F. Sols, Europhys. Lett. **101**, 40 001 (2013).
[29] H. Miyake, Ph.D. thesis, Massachusetts Institute of Technology, 2013.
[30] M. Aidelsburger, M. Atala, S. Nascimbène, S. Trotzky, Y.-A. Chen, and I. Bloch, Appl. Phys. B, doi: 10.1007/s00340-013-5418-1 (2013).
[31] A. Bermudez, T. Schaetz, and D. Porras, Phys. Rev. Lett. **107**, 150501 (2011).
[32] M. G. Tarallo, A. Alberti, N. Poli, M. L. Chiofalo, F.-Y. Wang, and G. M. Tino, Phys. Rev. A **86**, 033615 (2012).
[33] See Supplemental Material at http://link.aps.org/supplemental/10.1103/PhysRevLett.111.185302 for a detailed derivation of the Harper Hamiltonian from the Wannier-Stark Hamiltonian with laser-assisted hopping.
[34] M. Aidelsburger, M. Atala, M. Lohse, J. T. Barreiro, B. Paredes, and I. Bloch, preceding Letter, Phys. Rev. Lett. **111**, 185301 (2013).
[35] C. Sias, H. Lignier, Y. P. Singh, A. Zenesini, D. Ciampini, O. Morsch, and E. Arimondo, Phys. Rev. Lett. **100**, 040404 (2008).
[36] V. V. Ivanov, A. Alberti, M. Schioppo, G. Ferrari, M. Artoni, M. L. Chiofalo, and G. M. Tino, Phys. Rev. Lett. **100**, 043602 (2008).
[37] G. Möller and N. R. Cooper, Phys. Rev. A **82**, 063625 (2010).
[38] T. P. Polak and T. A. Zaleski, Phys. Rev. A **87**, 033614 (2013).
[39] S. Powell, R. Barnett, R. Sensarma, and S. Das Sarma, Phys. Rev. A **83**, 013612 (2011).
[40] H. Pichler, A. J. Daley, and P. Zoller, Phys. Rev. A **82**, 063605 (2010).
[41] L. Fallani, L. De Sarlo, J. E. Lye, M. Modugno, R. Saers, C. Fort, and M. Inguscio, Phys. Rev. Lett. **93**, 140406 (2004).
[42] G. K. Campbell, J. Mun, M. Boyd, E. W. Streed, W. Ketterle, and D. E. Pritchard, Phys. Rev. Lett. **96**, 020406 (2006).
[43] S. Powell, R. Barnett, R. Sensarma, and S. Das Sarma, Phys. Rev. A **83**, 013612 (2011).
[44] A. S. Sørensen, E. Demler, and M. D. Lukin, Phys. Rev. Lett. **94**, 086803 (2005).
[45] O. Manela, M. Segev, D. N. Christodoulides, and D. Kip, New J. Phys. **12**, 053017 (2010).
[46] M. Hafezi, A. S. Sørensen, E. Demler, and M. D. Lukin, Phys. Rev. A **76**, 023613 (2007).

Appendix C

Spin-Orbit Coupling and Quantum Spin Hall Effect for Neutral Atoms without Spin Flips

This appendix contains a reprint of [78], which was touched on, but not discussed in detail in the main text.

Spin-Orbit Coupling and Quantum Spin Hall Effect for Neutral Atoms without Spin Flips

Colin J. Kennedy, Georgios A. Siviloglou, Hirokazu Miyake, William Cody Burton, and Wolfgang Ketterle

MIT-Harvard Center for Ultracold Atoms, Research Laboratory of Electronics, Department of Physics, Massachusetts Institute of Technology, Cambridge, Massachusetts 02139, USA

(Received 28 August 2013; revised manuscript received 25 October 2013; published 25 November 2013)

We propose a scheme which realizes spin-orbit coupling and the quantum spin Hall effect for neutral atoms in optical lattices without relying on near resonant laser light to couple different spin states. The spin-orbit coupling is created by modifying the motion of atoms in a spin-dependent way by laser recoil. The spin selectivity is provided by Zeeman shifts created with a magnetic field gradient. Alternatively, a quantum spin Hall Hamiltonian can be created by all-optical means using a period-tripling, spin-dependent superlattice.

DOI: 10.1103/PhysRevLett.111.225301 PACS numbers: 67.85.−d, 03.65.Vf, 03.75.Lm

Many recent advances in condensed matter physics are related to the spin degree of freedom. The field of spintronics [1], the spin Hall effect [2], and topological insulators [3] all rely on the interplay between spin and motional degrees of freedom provided by spin-orbit coupling. Quantum simulations with neutral atoms have started to implement spin-orbit coupling using Raman transitions between different hyperfine states [4–8]. Since the Raman process transfers momentum to the atom, the resonance frequency is Doppler sensitive, and thus couples motion and spin.

The possibility of using spin-flip Raman processes to create interesting gauge fields was first pointed out in [9–11], and extended to non-Abelian gauge fields, which imply spin-orbit coupling, in [12,13]. With the exception of an atom chip proposal where the spin flips are induced with localized microwave fields [14], all recently proposed schemes are based on spin-flip Raman processes [8,15–20].

The major limitation of these Raman schemes is that spin-flip processes are inevitably connected with heating by spontaneous emission if they rely on spin-orbit coupling in the excited state, as in alkali atoms or other atoms with an S orbital ground state. Since laser beams interact with atoms via the electric dipole interaction, they do not flip the spin. Spin flips occur only due to intrinsic spin-orbit interactions within the atoms; therefore, spin-orbit coupling by spin-flip Raman processes relies on the spin-orbit coupling *within* the atom. Since the spontaneous emission rate and the two-photon Rabi frequency for Raman spin-flip processes scale in the same way with respect to the ratio of laser power to detuning, for a given atom the coupling strength relative to the spontaneous emission rate is fixed by the fine structure splitting compared to the natural linewidth. This has not been a limitation for the demonstration of single-particle or mean-field physics [4–8], but will become a severe restriction for many-body physics where interactions introduce a smaller energy scale and therefore require longer lifetimes of the atomic sample. Some authors have considered transitions involving metastable states of alkaline earth atoms to reduce the effects of spontaneous emission [21,22].

Here we present a spin-orbit coupling scheme that does not involve spin flips, is diagonal in the spin component σ_z, and corresponds to an Abelian gauge field. This scheme can be implemented with far-off-resonant laser beams, thus overcoming the limitation of short sample lifetimes due to spontaneous emission. In the field of cold atoms, many discussions of spin-orbit coupling emphasize its close relationship to non-Abelian gauge fields [17,23] which are non-diagonal for any spin component and therefore mix spin and motion in a more complicated way. However, a scheme diagonal in the spin component is sufficient for quantum spin Hall physics and topological insulators [24,25], and its implementation has major experimental advantages. In the theoretical proposals and demonstration of the spin Hall [23,26] and quantum spin hall [27] effects for quantum gases, Raman spin flips are used to create an Abelian gauge field diagonal with respect to one spin component.

The physical principle of the spin-orbit coupling scheme presented here is very different from spin-flip schemes. It does not require any kind of spin-orbit coupling within the atom. Rather, spin-dependent vector potentials are engineered utilizing the Zeeman effect in a magnetic field—atoms in the spin-up and -down states interact with different pairs of laser beams, or differently with the same pair, and the photon recoil changes the atom's motion in a spin-dependent way. This results in spin-orbit coupling which is diagonal in the spin basis.

To begin, we summarize the relationship between spin-orbit coupling and spin-dependent vector potentials. For charged particles, the origin of spin-orbit coupling is the relativistic transformation of electromagnetic fields. When an electron moves through an electric field $\mathbf{E}$ it experiences a magnetic field $\mathbf{B}$ in its moving frame which interacts with the spin $\boldsymbol{\sigma}$ (described by the Pauli spin matrices). Spin-orbit coupling contributes a term proportional to $(\mathbf{p} \times \mathbf{E}) \cdot \boldsymbol{\sigma}$ in the Hamiltonian. As such, an electric field in the z direction gives rise to the Rashba spin-orbit coupling $(\boldsymbol{\sigma} \times \mathbf{p})_z = \sigma_x p_y - \sigma_y p_x$.

Assuming a 2D system confined to the x, y plane, and an in-plane electric field, the spin-orbit interaction conserves

σ_z. Following [25], a radial electric field $\mathbf{E} \sim E(x, y, 0)$ leads to a spin-orbit coupling term in the Hamiltonian of the form $E\sigma_z(xp_y - yp_x)$, or equivalently to $E\boldsymbol{\sigma} \cdot \mathbf{L}$, where $\mathbf{L}$ is the angular momentum of the atom. Such a radial field could be created by a uniformly charged cylinder, or can be induced by applying stress to a semiconductor sample [25]. This spin-coupling term is identical to the $\mathbf{A} \cdot \mathbf{p}$ term for the Hamiltonian describing a spin in a magnetic field, $\sigma_z B$. Using the symmetric gauge for the vector potential $\mathbf{A} = (\sigma_z B/2)(y, -x, 0)$, one obtains a term in the Hamiltonian proportional to $\sigma_z B(xp_y - yp_x)$. Therefore, this form of spin-orbit coupling is equivalent to a spin-dependent magnetic field which exerts opposite Lorentz forces on spin-up and -down atoms. This leads to the spin Hall effect which creates a transverse spin current and no charge or mass currents [24,25]. The $\mathbf{A}^2$ term constitutes a parabolic spin-independent potential which is irrelevant for the spin physics discussed here.

We now present a scheme which realizes such an Abelian gauge field [28] and manifests itself as a spin-dependent magnetic field. Recently, the MIT group [30,31] and the Munich group [32,33] have suggested and implemented a scheme to generate synthetic magnetic fields for neutral atoms in an optical lattice. The scheme is based on the simple Hamiltonian for noninteracting particles in a 2D cubic lattice,

$$H = -\sum_{m,n} (J_x \hat{a}^\dagger_{m+1,n} \hat{a}_{m,n} + J_y \hat{a}^\dagger_{m,n+1} \hat{a}_{m,n} + \text{H.c.}), \quad (1)$$

where $J_{x(y)}$ describes tunneling in the x (y) direction and $\hat{a}^\dagger_{m,n}$ ($\hat{a}_{m,n}$) is the creation (annihilation) operator of a particle at lattice site (m, n). The setup is detailed in [30] and summarized as follows: a linear tilt of energy Δ per lattice site is applied using a magnetic field gradient in the x direction, thus suppressing normal tunneling in this direction. Resonant tunneling is restored with two far-detuned Raman beams of two-photon Rabi frequency Ω, frequency detuning $\delta\omega = \omega_1 - \omega_2$, and momentum transfer $\mathbf{k} = \mathbf{k_1} - \mathbf{k_2}$. Considering only the case of resonant tunneling, $\delta\omega = \Delta/\hbar$, rapidly oscillating terms time average out [34], yielding an effective Hamiltonian which is time independent [30]:

$$H = -\sum_{m,n} (K e^{-i\phi_{m,n}} \hat{a}^\dagger_{m+1,n} \hat{a}_{m,n} + J \hat{a}^\dagger_{m,n+1} \hat{a}_{m,n} + \text{H.c.}). \quad (2)$$

This effective Hamiltonian describes charged particles on a lattice in a magnetic field under the tight-binding approximation [35,36]. The gauge field arises from the spatially varying phase $\phi_{m,n} = \mathbf{k} \cdot \mathbf{R}_{m,n} = mk_x a + nk_y a$, where a is the lattice constant, and has the form $\mathbf{A} = [\hbar(k_x x + k_y y)/a]\hat{\mathbf{x}}$. One can tune the flux per unit cell α for a given spin state over the full range between 0 and 1 by adjusting the angle between the Raman beams, and consequently k_y.

We now extend this scheme to the spin degree of freedom, and assume a mixture of atoms in two hyperfine states, labeled spin up and down. If the potential energy gradient is the same for the two states, then the two states experience the same magnetic field. This is the situation when the tilt is provided by gravity, a scalar ac Stark shift gradient, or a magnetic field gradient if both states have the same magnetic moment—the phase $\phi_{m,n}$ is independent of σ_z.

If the two states have the same value of the magnetic moment, but opposite sign, then the potential gradient is opposite for the two states. This can be realized by using states of the same hyperfine level F, but with opposite magnetic quantum number M_F (e.g., in ^{23}Na or ^{87}Rb, the $|F, M_F\rangle = |2, 2\rangle$ and $|2, -2\rangle$ states), or by picking another suitable pair of hyperfine states. In this case, for laser-assisted tunneling between two sites m and $m + 1$, the roles of the two laser beams—absorption of a photon versus stimulated emission of a photon—for the Raman process are reversed, as depicted in Fig. 1. Therefore, the two states receive opposite momentum transfer, and this sign change leads to a sign change for the phase,

$$\phi_{m,n} = (mk_x a + nk_y a)\sigma_z, \quad (3)$$

and also for the vector potential and the magnetic field. The vector potential realized by this scheme,

$$\mathbf{A} = \left[\frac{\hbar}{a}(k_x x + k_y y)\hat{\mathbf{x}}\right]\sigma_z, \quad (4)$$

creates the spin-orbit coupling discussed in the introduction, although in a different gauge. The x dependence in the x component of $\mathbf{A}$ is necessary for a non-negligible tunneling matrix element for the laser-assisted process [30].

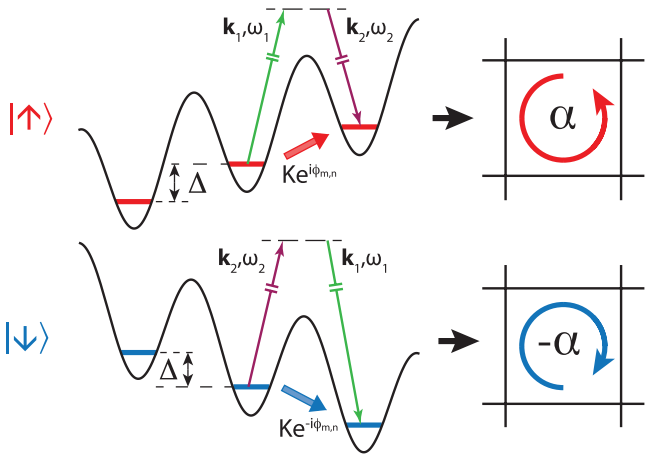

FIG. 1 (color online). Spin-dependent tunneling in an optical lattice tilted by a magnetic field gradient. When the two spin states have opposite magnetic moments, the role of absorbtion and emission of the two photons is exchanged. The result is that the two states have tunneling matrix elements with opposite phases, leading to opposite synthetic magnetic fields and realizing spin-orbit coupling and the quantum spin Hall effect.

This system now has time-reversal symmetry, in contrast to the system with the same synthetic magnetic field for both states (since a magnetic field breaks time-reversal symmetry). This scheme implements spin-orbit coupling both in two and three dimensions and with bosons and fermions. For fermions, in two dimensions it realizes the quantized spin Hall effect consisting of two opposite quantum Hall phases. It is protected by a $\mathbb{Z}$ topological index due to the fact that σ_z is conserved [24,25].

When the values of the two magnetic moments are different, and the potential energy gradient is provided by a magnetic field gradient, then the two states have different Bloch oscillation frequencies, Δ/h. Each state now needs two separate Raman beams for laser-assisted tunneling (or they can share one beam). This implies that the synthetic magnetic field can now be chosen to be the same, to be opposite, or to be different for the two spin states. One option is to have zero synthetic magnetic field for one of the states. Atoms in this state can still tunnel along the tilt direction by using a Raman process without y-momentum transfer, or, equivalently, by inducing tunneling through lattice modulation [37–39]. In the case of two different magnetic moments, one could also perform dynamic experiments, where laser parameters are modified in such a way that one switches either suddenly or adiabatically from the quantum Hall effect to the spin quantum Hall effect.

An intriguing possibility is to couple the two states. Since σ_z is no longer conserved, the system should become a topological insulator with the $\mathbb{Z}_2$ classification [3,40], provided that the coupling is done in a time-reversal invariant way. This can be done with a term which is not diagonal in σ_z—i.e., a $\sigma_x p_y$ term—by adding spin-flip Raman lasers to induce spin-orbit coupling, or by driving the spin-flip transition with rf or microwave fields. A coherent rf drive field would not be time-reversal invariant, but it would be interesting to study the effect of symmetry breaking in such a state [41]. A drive field where the phase is randomized should lead to a time-reversal invariant Hamiltonian.

Our scheme implements the idealized scheme for a quantum spin Hall system consisting of two opposite quantum Hall phases. This is a starting point for breaking symmetries and exploring additional terms in the Hamiltonian. References [41,42] discuss a weak quantum spin Hall phase, induced by breaking the time-reversal symmetry by a magnetic field—this can be achieved by population imbalance between the two spin states. A spin-imbalanced quantum Hall phase can turn into a spin-filtered quantum Hall phase [41,42] where only one component has chiral edge states. This can be achieved by realizing a finite synthetic magnetic field for one component and zero for the other. Changing the spin-orbit coupling can induce topological quantum phase transitions between a helical quantum spin Hall phase and a chiral spin-imbalanced quantum Hall state. This can probably be achieved in a population-imbalanced system by adding additional Raman spin-flip beams [41,42].

Thus far, we have discussed single-particle physics. Adding interactions, by increasing the density with deeper lattices or through Feshbach resonances, will induce interesting correlations and may lead to fractional topological insulators [43]. Another option is spin-drag experiments [44,45], transport experiments where one spin component transfers momentum to the other component. For the situation mentioned above, where the synthetic magnetic field is zero for one component (e.g., spin up), a transport experiment revealing the Hall effect [46] for spin down would show a nonvanishing Hall conductivity for spin up due to spin drag. In addition, one would expect that spin-exchange interactions destroy the two opposite quantum Hall phases, and should lead to the quantum spin Hall phase with $\mathbb{Z}_2$ topological index.

We now present another way of realizing the physics discussed above, using optical superlattices instead of a potential energy gradient. This has the advantage of purely optical control and avoids possible heating due to Landau-Zener tunneling [47] between Wannier Stark states. Thus far, optical superlattices have allowed the observation of the ground state with staggered magnetic flux [48], in contrast to experiments with magnetic tilts [30,33].

Figure 2 summarizes the new scheme. The superlattice has 3 times the period of the basic lattice, thus distinguishing sites A, B, C in energy. Resonant tunneling is reestablished using three pairs of Raman beams with frequencies $\omega_1 + \Delta_{AB}/\hbar$, $\omega_2 + \Delta_{BC}/\hbar$, and $\omega_3 - (\Delta_{AB} + \Delta_{BC})/\hbar$ collinear in one arm and ω_1, ω_2, and ω_3 collinear in another arm at an angle to the first. Consequently, there is always the same momentum transfer for tunneling in the y direction, leading to the same flux as the scheme with the magnetic tilt, and Eqs. (3) and (4) apply. This is in contrast

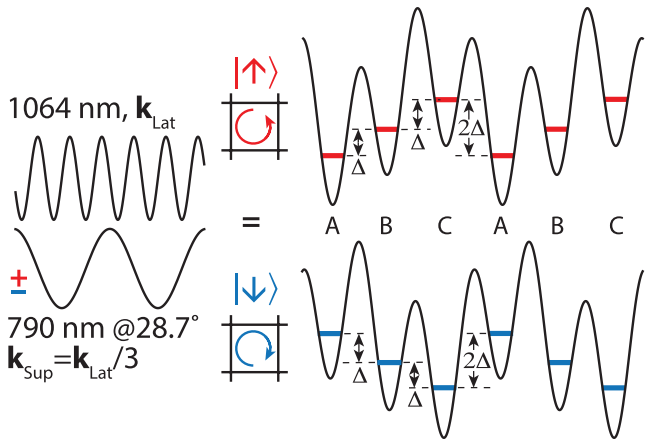

FIG. 2 (color online). Superlattice scheme for realizing the quantum Hall and quantum spin Hall effect. A superlattice with 3 times the spatial period as the fundamental lattice leads to three distinguishable sites A, B, C. For the quantum spin Hall effect, the superlattice operates at a magic wavelength where the ac Stark effect is opposite for the two spin states. For rubidium, this is achieved at a wavelength of 790 nm. When filled with fermions the quantum Hall and spin quantum Hall effects are realized.

to schemes with two distinguishable sites A and B (by using internal states [21,34] or a superlattice [48]), which lead to a staggered magnetic field. Rectification of the magnetic flux in a staggered configuration by adding a tilt [34,48] or a superlattice [21] has also been proposed. In the latter scheme, this would result in four distinguishable sites (two internal states A, B, doubled up by the superlattice). Another rectification scheme uses three internal states [49]. Our scheme avoids spin-flip transitions between internal states, and has the minimum number of ingredients of three different sites to provide directionality. Furthermore, by adjusting the spatial phase shift between the fundamental and the superlattice, one can choose the energy offsets $\Delta_{AB} = \Delta_{BC} = -\Delta_{CA}/2$ (see Fig. 2). The scheme can then be implemented by shining Raman beams from two directions, each beam having two frequencies.

This scheme would realize Hofstadter's butterfly and the quantum Hall effect. For the quantum spin Hall effect, one has to choose the superlattice laser to be at the magic wavelength where the scalar ac Stark shift vanishes, and only a vector ac Stark shift remains, corresponding to a so-called fictitious magnetic field [50,51]. By detuning the laser between the D_1 and D_2 lines, one can achieve a pure vector ac Stark shift, which is equal in magnitude but opposite in sign when the atoms in the two hypefine states have opposite magnetic moments. In this case, the superlattice will provide opposite potentials for the two states, resulting in opposite momentum transfers due to the Raman beams and opposite vector potentials. The superlattice period is $\lambda/[2\sin(\theta/2)]$, where θ is the angle between the two superlattice beams, which is adjusted to make the superlattice period 3 times the period of the basic lattice. This scheme realizes the quantum spin Hall effect and a topological insulator with two opposite quantum Hall phases with a purely optical scheme and no Raman spin-flip transitions.

To replace the magnetic field gradient by a superlattice that generates a fictitious magnetic field, the laser detuning has to be on the order of the fine structure splitting, resulting in heating due to spontaneous emission. For atoms like rubidium, the lifetime is many seconds [50]. To be specific, we consider a low-density gas ^{87}Rb atom in the $F = 2$, $M_F = \pm 2$ states in a lattice with a depth of 10 photon recoils at the wavelength of 1064 nm. A superlattice with a lattice depth of 10 kHz is created by interfering two laser beams at 790.0 nm of 1.0 mW of laser power and a beam waist of 125 μm. The resulting offset Δ_{AB} and Δ_{AC} will be approximately 4 and 8 kHz, respectively, well placed in the band gap of the basic lattice. The spontaneous scattering rate induced by the superlattice beams is less than 0.1 per second. Alternatively, the superlattice producing the fictitious magnetic field can be replaced by a sinusoidal (real) magnetic field generated by an atom chip [52].

There have been several suggestions of how to detect properties of the quantum Hall and quantum spin Hall phases. Time-of-flight pictures will reveal the enlarged magnetic unit cell due to the synthetic magnetic field [48,53–55]. Hall plateaus can be discerned in the density distribution [56]. The Chern number of a filled band can be measured interferometrically [57] or using ballistic expansion [58]. Topological edge states can be directly imaged [59,60] or detected by Bragg spectroscopy [61–63].

Topological insulators can be realized by engineering appropriate lattice Hamiltonians with ultracold atoms [64]. This may allow studying classes of topological insulators [65,66] which have not been realized in nature. Topological insulators with strong interactions [64] can be explored in cold atom systems using Feshbach resonances.

Our work maps out a route towards spin-orbit coupling, the spin Hall effect, and topological insulators which does not require coupling of different internal states with spin-flipping Raman lasers. The Hamiltonian describing the system is diagonal in the σ_z spin component. This follows closely the two original Letters on the spin Hall effect [24,25]. In addition, we have presented two configurations for realizing a quantum spin Hall Hamiltonian. The scheme with the magnetic tilt completely avoids near resonant light, and the superlattice scheme provides a purely optical approach.

This work was supported by the NSF through the Center of Ultracold Atoms, by NSF Award No. PHY-0969731, under ARO Grant No. W911NF-13-1-0031 with funds from the DARPA OLE program, and by ONR. This work was completed at the Aspen Center for Physics (supported in part by the National Science Foundation under Grant No. PHYS-1066293), and insightful discussions with Hui Zhai, Jason Ho, and Nigel Cooper are acknowledged. We thank Wujie Huang for a critical reading of the manuscript.

Note added.—After most of this work was completed [67], we became aware of similar work carried out by Bloch and colleagues in Munich [33,68].

[1] Insight on Spintronics, Nature Materials, Vol. 11, May 2012.
[2] Y. K. Kato, R. C. Myers, A. C. Gossard, and D. D. Awschalom, Science **306**, 1910 (2004).
[3] M. Z. Hasan and C. L. Kane, Rev. Mod. Phys. **82**, 3045 (2010).
[4] Y. J. Lin, K. Jiménez-García, and I. B. Spielman, Nature (London) **471**, 83 (2011).
[5] J.-Y. Zhang, S.-C. Ji, Z. Chen, L. Zhang, Z.-D. Du, B. Yan, G.-S. Pan, B. Zhao, Y.-J. Deng, H. Zhai, S. Chen, and J.-W. Pan, Phys. Rev. Lett. **109**, 115301 (2012).
[6] P. Wang, Z.-Q. Yu, Z. Fu, J. Miao, L. Huang, S. Chai, H. Zhai, and J. Zhang, Phys. Rev. Lett. **109**, 095301 (2012).
[7] L. W. Cheuk, A. T. Sommer, Z. Hadzibabic, T. Yefsah, W. S. Bakr, and M. W. Zwierlein, Phys. Rev. Lett. **109**, 095302 (2012).
[8] V. Galitski and I. B. Spielman, Nature (London) **494**, 49 (2013).
[9] J. Higbie and D. M. Stamper-Kurn, Phys. Rev. Lett. **88**, 090401 (2002).

[10] G. Juzeliūnas and P. Öhberg, Phys. Rev. Lett. **93**, 033602 (2004).
[11] G. Juzeliūnas, J. Ruseckas, P. Öhberg, and M. Fleischhauer, Phys. Rev. A **73**, 025602 (2006).
[12] J. Ruseckas, G. Juzeliūnas, P. Öhberg, and M. Fleischhauer, Phys. Rev. Lett. **95**, 010404 (2005).
[13] K. Osterloh, M. Baig, L. Santos, P. Zoller, and M. Lewenstein, Phys. Rev. Lett. **95**, 010404 (2005).
[14] B. M. Anderson, I. B. Spielman, and G. Juzeliūnas, Phys. Rev. Lett. **111**, 125301 (2013).
[15] G. Juzeliūnas, J. Ruseckas, and J. Dalibard, Phys. Rev. A **81**, 053403 (2010).
[16] J. Dalibard, F. Gerbier, G. Juzeliūnas, and P. Öhberg, Rev. Mod. Phys. **83**, 1523 (2011).
[17] T.-L. Ho and S. Zhang, Phys. Rev. Lett. **107**, 150403 (2011).
[18] B. M. Anderson, G. Juzeliūnas, V. M. Galitski, and I. B. Spielman, Phys. Rev. Lett. **108**, 235301 (2012).
[19] Z. F. Xu and L. You, Phys. Rev. A **85**, 043605 (2012).
[20] W. S. Cole, S. Zhang, A. Paramekanti, and N. Trivedi, Phys. Rev. Lett. **109**, 085302 (2012).
[21] F. Gerbier and J. Dalibard, New J. Phys. **12**, 033007 (2010).
[22] B. Béri and N. R. Cooper, Phys. Rev. Lett. **107**, 145301 (2011).
[23] M. C. Beeler, R. A. Williams, K. Jiménez-García, L. J. LeBlanc, A. R. Perry, and I. B. Spielman, Nature (London) **498**, 201 (2013).
[24] C. L. Kane and E. J. Mele, Phys. Rev. Lett. **95**, 226801 (2005).
[25] B. A. Bernevig and S.-C. Zhang, Phys. Rev. Lett. **96**, 106802 (2006).
[26] X.-J. Liu, X. Liu, L. C. Kwek, and C. H. Oh, Phys. Rev. Lett. **98**, 026602 (2007).
[27] S.-L. Zhu, H. Fu, C. J. Wu, S. C. Zhang, and L. M. Duan, Phys. Rev. Lett. **97**, 240401 (2006).
[28] The vector potential which we realize is Abelian. In the lattice all link variables and loop matrices commute, but for reasons which are not clear to us the gauge field is defined to be non-Abelian using the Wilson loop criteria [29].
[29] N. Goldman, G. Juzeliunas, P. Ohberg, I. B. Spielman, arXiv:1308.6533.
[30] H. Miyake, G. A. Siviloglou, C. J. Kennedy, W. C. Burton, and W. Ketterle, Phys. Rev. Lett. **111**, 185302 (2013).
[31] H. Miyake, Ph.D. thesis, Massachusetts Institute of Technology, 2013.
[32] M. Aidelsburger, M. Atala, S. Nascimbéne, S. Trotzky, Y. A. Chen, and I. Bloch, Appl. Phys. B **113**, 1 (2013).
[33] M. Aidelsburger, M. Atala, M. Lohse, J. T. Barreiro, B. Paredes, and I. Bloch, Phys. Rev. Lett. **111**, 185301 (2013).
[34] D. Jaksch and P. Zoller, New J. Phys. **5**, 56 (2003).
[35] P. G. Harper, Proc. Phys. Soc. London Sect. A **68**, 874 (1955).
[36] D. R. Hofstadter, Phys. Rev. B **14**, 2239 (1976).
[37] V. V. Ivanov, A. Alberti, M. Schioppo, G. Ferrari, M. Artoni, M. L. Chiofalo, and G. M. Tino, Phys. Rev. Lett. **100**, 043602 (2008).
[38] C. Sias, H. Lignier, Y. P. Singh, A. Zenesini, D. Ciampini, O. Morsch, and E. Arimondo, Phys. Rev. Lett. **100**, 040404 (2008).
[39] M. Glsuck, A. R. Kolovsky, and H. J. Korsch, Phys. Rep. **366**, 103 (2002).
[40] C. L. Kane and E. J. Mele, Phys. Rev. Lett. **95**, 146802 (2005).
[41] N. Goldman, W. Beugeling, and C. Morais Smith, Europhys. Lett. **97**, 23 003 (2012).
[42] W. Beugeling, N. Goldman, and C. Morais Smith, Phys. Rev. B **86**, 075118 (2012).
[43] M. Levin and A. Stern, Phys. Rev. Lett. **103**, 196803 (2009).
[44] R. A. Duine and H. T. C. Stoof, Phys. Rev. Lett. **103**, 170401 (2009).
[45] S. B. Koller, A. Groot, P. C. Bons, R. A. Duine, H. T. C. Stoof, and P. van der Straten, arXiv:1204.6143.
[46] L. J. LeBlanc, K. Jiménez-García, R. A. Williams, M. C. Beeler, A. R. Perry, W. D. Phillips, and I. B. Spielman, Proc. Natl. Acad. Sci. U.S.A. **109**, 10 811 (2012).
[47] Q. Niu, X. G. Zhao, G. A. Georgakis, and M. G. Raizen, Phys. Rev. Lett. **76**, 4504 (1996).
[48] M. Aidelsburger, M. Atala, S. Nascimbéne, S. Trotzky, Y. A. Chen, and I. Bloch, Phys. Rev. Lett. **107**, 255301 (2011).
[49] E. J. Mueller, Phys. Rev. A **70**, 041603 (2004).
[50] D. McKay and B. DeMarco, New J. Phys. **12**, 055013 (2010).
[51] C. Cohen-Tannoudji and J. Dupont-Roc, Phys. Rev. A **5**, 968 (1972).
[52] N. Goldman, I. Satija, P. Nikolic, A. Bermudez, M. A. Martin-Delgado, M. Lewenstein, and I. B. Spielman, Phys. Rev. Lett. **105**, 255302 (2010).
[53] G. Möller and N. R. Cooper, Phys. Rev. A **82**, 063625 (2010).
[54] S. Powell, R. Barnett, R. Sensarma, and S. Das Sarma, Phys. Rev. A **83**, 013612 (2011).
[55] T. P. Polak and T. A. Zaleski, Phys. Rev. A **87**, 033614 (2013).
[56] R. O. Umucalılar, H. Zhai, and M. Ö. Oktel, Phys. Rev. Lett. **100**, 070402 (2008).
[57] D. A. Abanin, T. Kitagawa, I. Bloch, and E. Demler, Phys. Rev. Lett. **110**, 165304 (2013).
[58] E. Zhao, N. Bray-Ali, C. J. Williams, I. B. Spielman, and I. I. Satija, Phys. Rev. A **84**, 063629 (2011).
[59] T. D. Stanescu, V. Galitski, J. Y. Vaishnav, C. W. Clark, and S. Das Sarma, Phys. Rev. A **79**, 053639 (2009).
[60] N. Goldman, J. Dalibard, A. Dauphin, F. Gerbier, M. Lewenstein, P. Zoller, and I. B. Spielman, Proc. Natl. Acad. Sci. U.S.A. **110**, 6736 (2013).
[61] X.-J. Liu, X. Liu, C. Wu, and J. Sinova, Phys. Rev. A **81**, 033622 (2010).
[62] N. Goldman, J. Beugnon, and F. Gerbier, Phys. Rev. Lett. **108**, 255303 (2012).
[63] M. Buchhold, D. Cocks, and W. Hofstetter, Phys. Rev. A **85**, 063614 (2012).
[64] T. D. Stanescu, V. Galitski, and S. Das Sarma, Phys. Rev. A **82**, 013608 (2010).
[65] A. Kitaev, Ann. Phys. (Amsterdam) **321**, 2 (2006).
[66] S. Ryu, A. P. Schnyder, A. Furusaki, and A. W. W. Ludwig, New J. Phys. **12**, 065010 (2010).
[67] W. Ketterle, in Proceedings of the International Conference on Quantum Technologies, Moscow, 2013.
[68] I. Bloch, in Proceedings of the International Conference on Quantum Technologies, Moscow, 2013.

Bibliography

[1] K. B. Davis, M. O. Mewes, M. R. Andrews, N. J. van Druten, D. S. Durfee, D. M. Kurn, and W. Ketterle. Bose-einstein condensation in a gas of sodium atoms. *Phys. Rev. Lett.*, 75:3969–3973, Nov 1995.

[2] M. H. Anderson, J. R. Ensher, M. R. Matthews, C. E. Wieman, and E. A. Cornell. Observation of bose-einstein condensation in a dilute atomic vapor. *Science*, 269(5221):198–201, 1995.

[3] M. R. Andrews, C. G. Townsend, H.-J. Miesner, D. S. Durfee, D. M. Kurn, and W. Ketterle. Observation of interference between two bose condensates. *Science*, 275(5300):637–641, 1997.

[4] C. Raman, M. Köhl, R. Onofrio, D. S. Durfee, C. E. Kuklewicz, Z. Hadzibabic, and W. Ketterle. Evidence for a critical velocity in a bose-einstein condensed gas. *Phys. Rev. Lett.*, 83:2502–2505, Sep 1999.

[5] J. R. Abo-Shaeer, C. Raman, J. M. Vogels, and W. Ketterle. Observation of vortex lattices in bose-einstein condensates. *Science*, 292(5516):476–479, 2001.

[6] D. Schneble, Y. Torii, M. Boyd, E. W. Streed, D. E. Pritchard, and W. Ketterle. The onset of matter-wave amplification in a superradiant bose-einstein condensate. *Science*, 300(5618):475–478, 2003.

[7] B. DeMarco and D. S. Jin. Onset of fermi degeneracy in a trapped atomic gas. *Science*, 285(5434):1703–1706, 1999.

[8] S. Chu, J. E. Bjorkholm, A. Ashkin, and A. Cable. Experimental observation of optically trapped atoms. *Phys. Rev. Lett.*, 57:314–317, Jul 1986.

[9] D. M. Stamper-Kurn, M. R. Andrews, A. P. Chikkatur, S. Inouye, H.-J. Miesner, J. Stenger, and W. Ketterle. Optical confinement of a bose-einstein condensate. *Phys. Rev. Lett.*, 80:2027–2030, Mar 1998.

[10] J. Hubbard. Electron correlations in narrow energy bands. *Proceedings of the Royal Society of London A: Mathematical, Physical and Engineering Sciences*, 276(1365):238–257, 1963.

[11] P. A. Lee, N. Nagaosa, and X.-G. Wen. Doping a mott insulator: Physics of high-temperature superconductivity. *Rev. Mod. Phys.*, 78:17–85, Jan 2006.

[12] D. Jaksch, C. Bruder, J. I. Cirac, C. W. Gardiner, and P. Zoller. Cold bosonic atoms in optical lattices. *Phys. Rev. Lett.*, 81:3108–3111, Oct 1998.

[13] D. van Oosten, P. van der Straten, and H. T. C. Stoof. Quantum phases in an optical lattice. *Phys. Rev. A*, 63:053601, Apr 2001.

[14] M. Greiner, O. Mandel, T. Esslinger, T. W. Hänsch, and I. Bloch. Quantum phase transition from a superfluid to a mott insulator in a gas of ultracold atoms. *Nature*, 415:39, Jan 2002.

[15] A. Görlitz, J. M. Vogels, A. E. Leanhardt, C. Raman, T. L. Gustavson, J. R. Abo-Shaeer, A. P. Chikkatur, S. Gupta, S. Inouye, T. Rosenband, and W. Ketterle. Realization of bose-einstein condensates in lower dimensions. *Phys. Rev. Lett.*, 87:130402, Sep 2001.

[16] D. Greif, G. Jotzu, M. Messer, R. Desbuquois, and T. Esslinger. Formation and dynamics of antiferromagnetic correlations in tunable optical lattices. *Phys. Rev. Lett.*, 115:260401, Dec 2015.

[17] C. K. Thomas, T. H. Barter, T.-H. Leung, S. Daiss, and D. M. Stamper-Kurn. Signatures of spatial inversion asymmetry of an optical lattice observed in matter-wave diffraction. *Phys. Rev. A*, 93:063613, Jun 2016.

[18] D. Jaksch and P. Zoller. Creation of effective magnetic fields in optical lattices: the hofstadter butterfly for cold neutral atoms. *New J. Phys.*, 5(1):56, 2003.

[19] A. R. Kolovsky. Creating artificial magnetic fields for cold atoms by photon-assisted tunneling. *Europhys. Lett.*, 93(2):20003, 2011.

[20] Y.-J. Lin, R. L. Compton, K. Jimenez-Garcia, J. V. Porto, and I. B. Spielman. Synthetic magnetic fields for ultracold neutral atoms. *Nature*, 462(7273):628–632, 2009.

[21] M. Aidelsburger, M. Atala, M. Lohse, J. T. Barreiro, B. Paredes, and I. Bloch. Realization of the hofstadter hamiltonian with ultracold atoms in optical lattices. *Phys. Rev. Lett.*, 111(18):185301, 2013.

[22] H. Miyake, G. A. Siviloglou, C. J. Kennedy, W. C. Burton, and W. Ketterle. Realizing the harper hamiltonian with laser-assisted tunneling in optical lattices. *Phys. Rev. Lett.*, 111(18):185302, 2013.

[23] J. Struck, M. Weinberg, C. Olschlager, P. Windpassinger, J. Simonet, K. Sengstock, R. Hoppner, P. Hauke, A. Eckardt, M. Lewenstein, and L. Mathey. Engineering ising-xy spin-models in a triangular lattice using tunable artificial gauge fields. *Nat. Phys.*, 9:738–743, Nov. 2013.

[24] G. Jotzu, M. Messer, R. Desbuquois, M. Lebrat, T. Uehlinger, D. Greif, and T. Esslinger. Experimental realization of the topological Haldane model with ultracold fermions. *Nature*, 515(7526):237–240, November 2014.

[25] A. D. Cronin, J. Schmiedmayer, and D. E. Pritchard. Optics and interferometry with atoms and molecules. *Rev. Mod. Phys.*, 81:1051–1129, Jul 2009.

[26] S. Dimopoulos, P. W. Graham, J. M. Hogan, and M. A. Kasevich. Testing general relativity with atom interferometry. *Phys. Rev. Lett.*, 98:111102, Mar 2007.

[27] A. O. Jamison, J. N. Kutz, and S. Gupta. Atomic interactions in precision interferometry using bose-einstein condensates. *Phys. Rev. A*, 84:043643, Oct 2011.

[28] A. O. Jamison, B. Plotkin-Swing, and S. Gupta. Advances in precision contrast interferometry with yb bose-einstein condensates. *Phys. Rev. A*, 90:063606, Dec 2014.

[29] I. Carusotto, L. Pitaevskii, S. Stringari, G. Modugno, and M. Inguscio. Sensitive measurement of forces at the micron scale using bloch oscillations of ultracold atoms. *Phys. Rev. Lett.*, 95:093202, Aug 2005.

[30] G. Ferrari, N. Poli, F. Sorrentino, and G. M. Tino. Long-lived bloch oscillations with bosonic sr atoms and application to gravity measurement at the micrometer scale. *Phys. Rev. Lett.*, 97:060402, Aug 2006.

[31] S. Schreppler, N. Spethmann, N. Brahms, T. Botter, M. Barrios, and D. M. Stamper-Kurn. Optically measuring force near the standard quantum limit. *Science*, 344(6191):1486–1489, 2014.

[32] E. W. Streed, J. Mun, M. Boyd, G. K. Campbell, P. Medley, W. Ketterle, and D. E. Pritchard. Continuous and pulsed quantum zeno effect. *Phys. Rev. Lett.*, 97:260402, Dec 2006.

[33] P. Medley, D. M. Weld, H. Miyake, D. E. Pritchard, and W. Ketterle. Spin gradient demagnetization cooling of ultracold atoms. *Phys. Rev. Lett.*, 106:195301, May 2011.

[34] N. Ashcroft and N. D. Mermin. *Solid State Physics*. Brooks/Cole, Cengage Learning, 1976.

[35] E. A. Martinez, C. A. Muschik, P. Schindler, D. Nigg, A. Erhard, M. Heyl, P. Hauke, M. Dalmonte, T. Monz, P. Zoller, and R. Blatt. Real-time dynamics of lattice gauge theories with a few-qubit quantum computer. *Nature*, 534:516, June 2016.

[36] D. Yang, G. S. Giri, M. Johanning, C. Wunderlich, P. Zoller, and P. Hauke. Analog quantum simulation of (1+1)-dimensional lattice qed with trapped ions. *Phys. Rev. A*, 94:052321, Nov 2016.

[37] N. Goldman, J. C. Budich, and P. Zoller. Topological quantum matter with ultracold gases in optical lattices. *Nature Physics*, 12:639, June 2016.

[38] N. Goldman, G. Juzeliūnas, P. Öhberg, and I. B. Spielman. Light-induced gauge fields for ultracold atoms. *Rep. Prog. Phys.*, 77(12):126401, December 2014.

[39] J. Schachenmayer, D. M. Weld, H. Miyake, G. A. Siviloglou, W. Ketterle, and A. J. Daley. Adiabatic cooling of bosons in lattices to magnetically ordered quantum states. *Phys. Rev. A*, 92:041602, Oct 2015.

[40] E. Altman, W. Hofstetter, E. Demler, and M. D. Lukin. Phase diagram of two-component bosons on an optical lattice. *New Journal of Physics*, 5(1):113, 2003.

[41] D. Barredo, S. de Léséleuc, V. Lienhard, T. Lahaye, and A. Browaeys. An atom-by-atom assembler of defect-free arbitrary two-dimensional atomic arrays. *Science*, 354(6315):1021–1023, 2016.

[42] M. Endres, H. Bernien, A. Keesling, H. Levine, E. R. Anschuetz, A. Krajenbrink, C. Senko, V. Vuletic, M. Greiner, and M. D. Lukin. Atom-by-atom assembly of defect-free one-dimensional cold atom arrays. *Science*, 354(6315):1024–1027, 2016.

[43] W. Kohn. Analytic properties of bloch waves and wannier functions. *Phys. Rev.*, 115:809–821, Aug 1959.

[44] Y. Lensky and C. Kennedy. Scheme for generalized maximmally localized wannier functions in one dimension. *Preprint at https://arxiv.org/abs/1412.3734*, 2014.

[45] G. K. Campbell, J. Mun, M. Boyd, P. Medley, A. E. Leanhardt, L. G. Marcassa, D. E. Pritchard, and W. Ketterle. Imaging the mott insulator shells by using atomic clock shifts. *Science*, 313(5787):649–652, 2006.

[46] H. Fukuyama, R. A. Bari, and H. C. Fogedby. Tightly bound electrons in a uniform electric field. *Phys. Rev. B*, 8:5579–5586, Dec 1973.

[47] X. Chen, Z.-C. Gu, Z.-X. Liu, and X.-G. Wen. Symmetry-Protected Topological Orders in Interacting Bosonic Systems. *Science*, 338(6114):1604–1606, December 2012.

[48] C. Wang, A. C. Potter, and T. Senthil. Classification of interacting electronic topological insulators in three dimensions. *Science*, 343(6171):629–631, 2014.

[49] R. Willett, J. P. Eisenstein, H. L. Störmer, D. C. Tsui, A. C. Gossard, and J. H. English. Observation of an even-denominator quantum number in the fractional quantum Hall effect. *Phys. Rev. Lett.*, 59(15):1776–1779, October 1987.

[50] L. Fu and C. L. Kane. Superconducting Proximity Effect and Majorana Fermions at the Surface of a Topological Insulator. *Phys. Rev. Lett.*, 100(9):096407, March 2008.

[51] M. T. Deng, C. L. Yu, G. Y. Huang, M. Larsson, P. Caroff, and H. Q. Xu. Anomalous Zero-Bias Conductance Peak in a Nb-InSb Nanowire-Nb Hybrid Device. *Nano Lett.*, 12(12):6414–6419, December 2012.

[52] S. Nadj-Perge, I. K. Drozdov, J. Li, H. Chen, S. Jeon, J. Seo, A. H. MacDonald, B. A. Bernevig, and A. Yazdani. Observation of Majorana fermions in ferromagnetic atomic chains on a superconductor. *Science*, 346(6209):602–607, October 2014.

[53] K. W. Madison, F. Chevy, W. Wohlleben, and J. Dalibard. Vortex formation in a stirred bose-einstein condensate. *Phys. Rev. Lett.*, 84:806–809, Jan 2000.

[54] N. Gemelke, E. Sarajlic, and S. Chu. Rotating few-body atomic systems in the fractional quantum hall regime. *Preprint at http://arXiv.org/abs/1007.2677*, 2010.

[55] P. G. Harper. Single band motion of conduction electrons in a uniform magnetic field. *Proc. Phys. Soc. A*, 68(10):874, 1955.

[56] M. Y. Azbel. Energy spectrum of a conduction electron in a magnetic field. *Sov. Phys. Jetp-Ussr*, 19(3):634–645, 1964.

[57] D. R. Hofstadter. Energy levels and wave functions of bloch electrons in rational and irrational magnetic fields. *Phys. Rev. B*, 14:2239–2249, Sep 1976.

[58] M. Aidelsburger, M. Lohse, C. Schweizer, M. Atala, J. T. Barreiro, S. Nascimbéne, N. R. Cooper, I. Bloch, and N. Goldman. Measuring the Chern number of Hofstadter bands with ultracold bosonic atoms. *Nat. Phys.*, 11(2):162–166, February 2015.

[59] M. Aidelsburger, M. Atala, S. Nascimbène, S. Trotzky, Y.-A. Chen, and I. Bloch. Experimental realization of strong effective magnetic fields in an optical lattice. *Phys. Rev. Lett.*, 107(25):255301, 2011.

[60] M. Atala, M. Aidelsburger, M. Lohse, J. T. Barreiro, B. Paredes, and I. Bloch. Observation of chiral currents with ultracold atoms in bosonic ladders. *Nat. Phys.*, 10(8):588–593, 2014.

[61] B. K. Stuhl, H.-I. Lu, L. M. Aycock, D. Genkina, and I. B. Spielman. Visualizing edge states with an atomic Bose gas in the quantum Hall regime. *Preprint at http://arXiv.org/abs/1502.02496*, February 2015.

[62] L.-K. Lim, A. Hemmerich, and C. M. Smith. Artificial staggered magnetic field for ultracold atoms in optical lattices. *Phys. Rev. A*, 81(2):023404, 2010.

[63] G. Möller and N. R. Cooper. Condensed ground states of frustrated bose-hubbard models. *Phys. Rev. A*, 82(6):063625, 2010.

[64] S. Powell, R. Barnett, R. Sensarma, and S. Das Sarma. Bogoliubov theory of interacting bosons on a lattice in a synthetic magnetic field. *Phys. Rev. A*, 83:013612, Jan 2011.

[65] C. J. Kennedy, W. C. Burton, W. C. Chung, and W. Ketterle. Observation of Bose-Einstein condensation in a strong synthetic magnetic field. *Nat. Phys.*, 11(10):859–864, oct 2015.

[66] E. Haller, R. Hart, M. J. Mark, J. G. Danzl, L. Reichsöllner, and H.-C. Nägerl. Inducing transport in a dissipation-free lattice with super bloch oscillations. *Phys. Rev. Lett.*, 104:200403, May 2010.

[67] A. Alberti, G. Ferrari, V. V. Ivanov, M. L. Chiofalo, and G. M. Tino. Atomic wave packets in amplitude-modulated vertical optical lattices. *New J. Phys.*, 12(6):065037, 2010.

[68] M. Kohmoto. Topological invariant and the quantization of the hall conductance. *Ann. Phys.*, 160(2):343–354, 1985.

[69] T. P. Polak and T. A. Zaleski. Time-of-flight patterns of ultracold bosons in optical lattices in various abelian artificial magnetic field gauges. *Phys. Rev. A*, 87:033614, Mar 2013.

[70] T. Ozawa, H. M. Price, and I. Carusotto. The Momentum-Space Harper-Hofstadter Model. *Preprint at http://arXiv.org/abs/1411.1203*, November 2014.

[71] M. Polini, R. Fazio, A. H. MacDonald, and M. P. Tosi. Realization of fully frustrated josephson-junction arrays with cold atoms. *Phys. Rev. Lett.*, 95:010401, Jun 2005.

[72] C. V. Parker, L.-C. Ha, and C. Chin. Direct observation of effective ferromagnetic domains of cold atoms in a shaken optical lattice. *Nat. Phys.*, 9(12):769–774, 2013.

[73] R. O. Umucalılar and M. Ö Oktel. Phase boundary of the boson Mott insulator in a rotating optical lattice. *Phys. Rev. A*, 76(5):055601, November 2007.

[74] T. Bilitewski and N. R. Cooper. Scattering theory for floquet-bloch states. *Phys. Rev. A*, 91:033601, Mar 2015.

[75] S. Choudhury and E. J. Mueller. Transverse collisional instabilities of a bose-einstein condensate in a driven one-dimensional lattice. *Phys. Rev. A*, 91:023624, Feb 2015.

[76] T. Bilitewski and N. R. Cooper. Population dynamics in a floquet realization of the harper-hofstadter hamiltonian. *Phys. Rev. A*, 91:063611, Jun 2015.

[77] T. Dubček, C. J. Kennedy, L. Lu, W. Ketterle, M. Soljačić, and H. Buljan. Weyl points in three-dimensional optical lattices: Synthetic magnetic monopoles in momentum space. *Phys. Rev. Lett.*, 114:225301, Jun 2015.

[78] C. J. Kennedy, G. A. Siviloglou, H. Miyake, W. C. Burton, and W. Ketterle. Spin-orbit coupling and quantum spin hall effect for neutral atoms without spin flips. *Phys. Rev. Lett.*, 111:225301, Nov 2013.

[79] M. Lewenstein, A. Sanpera, and V. Ahufinger. *Ultracold Atoms in Optical Lattices: Simulating quantum many-body systems*. OUP Oxford, 2012.

[80] N. R. Cooper and J. Dalibard. Reaching Fractional Quantum Hall States with Optical Flux Lattices. *Phys. Rev. Lett.*, 110(18):185301, April 2013.

[81] S. A. Weidinger and M. Knap. Floquet prethermalization and regimes of heating in a periodically driven, interacting quantum system. *Sci. Rep*, 7:45382, April 2017.

[82] M. Reitter, J. Näger, K. Wintersperger, C. Sträter, I. Bloch, A. Eckardt, and U. Schneider. Interaction dependent heating and atom loss in a periodically driven optical lattice. *Phys. Rev. Lett.*, 119:200402, Nov 2017.

[83] H. Miyake, G. A. Siviloglou, C. J. Kennedy, W. C. Burton, and W. Ketterle. Realizing the harper hamiltonian with laser-assisted tunneling in optical lattices. *Phys. Rev. Lett.*, 111:185302, Oct 2013.

[84] M. Aidelsburger, M. Atala, M. Lohse, J. T. Barreiro, B. Paredes, and I. Bloch. Realization of the hofstadter hamiltonian with ultracold atoms in optical lattices. *Phys. Rev. Lett.*, 111:185301, Oct 2013.

[85] M. Gustavsson, E. Haller, M. J. Mark, J. G. Danzl, G. Rojas-Kopeinig, and H.-C. Nägerl. Control of interaction-induced dephasing of bloch oscillations. *Phys. Rev. Lett.*, 100:080404, Feb 2008.

[86] I. D. Leroux, M. H. Schleier-Smith, and V. Vuletić. Implementation of cavity squeezing of a collective atomic spin. *Phys. Rev. Lett.*, 104:073602, Feb 2010.

[87] G.-B. Jo, Y. Shin, S. Will, T. A. Pasquini, M. Saba, W. Ketterle, D. E. Pritchard, M. Vengalattore, and M. Prentiss. Long phase coherence time and number squeezing of two bose-einstein condensates on an atom chip. *Phys. Rev. Lett.*, 98:030407, Jan 2007.

[88] J. G. Bohnet, K. C. Cox, M. A. Norcia, J. M. Weiner, Z. Chen, and J. K. Thompson. Reduced spin measurement back-action for a phase sensitivity ten times beyond the standard quantum limit. *Nature Photonics*, 8(9):731–736, September 2014.

[89] G.-B. Jo, J.-H. Choi, C. A. Christensen, T. A. Pasquini, Y.-R. Lee, W. Ketterle, and D. E. Pritchard. Phase-sensitive recombination of two bose-einstein condensates on an atom chip. *Phys. Rev. Lett.*, 98:180401, Apr 2007.

[90] J. Estève, C. Gross, A. Weller, S. Giovanazzi, and M. K. Oberthaler. Squeezing and entanglement in a Bose–Einstein condensate. *Nature*, 455(7217):1216–1219, October 2008.

[91] W. C. Burton, C. J. Kennedy, W. C. Chung, S. Vadia, W. Chen, and W. Ketterle. Coherence times of bose-einstein condensates beyond the shot-noise limit via superfluid shielding. *Phys. Rev. Lett.*, 117:275301, Dec 2016.

[92] D. Witthaut, M. Werder, S. Mossmann, and H. J. Korsch. Bloch oscillations of Bose-Einstein condensates: Breakdown and revival. *Phys. Rev. E*, 71:036625, Mar 2005.

[93] F. Meinert, M. J. Mark, E. Kirilov, K. Lauber, P. Weinmann, M. Gröbner, and H.-C. Nägerl. Interaction-induced quantum phase revivals and evidence for the transition to the quantum chaotic regime in 1d atomic bloch oscillations. *Phys. Rev. Lett.*, 112:193003, May 2014.

[94] A. R. Kolovsky. Bose–hubbard hamiltonian: Quantum chaos approach. *Int. J. Mod. Phys. B*, 30(10):1630009, 2016.

[95] S. Walter, D. Schneble, and A. C. Durst. Bloch oscillations in lattice potentials with controlled aperiodicity. *Phys. Rev. A*, 81:033623, Mar 2010.

[96] T. Schulte, S. Drenkelforth, G. Kleine Büning, W. Ertmer, J. Arlt, M. Lewenstein, and L. Santos. Dynamics of bloch oscillations in disordered lattice potentials. *Phys. Rev. A*, 77:023610, Feb 2008.

[97] M. Gustavsson, E. Haller, M. J. Mark, J. G. Danzl, R. Hart, A. J. Daley, and H. NÃd'gerl. Interference of interacting matter waves. *New J. Phys.*, 12(6):065029, 2010.

[98] J. Javanainen and M. Y. Ivanov. Splitting a trap containing a bose-einstein condensate: Atom number fluctuations. *Phys. Rev. A*, 60:2351–2359, Sep 1999.

[99] T. Akatsuka, M. Takamoto, and H. Katori. Optical lattice clocks with non-interacting bosons and fermions. *Nat. Phys.*, 4(12):954–959, December 2008.

[100] T. Akatsuka, M. Takamoto, and H. Katori. Three-dimensional optical lattice clock with bosonic ^{88}Sr atoms. *Phys. Rev. A*, 81:023402, Feb 2010.

[101] M. D. Swallows, M. Bishof, Y. Lin, S. Blatt, M. J. Martin, A. M. Rey, and J. Ye. Suppression of collisional shifts in a strongly interacting lattice clock. *Science*, 331(6020):1043–1046, 2011.

[102] D. C. McKay and B. DeMarco. Cooling in strongly correlated optical lattices: prospects and challenges. *Reports on Progress in Pnysics*, 74:054401, Apr 2011.

[103] I. Bloch, J. Dalibard, and S. Nascimbène. Quantum simulations with ultracold quantum gases. *Nature Physics*, 8:267, Apr 2012.

[104] L. W. Cheuk, M. A. Nichols, K. R. Lawrence, M. Okan, H. Zhang, E. Khatami, N. Trivedi, T. Paiva, M. Rigol, and M. W. Zwierlein. Observation of spatial charge and spin correlations in the 2d fermi-hubbard model. *Science*, 353(6305):1260–1264, 2016.

[105] M. Boll, T. A. Hilker, G. Salomon, A. Omran, J. Nespolo, L. Pollet, I. Bloch, and C. Gross. Spin- and density-resolved microscopy of antiferromagnetic correlations in fermi-hubbard chains. *Science*, 353(6305):1257–1260, 2016.

[106] A. Mazurenko, C. S. Chiu, G. Ji, M. F. Parsons, M. Kanász-Nagy, R. Schmidt, F. Grusdt, E. Demler, D. Greif, and M. Greiner. A cold-atom fermi–hubbard antiferromagnet. *Nature*, 545:462, May 2017.

[107] M. Erhard, H. Schmaljohann, J. Kronjäger, K. Bongs, and K. Sengstock. Measurement of a mixed-spin-channel feshbach resonance in ^{87}Rb. *Phys. Rev. A*, 69:032705, Mar 2004.

[108] A. M. Kaufman, R. P. Anderson, Thomas M. Hanna, E. Tiesinga, P. S. Julienne, and D. S. Hall. Radio-frequency dressing of multiple feshbach resonances. *Phys. Rev. A*, 80:050701, Nov 2009.

[109] O. Mandel, M. Greiner, A. Widera, T. Rom, T. W. Hänsch, and I. Bloch. Coherent transport of neutral atoms in spin-dependent optical lattice potentials. *Phys. Rev. Lett.*, 91:010407, Jul 2003.

[110] F. D. M. Haldane. Nonlinear field theory of large-spin heisenberg antiferromagnets: Semiclassically quantized solitons of the one-dimensional easy-axis néel state. *Phys. Rev. Lett.*, 50:1153–1156, Apr 1983.